

# PHOTOACOUSTIC DETECTION OF METASTATIC MELANOMA IN THE HUMAN CIRCULATORY SYSTEM

---

A Thesis presented to the Faculty of the Graduate School  
University of Missouri-Columbia

---

In Partial Fulfillment  
Of the Requirements for the Degree

Master of Science

---

by

RYAN MICHAEL WEIGHT

Dr. John A. Viator, Thesis Supervisor

DECEMBER 2006

© Copyright by Ryan Michael Weight 2006  
All Rights Reserved



The undersigned, appointed by the Dean of the Graduate School, have examined the thesis entitled:

**PHOTOACOUSTIC DETECTION OF METASTATIC  
MELANOMA IN THE HUMAN CIRCULATORY  
SYSTEM**

Presented by Ryan Michael Weight

A candidate for the degree of Master of Science

And hereby certify that in their opinion it is worthy of acceptance.

---

Dr. John A. Viator  
Biological Engineering

---

Dr. Paul S. Dale  
Ellis Fischel Cancer Center

---

Dr. Gang Yao  
Biological Engineering

---

Dr. Mark Haidekker  
Biological Engineering

This Work Is Dedicated To My Grandmother

Alice Chop

February 2, 1928- March 28, 2006

## ACKNOWLEDGEMENTS

As a fellow student and good friend of mine once said, "This work is built upon the shoulders of the giants that came before us". I believe this phrase to refer to the persons whose hard work and dedication have made it possible for me to progress to where I am today. Foremost, I must mention my academic advisor Dr. John A. Viator, whose guidance and patient support have allowed me to attain my most lofty goals and aspirations. Dr. Viator and his family embraced both myself and my fellow graduate students whole heartedly and provided tremendous support and encouragement to us all. Dr. Viator first introduced me to the field of photoacoustics and offered me a position as his first graduate student. He tolerated the fact that I was only a short term Masters student and entrusted me with the undertaking of a very large and undefined project that could not have been any more suitable to my interests. Dr. Viator provided me with the direction necessary to accelerate the project as well as the appropriate tools and monies to make it a success. Without his multi-faceted knowledge and creativeness, this project would have never been possible, and I certainly would never have had the enjoyment of taking a part in it. For that I thank him indefinitely.

Secondly, I must thank my clinical advisor and co-creator of the melanoma project, Dr. Paul S. Dale. Dr. Dale, a surgical oncologist at Ellis Fischel Cancer Center, has been a significant role model for myself in addition to just being an all around great guy. It was his work with cancer patients and melanomas that led to the inception of the melanoma project. He saw a need in the medical field, and in conjunction with Dr. Viator and his work in photoacoustics, conceptualized a method to fulfill this need which eventually led to the development of the melanoma project. Dr. Dale has provided me with immense support for both the completion of

this work and my future interests. He, as well as Dr. Viator, have served as mentors to me, guiding me through difficult decisions regarding both the project and life. I would like to formally thank Dr. Dale for his invaluable guidance and assistance as well as express the utmost gratitude to both Dr. Dale and Dr. Viator for giving me the opportunity to succeed.

I would like to thank my fellow graduate students and friends, Rob Talbert and Melvin Sims, for their support and entertainment. I would like to thank Dr. Fan and his students for positively critiquing my work and sharing our comfortable lab space and supplies. I would also like to thank Dr. Gerardo Gutiérrez Juárez from the University of Guanajuato, Mexico, for his impressive work with integrating sphere calibration. I wish them all the best.

I must give acknowledgment and thanks to the numerous academic contributors from the University of Missouri. I would like to give many thanks to Dr. Charles Caldwell, Dr. Allison Lisle, and Mufad Al-Kuhlani in the Pathology Department of the UMC Medical School for their tireless work in obtaining, culturing, counting, and sustaining our ever-so-delicate and equally important melanoma cells. I must thank Dr. David Lee and his students in the Microbiology and Immunology Department of the UMC Medical School for guidance in the operations of blood centrifugation and PBMC isolation. Without these contributors this work would not be where it is today.

This work was funded by the University of Missouri Department of Surgery Seed Grant as well as funds from the Bioprocessing and Biosensing Center administered by the Biological Engineering Department of the University of Missouri-Columbia.

I wish to thank the Biological Engineering Department of the University of Missouri-Columbia, specifically Dr. Gang Yao and Dr. Mark Haidekker for serving on my thesis committee. In addition I would like to acknowledge Dr. Yao for conveying to me the knowledge of light/tissue interactions over the course of two semesters. Much appreciation is also due to Dr. Sheila Grant, my undergraduate advisor, and Dr. Jinglu Tan for persuading me to pursue a Masters degree at UMC.

Finally, I thank my family. My mother, Joyce Weight, my father, John Weight,

and my brother, Evan Weight, for their continued support and love through all of my endeavors. My family is the most powerful source of support to whom I owe my character and ambition along with all of my accomplishments. I would like to extend my greatest appreciation to all my extended family especially my grandmother, Alice Chop, to whom this work is dedicated. She fought cancer with all of her might and remains the strongest most influential person to ever grace my life.

# TABLE OF CONTENTS

<b>ACKNOWLEDGEMENTS.....</b>	<b>ii</b>
<b>LIST OF FIGURES.....</b>	<b>xii</b>
<b>LIST OF TABLES.....</b>	<b>xviii</b>
<b>ABSTRACT.....</b>	<b>xix</b>
<b>Chapter</b>	
<b>1 INTRODUCTION TO PHOTOACOUSTICS</b>	<b>1</b>
1.1 History . . . . .	1
1.2 Theory . . . . .	2
1.3 Applications . . . . .	5
<b>2 INTRODUCTION TO CANCER</b>	<b>6</b>
2.1 History . . . . .	6
2.2 Challenges . . . . .	7
2.3 Melanoma . . . . .	9
2.3.1 Overview . . . . .	9
2.3.2 Types of Melanoma . . . . .	10
2.3.3 Disease Progression . . . . .	10
2.4 Staging . . . . .	11
2.5 Metastasis . . . . .	11
2.5.1 Transformation . . . . .	12
2.5.2 Intravasation and Extravasation . . . . .	12

2.5.3	Secondary Tumor Formation . . . . .	13
2.5.4	Parallel Evolution Theory . . . . .	14
2.6	Treatment . . . . .	15
2.7	Detection . . . . .	16
2.7.1	Clinical Methodology And Shortcomings . . . . .	16
2.7.2	Current Areas of Development . . . . .	17
2.7.3	Immunomagnetic Separation and Laser Scanning Cytometry .	17
2.7.4	Cell Filtration and Laser Scanning Cytometry . . . . .	18
2.7.5	Reverse Transcriptase-Polymerase Chain Reaction . . . . .	18
2.8	Implementing the Photoacoustic Device . . . . .	19
<b>3</b>	<b>PHOTOACOUSTIC DETECTION SYSTEM</b>	<b>21</b>
3.1	Introduction . . . . .	21
3.2	Development and Design . . . . .	22
3.3	Detection Apparatus . . . . .	22
3.3.1	Flow Cell . . . . .	22
3.3.2	PVDF Copolymer Film . . . . .	23
3.3.3	Electrodes . . . . .	23
3.3.4	Flow System . . . . .	24
3.4	Laser . . . . .	27
3.4.1	Optical Parametric Oscillator . . . . .	28
3.4.2	Fiber Coupling . . . . .	28
3.4.3	Beam Focusing and Profiling . . . . .	28
3.5	Photoacoustic Mechanism . . . . .	29
3.5.1	Excitation . . . . .	29
3.5.2	Acoustic Wave Propagation . . . . .	29
3.5.3	Acoustic Wave Detection . . . . .	30
3.5.4	Signal Transduction . . . . .	30
3.6	Data Acquisition . . . . .	30
3.6.1	Amplification and Signal Display . . . . .	30

3.7	System Modifications and Improvements . . . . .	32
3.7.1	Design . . . . .	32
3.7.2	Detection . . . . .	32
3.7.3	Signal Improvement . . . . .	35
3.8	Final Setup Design . . . . .	37

## 4 DETECTION TRIALS INCORPORATING LATEX MICROSPHERES 39

4.1	Introduction . . . . .	39
4.2	Latex Microspheres . . . . .	39
4.2.1	Specifications . . . . .	39
4.2.2	Spectroscopy . . . . .	40
4.3	Materials and Methods . . . . .	41
4.3.1	Saline Solutions . . . . .	41
4.4	Initial Results . . . . .	42
4.4.1	Photoacoustic Waveform . . . . .	42
4.4.2	Dual Chamber Flow Cell . . . . .	42
4.4.3	Single Chamber Flow Cell . . . . .	43
4.4.4	Thresholding . . . . .	47
4.5	Discussion of Initial Results . . . . .	49
4.5.1	Pilot Study . . . . .	49
4.5.2	Time Domain Response . . . . .	50
4.5.3	Single Chamber Sensitivity . . . . .	50
4.6	Redesign and Confirmation of Results . . . . .	53
4.6.1	Saline Solutions . . . . .	54
4.6.2	Photoacoustic Waveforms . . . . .	55
4.6.3	Thresholding . . . . .	58
4.7	Discussion of Custom Design . . . . .	59
4.7.1	Saline Concentration . . . . .	59
4.7.2	Time Domain Response . . . . .	60
4.7.3	Peak Signal Intensity . . . . .	60



4.7.4	Threshold . . . . .	61
4.7.5	Effects of Modification . . . . .	62
4.8	Conclusions . . . . .	63
<b>5</b>	<b>DETECTION OF TISSUE PHANTOMS ISOLATED IN THE PERIPHERAL BLOOD MONONUCLEAR CELL LAYER</b>	<b>64</b>
5.1	Introduction . . . . .	64
5.2	White Blood Cells and the Peripheral Blood Mononuclear Cells . . .	65
5.3	Materials and Methods . . . . .	66
5.3.1	Blood Draw . . . . .	66
5.3.2	Isolation of Mononuclear Cell Layer . . . . .	67
5.3.3	Introduction of Microspheres . . . . .	68
5.4	Results . . . . .	69
5.4.1	Mononuclear Cell Layer Control . . . . .	69
5.4.2	Post-Mononuclear-Cell-Isolation Addition of Microspheres . . . . .	69
5.4.3	Pre-Mononuclear-Cell-Isolation Addition of Microspheres . . . . .	70
5.4.4	Plasma . . . . .	70
5.5	Discussion . . . . .	71
5.5.1	Controls . . . . .	71
5.5.2	Peak Values . . . . .	73
5.5.3	Plasma . . . . .	74
5.6	Conclusion . . . . .	74
<b>6</b>	<b>DETECTION TRIALS INCORPORATING LIVE MELANOMA CELLS</b>	<b>75</b>
6.1	Introduction . . . . .	75
6.2	Melanoma . . . . .	76
6.2.1	Cell Line . . . . .	78
6.2.2	Medium . . . . .	78

6.3	Cell Counting . . . . .	79
6.4	Microscopy and Fontana-Masson Staining . . . . .	80
6.5	Materials and Methods . . . . .	81
6.5.1	White Microsphere Control . . . . .	81
6.5.2	Medium Control . . . . .	83
6.5.3	Cell Preparation . . . . .	84
6.6	Results . . . . .	84
6.6.1	Controls . . . . .	84
6.6.2	Photoacoustic Waveforms . . . . .	84
6.7	Discussion . . . . .	85
6.7.1	Cell Line . . . . .	85
6.7.2	Peak Values . . . . .	88
6.7.3	Determination of Melanoma Detection . . . . .	89
6.7.4	Sources of Error . . . . .	90
6.8	Conclusion . . . . .	90

## **7 INTEGRATING SPHERE THEORY AND OPTICAL PROPERTY**

	<b>DETERMINATION</b>	<b>91</b>
7.1	Introduction . . . . .	91
7.2	Optical Properties . . . . .	92
7.2.1	Absorption . . . . .	92
7.2.2	Scattering . . . . .	93
7.2.3	Anisotropy . . . . .	93
7.2.4	Other Optical Properties . . . . .	94
7.3	Integrating Sphere Theory . . . . .	95
7.3.1	Overview . . . . .	95
7.3.2	Inverse Adding-Doubling . . . . .	97
7.3.3	Non-Linear Behavior of Detectors . . . . .	98
7.4	Double-Integrating Sphere Materials and Methods . . . . .	99
7.4.1	Experimental Design . . . . .	99

7.4.2	Sample Preparation . . . . .	100
7.4.3	Curve Fitting . . . . .	101
7.4.4	Data Analysis . . . . .	101
7.5	Double-Integrating Sphere Results . . . . .	102
7.5.1	Optical Properties . . . . .	102
7.5.2	Variation of Optical Properties with Wavelength . . . . .	102
7.6	Single-Integrating Sphere Materials and Methods . . . . .	102
7.6.1	Experimental Design . . . . .	104
7.7	Single-Integrating Sphere Results . . . . .	104
7.8	Discussion . . . . .	105
7.8.1	Double-Integrating Sphere . . . . .	105
7.9	Conclusion . . . . .	106
<b>8</b>	<b>GENERAL DISCUSSION AND CONCLUSIONS</b>	<b>108</b>
8.1	Photoacoustic Detection System . . . . .	108
8.2	Detection of Tissue Phantoms and Sensitivity Characterization . . . .	109
8.3	Melanoma Detection . . . . .	110
8.4	Optical Properties and Integrating Sphere Theory . . . . .	111
8.5	Future Directions . . . . .	111
8.6	Conclusion . . . . .	112
 <b>APPENDIX</b>		
<b>A</b>	<b>Photoacoustic Waveforms For Decreasing Concentrations Of Mi- crospheres Using Single Flow Chamber Design</b>	<b>114</b>
<b>B</b>	<b>Photoacoustic Waveforms For Decreasing Concentrations of Micro- spheres Using Customized Flow Cell Design</b>	<b>118</b>
<b>BIBLIOGRAPHY.....</b>		<b>121</b>

VITA.....	125
-----------	-----

## LIST OF FIGURES

Figure	page
2.1 U.S. death rates of various diseases presented as $10^3$ deaths. 1950–2002.	8
2.2 Schematic representation of mechanism for tumor detachment and intravasation into the blood stream courtesy of Castells <i>et. al.</i> ( <a href="http://www.intl.elsevierhealth.com/e-books/pdf/478.pdf">www.intl.elsevierhealth.com/e-books/pdf/478.pdf</a> ). . . . .	13
2.3 Schematic representation of the theory of parallel metastasis. Inspired by an article published July 2003 in <i>Cancer Cell</i> by J. W. Gray. . . .	15
3.1 A. Customized flow cell with 5 mm diameter PVDF film and positive electrode. B. Schematic showing dimensions of flow cell and incident laser direction. . . . .	23
3.2 Setup showing flow cell, ground, acrylic housing, and positive electrode.	25
3.3 Schematic of active flow cell showing incident laser light and photoacoustic event. . . . .	26
3.4 Nd:YAG Laser pumping the Vibrant Tunable Laser System. Beam path and corresponding wavelength indicated as well as internal components. . . . .	27
3.5 Schematic showing the photoacoustic mechanism as it applies to this system. The figure represents the interior of detection chamber. Single chromophore excitation. Equation for pulse time noted. . . . .	31

3.6	A. Original setup for photoacoustic detection system including photo-diode, peristaltic pump, excitation source, electrodes, and reservoir. B. Close-up of dual chamber flow cell with side excitation. Electrodes connect to the top of the flow cell. . . . .	33
3.7	A. Side view of single chamber flow cell placed in acrylic electrode housing from direction of laser light input. B. View from top of same setup. Shows dual electrode clamping mechanism on NiCr/Al plated PVDF in free space. Laser ferrule shown on far right. . . . .	34
3.8	Picture of current setup with beam path from laser. . . . .	37
3.9	Schematic representing the entire photoacoustic system. . . . .	38
4.1	Absorbance spectrum for 6.6 $\mu\text{m}$ black CML Latex Microspheres suspended in a 0.9% solution across a 150 $\mu\text{m}$ plane. . . . .	41
4.2	Standard photoacoustic waveform retrieved from pilot study of system. $1.42 \times 10^6$ $\mu\text{sphere/ml}$ solution. 510 nm excitation with no amplification. . . . .	43
4.3	Pilot study results including control and three decreasing concentrations from top right to bottom right. 510 nm excitation with no amplification. Top left: 0.9% saline control solution. Top right: $7.12 \times 10^6$ $\mu\text{sphere/ml}$ solution. Bottom left: $3.56 \times 10^6$ $\mu\text{sphere/ml}$ solution. Bottom right: $1.42 \times 10^6$ $\mu\text{sphere/ml}$ solution. . . . .	44
4.4	Pilot study photoacoustic signals normalized over control waveform. 510 nm excitation with no amplification. Top: $7.12 \times 10^6$ $\mu\text{sphere/ml}$ solution. Bottom left: $3.56 \times 10^6$ $\mu\text{sphere/ml}$ solution. Bottom right: $1.42 \times 10^6$ $\mu\text{sphere/ml}$ solution. . . . .	45
4.5	Average peak voltage given by percentage of microspheres to saline in solution for the dual chamber trials. Control included. . . . .	46
4.6	Strongest signal obtained from the single chamber detection trials (20:0.2 saline to microsphere solution ratio). 450 nm excitation with a gain of 25. A. 0.9% saline control waveform. B. $1.42 \times 10^6$ $\mu\text{sphere/ml}$ solution. . . . .	47

4.7	Smallest differentiated signal obtained from the single chamber detection trials (20:0.0001 saline to microsphere solution ratio). 450 nm excitation with a gain of 125. A. 0.9% saline control waveform. B. $7.0 \times 10^2$ $\mu$ sphere/ml solution. . . . .	48
4.8	Signal to noise ratios for peak values of detection trials using single chamber flow cell as a function of concentration. Gain of 25 shown on left. Gain of 125 shown on right. Linear function of curve fit given in red. . . . .	49
4.9	Dimensions of dual chamber flow cell that result in a photoacoustic response at 3.0 $\mu$ s. Includes single chromophore excitation. Second chamber not shown. . . . .	51
4.10	Close up of an active Spectrocell customized flow in the detection system. Top of the figure shows the x-z mount for aligning the flow cell. Ground electrode present on PVDF film. Positive electrode in solution. Incident laser light shown. . . . .	54
4.11	The effect of saline concentration on peak voltage. . . . .	55
4.12	Strongest signal obtained from the custom flow cell detection trials (1600:1 saline to microsphere solution ratio) shown on right. Corresponding 1.8% saline control waveform given on left. 450 nm excitation with a gain of 25. 11.5 mJ incident energy. . . . .	56
4.13	Weakest differentiated signal obtained from the custom flow cell detection trials (200000:1 saline to microsphere solution ratio) shown on right. Post-experimental 1.8% saline control waveform given on left. 450 nm excitation with a gain of 25. 11.5 mJ incident energy. . .	57
4.14	A. Signal to noise ratio for all data points taken in customized flow cell trials at 1.0 $\mu$ s. Linear equation given in red. B. Close up of four smallest concentrations in A. . . . .	58
4.15	A. Signal to noise ratio for all waveforms measured at 3.0 $\mu$ s with linear curve fit. B. Linear curve fit of lowest concentrations from A measured at 3.0 $\mu$ s. Linear equation given in red. . . . .	59

5.1	Representation of Ficoll-Hypaque blood separation indicating location of peripheral blood mononuclear cell layer. . . . .	67
5.2	A. Control waveform of a 0.9% saline solution. Amplification x 25. 450 nm excitation. B. Photoacoustic results for a control agranulocyte cell suspension with no addition of microspheres. Amplification x 25. 450 nm excitation. . . . .	69
5.3	Photoacoustic waveform of a post-PBMC-isolation addition of microspheres. $3.56 \times 10^6$ $\mu$ spheres/ml mononuclear cell solution. Amplification x 25. 450 nm excitation. . . . .	70
5.4	Photoacoustic waveform of a pre-PBMC-isolation addition of microspheres. $7.124 \times 10^6$ $\mu$ spheres/ml mononuclear cell solution. Amplification x 25. 450 nm excitation. . . . .	71
5.5	A. Control waveform of a 3 ml plasma/ 10 ml saline solution. Amplification x 25. 595 nm excitation. B. Photoacoustic waveform of the same plasma solution with the addition of $1.49 \times 10^8$ ( $6.0 \times 10^6$ per ml) black latex microspheres. Amplified x 25. 595 nm excitation. . .	72
6.1	Chemical structure of two most abundant types of melanin (top). Absorption spectrum given as a function of absorption coefficient for melanosomes (bottom). . . . .	77
6.2	Microscopic view of cultured melanoma cells after Hematoxylin and Eosin staining and cytopsin analysis. . . . .	79
6.3	Examples of Fontana Masson Melanin Staining. A. Arrow points to large, darkly pigmented melanoma cell. B. Mutated aneuploid cell producing melanin with three nuclei. C. Group of malignant melanoma cells with light pigmentation. Arrow points to melanin granule. . . . .	82



6.4	Chemical structure and absorbance spectrum of phenol red at various pH. Absorbance spectrum on left is from The Sigma-Aldrich Handbook of Stains, Dyes, and indicators. Spectrum on right is from <i>in vitro</i> spectroscopy studies of 0.8 mM solutions of phenol red performed by Baylor <i>et. al.</i> Phenol red is a key chemical component of RPMI cell culture medium used to culture melanoma. . . . .	83
6.5	A. 1.8% saline control waveform. B. $7.124 \times 10^6$ $\mu$ sphere/ml white microsphere waveform displaying the pyro-electric effect. Excited at 450 nm with 9.5 mJ incident energy. Gain of 25. . . . .	85
6.6	A. 10 ml RPMI Culture Medium/10 ml 1.8% Saline solution excited at 450 nm. 9.5 mJ incident energy. B. 10 ml RPMI Culture Medium/10 ml 1.8% Saline solution excited at 620 nm. 7.5 mJ incident energy. . . . .	86
6.7	A-B. Photoacoustic waveforms for metastatic melanoma. $1.43 \times 10^5$ cells/ml 1.8% saline. 450 nm excitation. 11.6 mJ incident energy in A, 9.5 mJ in B. C. Photoacoustic waveform for melanoma with 620 nm excitation. $1.53 \times 10^5$ cells/ml. 6.7 mJ incident energy. D. Post-experiemntal control waveform. 1.8% saline solution. 450 nm excitation with 9.5 mJ incident energy. . . . .	87
7.1	Depiction of experimental setup to determine absorption coefficient using Beer's Law. . . . .	93
7.2	A. Representation of isotropic scattering ( $g=0$ ). B. Representation of complete forward scattering ( $g=1$ ). . . . .	94
7.3	A schematic representation of possible light interactions with a sample. . . . .	96
7.4	A schematic representation of a double integrating sphere setup. . . . .	96
7.5	Polynomial curve fit of photodiode detectors for double-integrating sphere setup. . . . .	99
7.6	Optical properties as a function of wavelength using double-integrating spheres and 1 mm samples. A. Absorption coefficient. B. Scattering coefficient. C. Anisotropy. D. Reduced scattering coefficient. E. Optical depth. F. Scattering albedo. . . . .	103



## LIST OF TABLES

Table	page
7.1 Optical properties of black latex microspheres using a double-integrating sphere method and a 1 mm cuvette. . . . .	102

# PHOTOACOUSTIC DETECTION OF METASTATIC MELANOMA IN THE HUMAN CIRCULATORY SYSTEM

Ryan Michael Weight, M.S.

Dr. John A. Viator, Thesis Supervisor

## ABSTRACT

Detection of disseminating tumor cells among patients suffering from various types and stages of cancer can function as an early warning system, alerting the metastatic spread or recurrence of the disease. Early detection of such cells can result in preventative treatment of the disease while late stage detection can serve as an indicator of the effectiveness of chemotherapeutics. The prognostic value of exposing disseminating tumor cells poses an urgent need for an efficient, accurate screening method for metastatic cells. We propose a system for the detection of metastatic circulating tumor cells based upon the thermo-elastic properties of melanoma. The method employs photoacoustic excitation coupled with a detection system capable of determining the presence of disseminating cells within the circulatory system *in vitro*. Detection trials consisting of tissue phantoms and a human melanoma cell line resulted in a detection threshold on the order of 10 individual cells, thus validating the effectiveness of the proposed mechanism. Optical properties of latex microsphere tissue phantoms and human melanoma cells were derived using integrating sphere measurements and an inverse adding doubling algorithm for studies of comparison. Melanoma cells were introduced into human blood *in vitro* to mimic a metastatic environment. Results imply the potential to assay simple blood draws from healthy and metastatic patients for the presence of cancerous melanoma providing an unprecedented method for routine cancer screening.

# Chapter 1

## Introduction to Photoacoustics

### 1.1 History

Photoacoustics is the study of light induced pressure waves, or ultrasound, for the determination of absorbers through the analysis of dynamic wave response. Photoacoustics, as it is known and used today, is a relatively new innovation in the field of optical diagnosis. Contrary to other optical techniques which model biological features by analyzing the effects of turbid media on the scattering and absorption properties of light, photoacoustics has the ability to model features through the detection of acoustic waves as opposed to optical detection. There have been many advancements in photoacoustics within the past 15 years including the use of piezoelectric films as ultrasonic detectors and the implementation of high intensity pulsed laser systems for incident light modulation. These advancements have allowed the field of photoacoustics to expand in many directions, offering new imaging and detection methods by providing cutting edge technology to both the scientific and medical fields.

Light's ability to produce ultrasonic waves in gases has been known and studied since the 19th century when Alexander Graham Bell first observed it while working on a way to transmit sound without any cables. He discovered that if a focused beam of light was rapidly interrupted and allowed to fall on a Selenium block, an audible signal could be picked up through a hearing tube [1]. Following Bell's discovery, the field lay dormant for 50 years until the discovery of the microphone made it possible

to enhance the measurements. Since the inception of light modulated acoustics, the technology has been sparsely studied with no apparent practical use until recent years. Currently, photoacoustics is being implemented in numerous clinical applications ranging from cancer detection and tissue ablation to blood flow analysis and optical depth determination.

This particular study exploits photoacoustic technology for the purpose of cancer screening in the human blood *in vitro*. This thesis presents information on photoacoustics as it relates to cancer and shows results for the detection of metastatic cancer cells by a proposed photoacoustic mechanism.

## 1.2 Theory

Photoacoustics, also referred to as laser-induced ultrasound, uses short duration pulsed light to create ultrasonic acoustic waves in an optically absorbing medium. These acoustic waves are generated based upon the thermoelastic properties of targeted chromophores. Chromophores by definition are atoms or molecules within a compound that are responsible for the color of the given compound. Inherently, they present color by partially absorbing wavelengths composing the visible spectrum of incident light. The non-absorbing wavelengths are subject to scattering and reflectance as determined by the composition of the particular chromophore, thus emitting the color representative of the reflected wavelengths. Photoacoustics is based upon the absorbed portion of incident light. As light is absorbed by irradiated chromophores, the optical energy gets converted into kinetic thermal energy trapped within the chromophore and subsequent thermal expansion of the atoms ensues. Thermoelastic expansion occurs when the condition of stress confinement is achieved by depositing direct energy unto a chromophore in a continuous manner such that energy is unable to propagate away except by means of eventual convection with surrounding mediums [2]. This condition is expressed in Equation 1.1

$$t_p < \delta/c_s \tag{1.1}$$

where  $t_p$  is the laser pulse duration,  $\delta$  is the absorption depth of laser energy, and  $c_s$  is the speed of sound in the medium [3]. It is assumed that the absorption depth,  $\delta$  is smaller than the diameter of the laser beam.

Transient thermoelastic expansion can be achieved by irradiating with short pulses of concentrated laser light allowing for elastic expansion and contraction of an absorbing molecule. This thermoelastic expansion and subsequent contraction results in the production of longitudinal ultrasonic waves propagating in all directions away from the thermally excited medium of interest. Stronger heat generation will produce a stronger acoustic wave via greater thermoelastic expansion. Therefore, a strong optical absorber emanates a strong acoustic wave. Conceptually, photoacoustics can be described as pulsed laser energy quickly absorbed by a scattering medium such that transient thermoelastic expansion results in formation and propagation of acoustic energy. Thermoelastic expansion, as used in photoacoustics, can be described by Equation 1.2 (assuming a pure absorber where  $\delta = 1/\mu_a$ )

$$p(z) = \frac{1}{2}\mu_a\Gamma e^{-\mu_a z} \quad (1.2)$$

where  $p(z)$  represents pressure at depth  $z$ ,  $\mu_a$  is the optical absorption coefficient of the tissue,  $\Gamma$  is the Gruneisen coefficient, which denotes the fraction of optical energy which is converted to acoustic energy. It is temperature dependent and is equal to 0.12 at room temperature for most tissue. [2–4].

The total photoacoustic energy is directly related to chromophore content. The amount of thermoelastic expansion as given in Equation 1.2 is directly related to the absorption coefficient ( $\mu_a$ ) of the chromophore. The absorption coefficient is derived from the molar extinction coefficient and chromophore concentration as described in Equation 1.3

$$\mu_a = 2.3\epsilon c \quad (1.3)$$

where  $c$  is the concentration of specific chromophore and  $\epsilon$  is the molar extinction coefficient of the compound.

Acoustic pressure is proportional to energy per unit volume given as Joules per  $\text{cm}^3$ . Since the spot size is held constant, the integral of pressure over depth yields

the total absorbed energy as given in Equation 1.4

$$E_a = \int_0 p_0(z) dz \quad (1.4)$$

where  $E_a$  is the total absorbed energy by the chromophore and  $p_0(z)$  is the initial pressure as a function of depth  $z$ . The integral gives a quantity expressed in terms of  $J/cm^2$ , so the total energy detected is related to this quantity by the detector active area. [2] The amount of energy ( $E_a$ ) absorbed is directly related to the amount of incident light energy upon the medium (also given as  $J/cm^2$ ) to a certain limit determined by the absorption capacity of the specific chromophore.

Detection of these minute photoacoustic waves is equally as important as their production. Photoacoustic detection methods can vary drastically from one experimental design to another. However, the concept most commonly employed utilizes a piezoelectric copolymer in electrical connection with two electrodes, one being the ground wire and the other measuring the positive voltage change of the film. These films are commonly constructed of polyvinylidene difluoride, or PVDF, and may or may not incorporate an aluminum coating that acts as a conducting element. As longitudinal acoustic waves propagate towards the film, pressure accumulates according to the magnitude of each pressure wave. As these pressure waves come into contact with the piezoelectric film, the lateral surface of the film impacted by the pressure wave shifts, disrupting the entropically stabilized bilayer. The disruption of the polymer layer causes an electrical charge to form between the two copolymer layers that can be detected by two conducting electrodes as a voltage spike (Photoacoustic phenomena, as applied to this thesis, will be described further in Chapter 3). Using information on the amplitude of the voltage spike and the time difference between sending a laser pulse and receiving the pressure wave, chromophore density can be quantified in addition to deducing the relative location of the chromophores to that of the PVDF film as described in Chapter 4 [5].



## 1.3 Applications

In today's fast paced technological environment, there is a potent interest in the application of photoacoustics for a number of different medically and non-medically related endeavors. The large majority of this interest is based in imaging and detection modalities. For example, photoacoustic imaging has been used to study tumor heterogeneity and molecular identification as well as being implemented in image guided biopsies. Photoacoustics has been used for extensive studies of vasculature *in vivo* which has developed into tumor diagnosis by analysis of neovascularization, prognostic determination of traumatic brain injury, and *in vivo* quantification of blood oxygenation among others. Photoacoustic tomography has been used to analyze gene expression *in vivo* as well as classifying and assessing kidney disease. New clinical detection methods are arising from photoacoustic technologies including the early detection of dental caries and the topic of this thesis. The newest wave of photoacoustic technology combines nanoparticle technology with photoacoustic imaging to enhance images and induce accelerated thermolysis. This mentions a few of the many recent applications of photoacoustic technology. Given the breadth of current photoacoustic technologies, it should be noted that to date there exists no photoacoustic studies paralleling the research presented in this thesis. [6]

# Chapter 2

## Introduction to Cancer

### 2.1 History

Cancer has plagued all multicellular organisms since the beginning of time. In fact, paleopathologists have found melanotic masses and diffuse metastases in Incan mummies dating back to the 4th century B.C. [7]. Indeed cancer, specifically melanotic carcinomas for the purposes of this study, has proven to be an elusive adversary in the field of medicine.

Cancer is derived from a Latin root word meaning *crab*. Cancer is the common term for neoplasms, or tumors, that are malignant. Tumors arise from a large number of sequential mutations within a cell's genome that are often prompted by cellular or environmental stress on the cells. Simple mutations are commonplace within the genome of a cell. Multiple established cellular mechanisms are in place to correct such mutations. However, once these mechanisms are overcome, the cells can lose the ability to regulate cellular growth and proliferation. Cancer cells, unlike normal cells, lack contact inhibition which limits their ability to control growth via intra-cell communication.

A number of key oncogenes and tumor suppressor genes are present in all cells. These cells regulate mechanisms that are key for a cell's survival such as apoptosis, senescence, and cell cycle. Inherently, these genes serve as gatekeepers to disease progression. If an oncogene is mutated and permanently activated or a tumor suppressor gene is rendered dysfunctional, cells lose the innate ability to communicate

which leads to the formation of tumors. Like benign tumors, malignant tumors do not respond to body mechanisms that limit cell growth. Unlike benign tumors, malignant tumors consist of undifferentiated, or unspecialized, cells that show an atypical cell structure and do not function like the normal cells from the organ from which they derive. Malignant tumors are cancers and can metastasize to other locations if allowed to progress, as described later in this chapter.

The epidemiology of cancer is astonishing. According to reports presented by the *American Cancer Society*, in the year 2000 alone, 10 million new cases of cancer were reported world wide. 1.5 million of these new cases were reported in the U.S., not including the 1 million *in situ*, or early stage, skin cancers presented each year within the U.S. Cancer accounted for 6 million deaths worldwide in the year 2000. Over 500,000 cancer related deaths occur each year in the U.S., making up nearly 23% of total yearly deaths. A 2005 study by the *American Cancer Society* shows that the number of cancer deaths has overtaken the number of deaths related to heart disease in recent years, making cancer the primary cause of death in the U.S.

## 2.2 Challenges

Figure 2.1 shows the cancer death rates 1950-2002 compared to that of other prevalent diseases. It is clear that advances in medicine over the past 50 years have had a dramatic impact on most common diseases. However, cancer death rates have remained unchanged over this course of time. This is not to say that there have not been advances in cancer treatments, only that these advances have worked to increase a patient's life span but have not succeeded in increasing overall survival rates. These findings can be primarily attributed to three short-comings in the field of oncology: insufficient detection methods, a lack of preventative treatment options, and relapse of the disease.

Currently, there exists no accurate early screening method for cancer, leaving detection up to the patient in the form of overt signs of disease. An improved method for both early and late stage cancer detection would greatly benefit the field of oncology by allowing for earlier treatment options thereby improving the

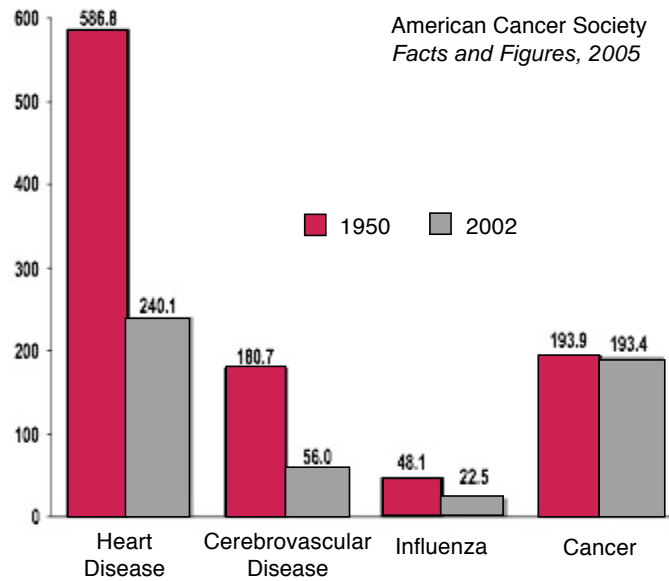


Figure 2.1: U.S. death rates of various diseases presented as  $10^3$  deaths. 1950–2002.

prognosis of the patient. Secondly, a lack of preventative treatment options to curb the development of disease previous to its inception proposes a yet unresolved problem. Some studies have been conducted addressing natural chemopreventative agents through dietary phytochemicals and some synthetic oxidative stress reducers but there is yet to be a safe method identified for the prevention of cancers [8, 9]. Another major problem that must be addressed is that of relapse. Recurrence of disease following primary treatments remains a monumental task for physicians and patients to overcome. Recurrence of disease results from disseminated or metastatic cells that have broken off of the primary tumor and relocated at a distant site. Relapse often occurs after successful treatment of the primary disease, however, in the end cancer remains the cause of death.

This only names a few of the obstacles to be overcome in order to improve upon the current trends of the disease. This work provides a method for the detection of both early and late stage, or metastatic, disease with the hope of eventually meeting some of the challenges set forth by cancer today, specifically that of early detection and detection of potential relapse of disease.

## 2.3 Melanoma

### 2.3.1 Overview

There are four basic types of cancer: Carcinomas, which describes any malignant cancer derived from an epithelial origin including any tumor formed from the epithelial lining of an organ; Sarcomas, which describes any malignant tumor derived from a mesenchymal origin including fibroblasts, lipids, bone, cartilage, endothelial cells, smooth muscle cells, and skeletal muscle cells; Lymphomas and Leukemias, which are composed of malignant B-cells and T-cells and can be either circulating, a leukemia, or in a solid tumor state, a lymphoma; finally, Malignant Melanoma, which is derived from melanocytes. It is believed that the cancer detection system proposed by this thesis has the ability to detect any cells that contain melanin (as described in following chapters). This would primarily include melanotic melanomas. It should be noted that only 90% of melanomas are thought to be melanotic, or contain melanin. Approximately 10% of said cancers are amelanotic which would render the proposed detection mechanism ineffective (see Chapter 6).

Cancer of the skin is the most common of all cancers, accounting for more than 50% of all cancers. According to the *American Cancer Society*, melanoma accounts for about 4% of skin cancer cases but causes a large majority of skin cancer deaths. Melanoma tends to occur at a younger age than most cancers with nearly half of all melanomas found in people under the age of 57. Adolescents can have melanoma also. About 1 of every 30,000 girls aged 15 to 19 will develop melanoma. For boys of this age, the rate is about 1 of every 15,000.

*The American Cancer Society* estimates that about 62,190 new melanomas will be diagnosed in the United States during 2006. Malignant melanomas are extremely dangerous. Since 1973, the mortality rate for melanoma has increased by 50%. Among white men and women in the United States, incidence rates for melanoma increased sharply at about 6% per year from 1973 until the early 1980s. According to the *American Cancer Society*, approximately 7,910 people in the United States are expected to die from melanomas during 2006.

The remainder of this section details malignant melanoma to provide a better understanding of the progression of disease. Melanoma is discussed specifically since it composes the most relevant type of cancer for implementation in the proposed cellular detection device. Melanoma is also used as the test subject for the device.

### **2.3.2 Types of Melanoma**

There are six known types of melanoma: amelanotic melanomas, lentigo maligna melanoma (LMM); superficial spreading melanoma (SSM); nodular melanoma (NM); acral lentiginous melanoma (ALM); and mucosal lentiginous melanoma (MLM). Amelanotic melanomas lack pigment and constitute approximately 1% of melanomas. LMM, SSM, and NM compose 85% of melanomas with superficial spreading melanoma consisting of 70% of all known melanomas. SSM generally arises from a pre-existing lesion of the skin and slowly progresses eventually presenting irregular borders and surfaces. [7]

### **2.3.3 Disease Progression**

Malignant melanoma usually arises from precursor lesions such as dysplastic nevi, congenital nevi, or from cutaneous melanocytes. Visible precursor lesions can be characterized by the appearance of large brown macular moles with irregular borders, often variable shades of brown. Many occurrences of melanoma arise from melanocytes as antecedent lesions. Melanocytes grow from the neural crest and migrate to their final destinations, generally at the epidermal-dermal junction of the skin. Antecedent lesions of melanoma are often derived from atypical melanocytic proliferations. Melanomas progress in two distinct growth phases, radial and vertical, from their point of origin. Radial growth, or superficial spreading, normally occurs above or below the basal lamina and is not associated with the ability to metastasize. The vertical growth phase allows the malignant cell population to invade the dermis, thus providing the opportunity for metastasis. [7]

## 2.4 Staging

Grading and staging differ for each type of cancer based upon the characteristic differentiation of each type of disease. Prognostic features of melanoma are characterized by a microstaging method known as Clarks level of invasion where lesions are defined by dermal invasion and rated as stage I-IV. Stage I represents poorly differentiated cells often referred to as *in situ*. Stage II refers to slightly differentiated tumor with minor dermal invasion while stage III represents invasive tumors with localized metastasis. Stage IV stands for fully differentiated, fully invasive tumors with a size greater than 4mm and distant metastases [7]. The vertical size of the primary melanoma is indicative of the presence of metastatic disease and subsequent overall patient survival rates. Staging can be further classified into the categories "T", "N", and "M" for level of invasion, extent of lymph node involvement, and metastasis, respectively. Each sub-category can be ranked by Clark's I-IV staging dependent upon the severity of the disease. The number of lymph nodes containing metastatic tumor is the most important factor in determining the prognosis and severity of the disease [7].

## 2.5 Metastasis

Metastasis is a hallmark of malignant disease. It is often the reason for relapse in cancer patients and is the cause of 90% of cancer related deaths. At least 60% of cancer patients have microscopic or clinically evident metastases at the time of primary tumor treatment [10]. Traditionally, metastasis is thought to be the end stage of disease or the most advanced form of cancer. Although this prevailing view has been challenged and the exact mechanism of metastasis remains debatable [11–14], it is well known that devising a method for stopping the spread of metastasis would have a revolutionary impact on cancer survival rates. Preliminary to eliminating metastasis, the disseminated disease must first be detected. The device proposed in this thesis may prove to be a key component in both the early and late stage detection of disseminated tumor cells. This section details the biological pathway

leading to overt metastasis as well as conflicting views as to the role of metastatic disease.

### **2.5.1 Transformation**

Metastasis is a cascade of linked sequential steps involving multiple host-tumor interactions leading to dissemination [15]. Cancer cells possessing multiple genetic abnormalities grow unregulated and eventually lose the ability to adhere to one another [15], resulting in the spread of free carcinomic cells. These cells can easily migrate through the tumor membrane and extra-cellular matrix and travel to new sites via the lymphatic and/or blood systems [15]. When cancer cells enter the lymphatic system, they travel to the lymph nodes before entering the blood stream. Subsequent progression allows for a new focus to undergo neovascularisation at other sites [15]. However, according to Chambers [16], the majority of tumor cells that leave a primary human tumor fail to give rise to metastases resulting in a large number of single disseminated cells circulating within the blood stream. Chambers also noted that most metastatic cancer cells that enter the blood stream do not undergo destruction by the immune system, most likely due to a lack of recognition pathways between the tumor cells and antibody targeting.

### **2.5.2 Intravasation and Extravasation**

To initiate the metastatic process, tumor cells must lose the ability to adhere to one another or overcome attachment by breaking bonds or losing functionality between cadherins and integrins of the cell-extracellular matrix (ECM) [10]. Cadherins are transmembrane glycoproteins that mediate calcium-dependent cell-cell adhesion in normal tissue. Integrins are a family of heterodimers (VLA-1 to VLA-6) that serve as receptors for ECM components including recognition of vascular cell adhesion molecules and cellular communication [10]. Following detachment from the ECM, neoplastic cells must penetrate the basement membrane and then invade the interstitial stroma by active proteolysis. Subsequently, intravasation requires tumor cell invasion of the subendothelial basement membrane [10]. In a similar manner, only



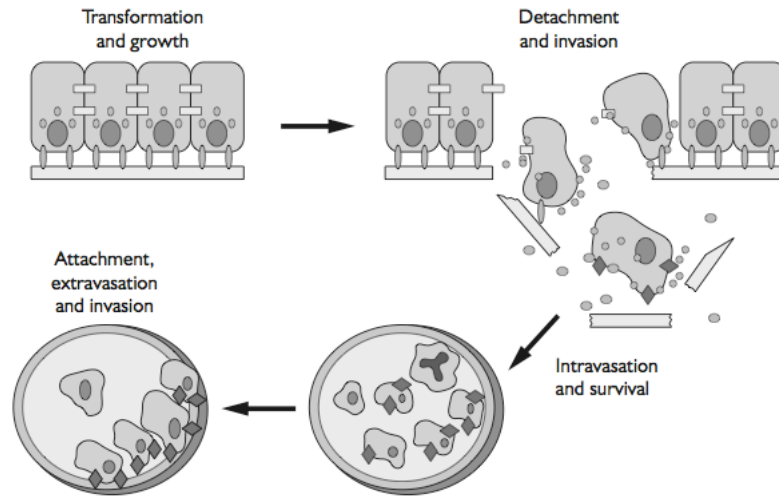


Figure 2.2: Schematic representation of mechanism for tumor detachment and intravasation into the blood stream courtesy of Castells *et. al.* ([www.intl.elsevierhealth.com/e-books/pdf/478.pdf](http://www.intl.elsevierhealth.com/e-books/pdf/478.pdf)).

reversed, tumor cell extravasation occurs allowing for the metastatic disease to exit the blood or lymph stream and establish a metastatic site at a distant location. Figure 2.2 shows a schematic representation of both intravasation and extravasation.

### 2.5.3 Secondary Tumor Formation

In order for cells to successfully establish a metastatic colony, circulating neoplastic cells must survive immunologic surveillance, arrest at a distant vascular step, and extravasate [10]. Development of a secondary tumor site is associated with tumor-induced angiogenesis, a process that not only allows tumor growth but permits easy access to the vascular compartment, favoring metastatic spread [10]. Once extravasted, cells must proliferate in the secondary organ in a process similar to the development of a primary site, in which several growth factors play a key role [10, 14]. Indeed, metastatic disease is a highly inefficient process. Using experimental animal models, it has been demonstrated that although several million neoplastic cells may

be released into the vascular system, fewer than 0.01% will be capable to form secondary tumors [10].

The distribution of metastases can be predicted in part by the pattern of regional venous or lymph drainage, however, tumors also metastasize to unpredictable locations [10] alluding to the theory of a pre-metastatic niche [13, 14]. Although the mechanism for the location of extravasation and why secondary tumors form where they do remains unresolved [16], studies have shown that a type of homing mechanism exists, creating a chemical *trail* that directs metastatic cells to a particular organ or site. Melanoma has a relatively unusual capability to spread to almost any organ site within the body [7]. It is therefore important to have the ability to accurately detect the potential spread of the disease through the blood stream.

#### 2.5.4 Parallel Evolution Theory

Metastatic melanoma along with other cancers are dynamic in the fact that they sometimes present without a detectable primary lesion. Cancer of Unknown Primary (CUP) accounts for up to 7% of hospitalized cancer patients that are diagnosed with distant metastases [12]. One possible explanation for this phenomena comes in stark contrast to the traditional view of metastatic tumor formation. Schmidt-Kittler *et. al.* first described studies alluding to the parallel evolution theory of metastasis [11, 12]. They show ground breaking evidence in metastatic breast cancer that distant metastases are more advanced than lymph node metastases from the primary tumor alluding to the fact that cells disseminate during early tumor development, prior to lymph node metastases, and develop independently at a distant site. This work insinuates that Unknown Primary Syndrome may result from an early disseminating cell that acquires a mutation and evolves faster than the progenitor cell, thus providing a parallel evolution theory that could redefine cancer detection as it is known today.

Figure 2.3 shows a schematic representation of the parallel evolution theory. Assuming this theory to be true, a detection method that could identify the presence of cancerous cells in the blood stream of an individual, such as the mechanism

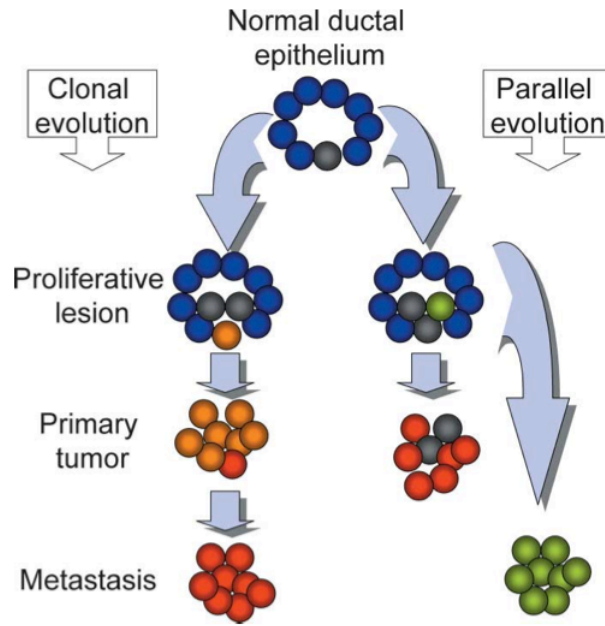


Figure 2.3: Schematic representation of the theory of parallel metastasis. Inspired by an article published July 2003 in *Cancer Cell* by J. W. Gray.

presented in this thesis, could be implemented as a regular screening method for the early detection of disease. This would allow healthy individuals to detect cancer before any outward signs of the disease presents, thus allowing for early treatment options, a better prognosis, and the ability to stop cancer before it reaches an uncontrollable state.

## 2.6 Treatment

Treatment methods for cancer are limited and constantly under review and revision. One of the most effective therapies for melanoma, after histological verification of the diagnosis, is surgical resection by wide margin excision. If possible, surgical resection is often accompanied by adjuvant therapy to further recess any possible residual tumor and for the preventative treatment of metastatic disease. Radiation and chemotherapy are two very common adjuvant treatments that may also be used to replace surgery in the event that surgical resection of the lesion is not possible or

not advised. [7]

## 2.7 Detection

The procedures for the detection and treatment of potential cancers have evolved dramatically over the past decades. However, the current therapies remain greatly unsuccessful due to the development of distant metastases. Detection of these disseminating metastases is of paramount concern for physicians and researchers today. In blood, the presence of these circulating tumor cells appears to be an early marker for recurrence and relapse of the disease [17]. The change in their quantitative number can reflect upon the chemotherapeutic sensitivity and metastatic growth activity of a tumor [17]. A sensitive method for early detection of circulating tumor cells can result in the clinical intervention of a potential relapse, which could go unnoticed or lay dormant for many years.

### 2.7.1 Clinical Methodology And Shortcomings

Currently, the most common procedure for the detection of disseminating tumor cells is assaying lymph nodes or bone marrow at the time diagnosis and surgery. Histochemical examinations involving the staining of tissues using dyes such as Haematoxylin and Eosin can be used to track the short-term spread of cells through the lymphatic system [15]. However, these methods have proven inaccurate, time consuming, and painful [15]. In addition, 15% of patients shown to be negative for lymphatic transport of metastases will develop metastatic disease in the future [15]. This occurs by either the lack of detection by current techniques or by metastatic spread directly into the blood stream. It has been shown that the disseminating cells are present in circulation in extremely low concentrations, estimated to be in the range of one tumor cell in the background of  $10^6$ - $10^7$  normal blood cells [18]. Considering that Gusterson and Ott calculated that a pathologist has a 1% chance of identifying a metastatic focus in a patient with breast cancer which is three cells in diameter [19], and that Cote *et. al.* determined that the identification of regions of metastasis by Haematoxylin and Eosin staining in the node negative lymph nodes

required the analysis of up to 144 slides/ patient [20], it is not surprising that regions of metastasis within lymph nodes are not detected.

Fisher *et. al.* compared the incidence of metastatic disease in two sets of patients with breast cancer, those who had their lymph nodes removed and those that did not [21]. This study revealed that removing the lymph nodes did not significantly alter the recurrence of metastatic disease leading researchers to believe that the haematogenic factor of metastases may play a much larger role than that of the lymphatic system [21]. Consequently, a technique is desired that can accurately detect the circulation of tumor cells on the order of 1 in  $10^6$  blood constituent cells with relative ease and at certain desired frequencies.

### **2.7.2 Current Areas of Development**

The idea of detecting circulating tumor cells in the blood of patients is not a new one. Current investigations are being conducted into new techniques for assaying blood samples thought to contain metastatic tumor cells. Three specific techniques have emerged as plausible detection methods; immunomagnetic separation (IMS) and laser scanning cytometry(LSC), cell filtration and laser scanning cytometry, and multimarker real-time RT-PCR methods. The specific details of these procedures are beyond the scope of this paper, however, a broad overview will be given as noted by Ring *et. al.* [22]

### **2.7.3 Immunomagnetic Separation and Laser Scanning Cytometry**

The IMS technique consists of subjecting a blood sample to density gradient enrichment followed by incubation with mouse BerEP4-FITC antibody followed by incubation with goat anti-mouse IgG microbeads. This method successfully marks potential carcinogenic cells and allows for magnetic separation. After separation the positive fraction is centrifuged and deposited on cytokeratin staining slides. The slides are then analyzed by laser scanning cytometry which consists of measuring cytokeratin positive cells by 488nm laser induced DNA fluorescence. Cells

showing green and red fluorescence are identified as cytokeratin positive cells, re-located, and examined by eye. This method has proven effective, however, some drawbacks include illegitimate expression of tumor cell related markers due to the heterogeneity of metastatic cells with cell surface molecules [17]. This method is also time consuming and requires trained cytologists to distinguish cells.

#### **2.7.4 Cell Filtration and Laser Scanning Cytometry**

Cell filtration followed by LSC is similar to IMS only cells are separated using a gravity filter consisting of a polycarbonate membrane. The membranes are then fixed to slides and undergo LSC as described above. This method has proven effective in the detection of disseminating cells, however, problems lie in the isolation of small amounts of cells. Also, this method does not allow for the quantification of the cells recovered by the filtration method [23].

#### **2.7.5 Reverse Transcriptase-Polymerase Chain Reaction**

Real-time RT-PCR uses density gradient enrichment and an RNA extraction to isolate target cell RNA. Primers are designed to mark the CK19, mammaglobin, and PIP peptides in target cells. Reverse transcriptase and PCR are then carried out. Emitted fluorescence is measured and compared to a fluorescence threshold for a maximum of 40 cycles. The mean normalized expression for the target gene is then given. This method also has limitations including likelihood of false-positives derived from tumor cells shedding nucleotides as opposed to full disseminated cells. Also, RNA is inherently liable, requiring blood to be quickly analyzed which is not always possible in a clinical setting [15, 22].

As reported by Ring *et. al.*, a real-time RT-PCR assay may be the superior technique reported to date for detecting circulating tumor cells as it is more sensitive than other methods mentioned and may more accurately assess the quantity of tumor cells in the blood [24]. However, if it is desirable to isolate cells for further characterization, then the cytometric approach may be preferable [24].

## 2.8 Implementing the Photoacoustic Device

It is clear that the undetected metastatic spread of primary carcinomic lesions is the leading cause of cancer deaths today. As previously described, detection of developed metastatic disease can only be diagnosed at the time of surgery through resection and analysis of lymphatic tissue. This method often proves unsuccessful when compared to patients that eventually develop recurring disease.

Given the successes and constraints of the works done by previous authors, we have set out to propose a new technique for detecting and quantifying metastatic tumor cells. We propose a novel photoacoustic mechanism employing laser induced ultrasound aiming to serve as a detection system for both early stage and metastatic disease. We propose that this mechanism may eventually be capable of detecting a quantifiable dosage of metastatic melanoma cells obtained from the isolated blood contents of a potential cancer patient. The design incorporates the use of a customized flow cell designed to detect the presence of melanoma cells, or an equivalent, by detecting photoacoustic waves produced by the cells (methods described in detail in Chapter 3). The photoacoustic signal is the direct result of a change in polarization of the acoustic film governed by the acoustic output of excited tumor cells which can be induced by laser excitation. Melanotic tumor cells can serve as light traps, which can be thought of as highly absorbing, highly scattering particles that absorb large quantities of the visible spectrum through a multiplying effect of light scattering and absorption within the cell. Therefore, the opto-acoustic properties of the broadband absorber melanin can be used to screen for the presence of potentially harmful cells circulating within the hematogenic system of both cancer patients and healthy individuals alluding to the early detection of disease.

The proposed photoacoustic mechanism offers a number of advantages over the current methods of cancer detection. It is more efficient in the speed of sample diagnosis, overall simplicity of the device, immunity from human error, and sensitivity. Using the device described in this thesis, a blood sample can be processed and analyzed for the presence of metastatic cells within thirty minutes of obtaining a sample of blood. The device is simple and relatively easy to use in that once a

solution is obtained, it only requires the addition of saline and introduction into the circulating reservoir as described in Chapter 4. Another advantage of the photoacoustic detection system is its immunity from technician error. The only human component of the analyzation process is the blood draw and separation procedures which are fairly straight forward. The actual detection and identification of the cells is automated and does not rely on the discretion of a trained technician which inherently contains human error as described in Section 2.7.1. Sensitivity is yet another benefit of the proposed mechanism which will be discussed in more detail in the following chapters.



## Chapter 3

# Photoacoustic Detection System

### 3.1 Introduction

This work proposes a detection system for accurately identifying the presence of melanotic cancer cells within the human hematogenic system. The method employs photoacoustic technology as an *in vitro* method of screening and quantifying disseminating tumor cells for the purpose of cancer detection or as a method for determining the effectiveness of chemotherapeutics. This device offers a way of improving upon standard detection protocols while alleviating many of the problematic symptoms of alternative detection methods previously described in Section 2.8. The goal of the photoacoustic detection system is to have the ability to accurately pinpoint both early and late stage disseminated cancerous cells present within the bloodstream. This would provide a relatively pain-free alternative to clinical protocols of surgically based detection methods as well as offer a much needed mechanism for the early detection of disease. It is proposed that this detection system may provide a method for precise and unprecedented detection thresholds by identifying single melanoma cells in the presence of millions of secondary blood constituent cells.

This chapter describes the inception and development of the device as well as providing details of the materials and makeup of the detection system.

## 3.2 Development and Design

The original idea for the photoacoustic detection system was conceived by the collaborative works of Dr. Paul S. Dale and Dr. John A. Viator. The overall design of the device was implemented by the author of this thesis. The concept of the detection device is to provide a flow system through which solutions of interest may be introduced for the purpose of exciting single, melanotic cancer cells by pulsed laser excitation. In order to do so, a transparent flow cell, or excitation chamber, conducive to laser excitation must be incorporated into the system. A reliable acoustic detection system must also be implemented to capture photoacoustic waves. A signal element is necessary to convert acoustic waves produced by melanotic excitation to voltage signals that can be displayed for analysis. The remainder of the chapter gives an in depth description of the photoacoustic system including the excitation device and its components.

## 3.3 Detection Apparatus

The detection apparatus encompasses the excitation chamber, or flow cell, acoustic detection mechanism, signal propagation, and the flow system.

### 3.3.1 Flow Cell

The flow cell refers to the chamber where laser excitation and acoustic wave propagation and detection occurs. Following a number of different designs, a Spectrocell customized flow cell (Oreland, PA) was selected as the most efficient form for an excitation chamber. Figure 3.1A shows the Spectrocell flow cell separate from the rest of the system. The flow cell consists of a 2 x 10 mm horizontal aperture with a vertical height of 45 mm for a total fluidic volume of 0.9 ml. The top and bottom of the flow chamber are tapered to cylindrical ports with an inner diameter of 2.7 mm and an outer diameter of 4.95 mm. These ports serve to connect the cell to the pump tubing. A cylindrical hole measuring 5 mm in diameter is cut laterally from one side of the flow cell where a piezoelectric film is affixed as shown in Figure

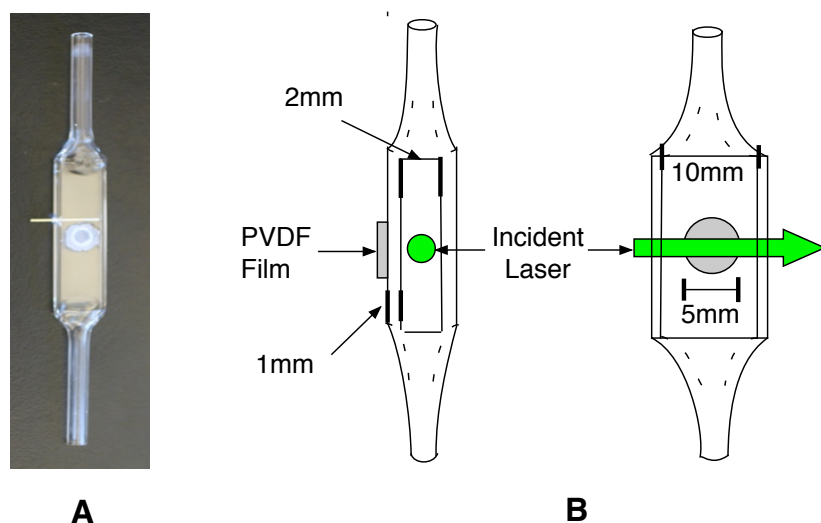


Figure 3.1: A. Customized flow cell with 5 mm diameter PVDF film and positive electrode. B. Schematic showing dimensions of flow cell and incident laser direction.

3.1B. A second small hole is drilled into one side of the 2 mm face of the flow cell for insertion of an electrode. High intensity laser light is focused into the 2 mm side of the flow cell, opposite that of the positive electrode, at a height equal to that of the detection aperture.

### 3.3.2 PVDF Copolymer Film

A piezoelectric film is employed as the acoustic wave detector. The film is cut to a diameter slightly larger than the 5 mm diameter aperture on the 10 mm side of the flow cell and is affixed to the outside of the flow cell by a 100% silicone sealant (DAP Inc., Baltimore, MD). The piezoelectric film is a 100  $\mu\text{m}$  polyvinylidene difluoride (PVDF) copolymer film (Ktech Corp., Albuquerque, NM).

### 3.3.3 Electrodes

Copper electrodes were used for both positive signal detection and grounding although different mechanisms were used for both. The positive electrode is a stripped

0.6 mm diameter copper wire (Consolidated Inc., Franklin Park, IL) approximately 17 mm in length inserted into the 2 mm side of the flow cell as previously seen in Figure 3.1A. The electrode is sealed with 100% silicon sealant. It extends the horizontal length of the flow cell and leaves an external lead which is connected to an alligator clip for transfer to display.

The negative electrode, or ground, consists of a thin, 4 mm diameter copper plate (Small Parts Inc., Miami Lakes, FL) soldered to a 3.5 mm diameter bare micro-coaxial cable (Microstock Inc., West Point, PA) that measures 13 mm in length. The cable is in turn soldered to a 31-221-VP BNC connector (Jameco Electronics, Belmont, CA) which connects to a grounded RG 58 coaxial cable (Pomona Electronics, Everett, WA). The BNC connector screws into a cut 50.8 mm diameter cast acrylic housing (Small Parts Inc., Miami Lakes, FL) applying the flat copper plate flush against the external side of the PVDF film, thus providing a ground to one side of the piezoelectric film. The acrylic housing, ground, and flow cell are shown below Figure 3.2. A schematic of the flow cell, including laser excitation and acoustic propagation, is shown in Figure 3.3.

### 3.3.4 Flow System

Experimental solutions are pumped through a loop by a Masterflex L/S Economy Drive peristaltic pump (Cole-Parmer Instr., Vernon Hills, IL) and L/S 14 platinum-cured silicon tubing (Cole-Parmer Instr., Vernon Hills, IL). A peristaltic pump was used so that no mechanical pump elements directly interacted with the samples. 15 ml solutions are entered into the detection system through a 13.75 cm<sup>3</sup> open reservoir. The peristaltic pump provides negative pressure, circulating fluid out of the reservoir, the the detection chamber, and returning it back to the reservoir. The silicon tubing is size fitted to the output and input ports of the flow cell. Experimental solutions circulate at a speed averaging 9 ml/minute, allowing for cells of interest to be excited 235 times when vertically crossing the beam path of a 5 ns pulsed laser with a 1 mm spot size (average conditions for given setup).

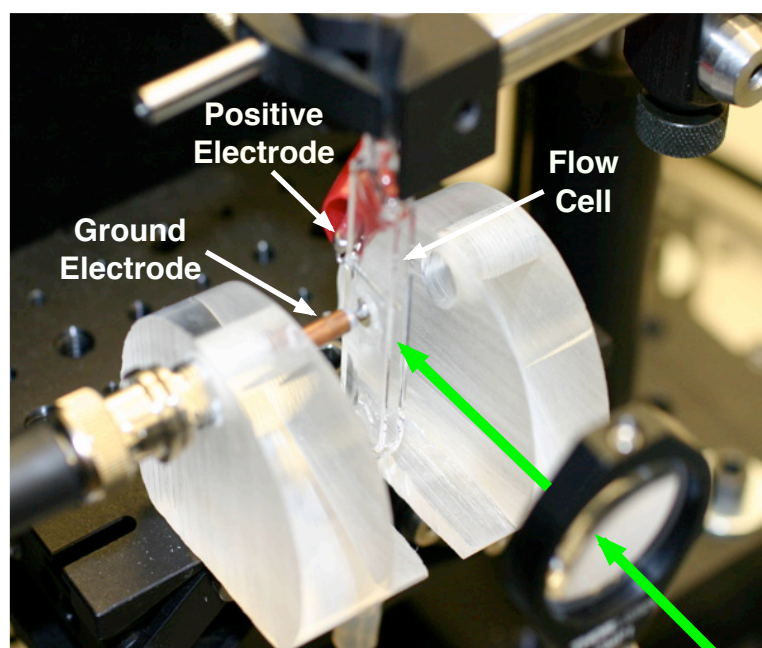


Figure 3.2: Setup showing flow cell, ground, acrylic housing, and positive electrode.

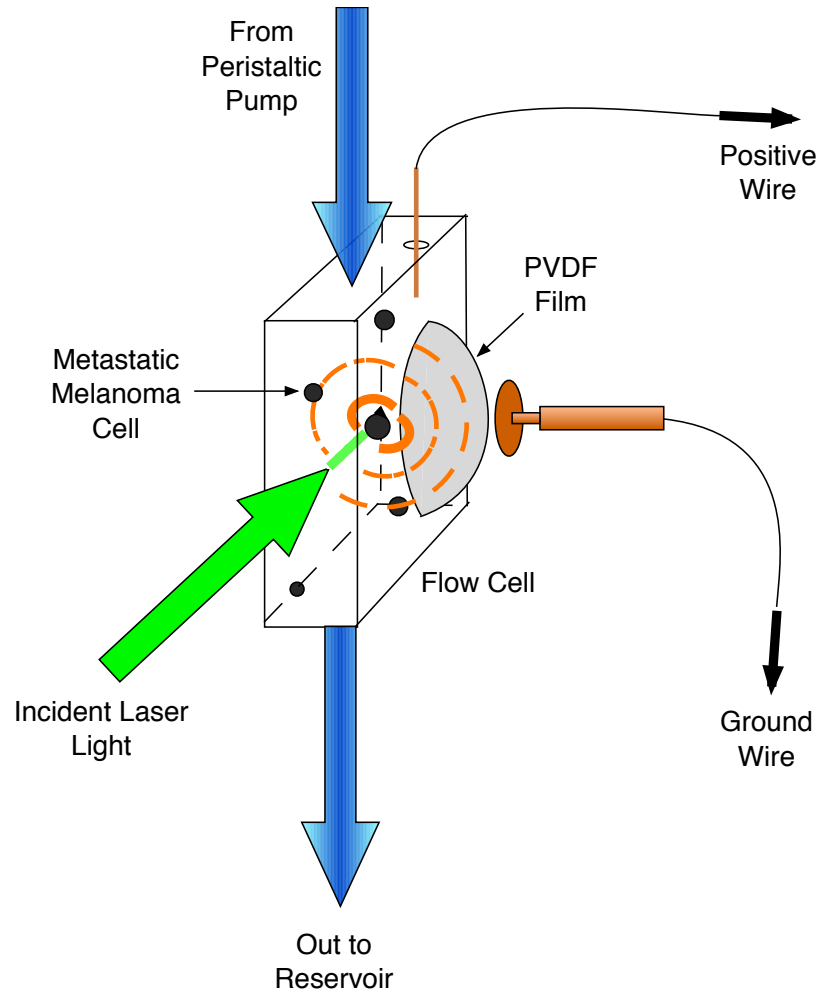


Figure 3.3: Schematic of active flow cell showing incident laser light and photoacoustic event.

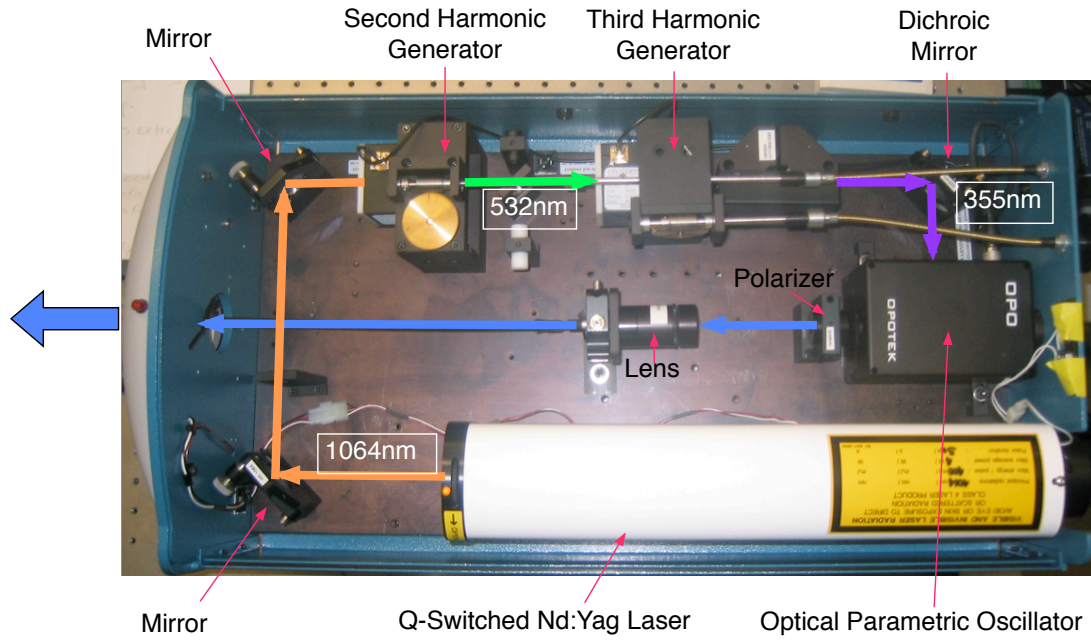


Figure 3.4: Nd:YAG Laser pumping the Vibrant Tunable Laser System. Beam path and corresponding wavelength indicated as well as internal components.

### 3.4 Laser

Photoacoustic excitation is made possible by a sharply focused pulsed laser system. The laser is a Q-switched, frequency tripled Neodymium-doped Yttrium Aluminum Garnet or Nd:YAG laser (Quantel, LES ULIS cedex, France) housed in a Vibrant Integrated Tunable Laser System (Opotek, Carlsbad, CA). The Nd:YAG is a pumped laser that emits 1024 nm pulsed laser light by an optical switch dubbed the "Q-switch" which acts as a gate to release light at the maximum neodymium ion inversion. Once released, laser light is reflected by two mirrors within the Vibrant into a second harmonic generator where the wavelength is converted to 532 nm then into a third harmonic generator where it is converted to 355 nm. The 355 nm laser light is pumped into an Optical Parametric Oscillator or OPO. Figure 3.4 shows the internal layout of the Vibrant including the beam path and components.

### 3.4.1 Optical Parametric Oscillator

The OPO allows for the output of variable wavelengths ranging from 410 nm to 710 nm. For the purpose of these experiments an excitation wavelength of 450 nm was used for reasons further described in Section 4.6. The OPO contains a Beta Barium Borate crystal that tunes by the electronically controlled rotating of the crystal with respect to beam. The OPO converts the 355 nm input wavelength into two beams, the signal and the idler, each having longer wavelengths than the input beam. A cavity termed the Double Resonating Oscillator oscillates both the idler and the signal wavelengths while the tuning angle of the crystal determines a phase match that produces the desired wavelength which is then released from the cavity. The tuning angle is controlled by a stepping motor operated by an external, computer generated program. Additional information regarding optical parametric oscillators can be referenced from S. E. Harris *et. al* [25].

### 3.4.2 Fiber Coupling

Following the OPO, the beam passes through a polarizer and is coupled by a lens into a standard 1.5 mm diameter silica fiber for light transfer. The fiber was originally used for all experiments but became complicated by breaks and loss of energy resulting in poor results. Reconstruction of the experimental setup led to the development of an "open" delivery system, exciting the target cells directly from the Vibrant output port following the polarizer. This increased energy input into the system from a range of 7.0- 8.0 mJ output from fiber to 11-12 mJ direct output from polarizer, the results of which are evident in Chapters 4 and 6.

### 3.4.3 Beam Focusing and Profiling

A tradeoff exists between radiant energy and sufficient radiant exposure. One must possess a radiant beam large enough to encompass the entire detection chamber, and thus all the chromophores, while providing enough energy for a proficient signal strength. Radiant Energy is inversely related to beam size as described in Section 3.7.3. The laser beam exiting the the output port of the Vibrant takes the form of



an ellipse. Ideally, the beam should be focused into the flow cell as accurately as possible so that the beam profile takes on a circular shape ranging between 1 mm and 2 mm in diameter so as to cleanly enter the 2 mm wall of the flow cell. The setup required that we spatially orient the output beam by a cylindrical lens (LJ1014L2-B, Thorlabs, Newton, NJ) in addition to collimating the beam using two plano-convex lenses, 100 mm and 50 mm focal length (LA1509 and LA1131, Thorlabs, Newton, NJ) before entering the flow cell. The result was a 1 to 2 mm diameter cylindrical spot size measuring between 11.0-12.0 mJ. Spot size was determined by irradiating Zap-It Laser Alignment Paper (Kentek Corp., Pittsfield, NH) with a single 5 ns pulse and measuring the diameter of the burn.

## **3.5 Photoacoustic Mechanism**

### **3.5.1 Excitation**

The photoacoustic mechanism as it pertains to these studies begins with the excitation of a chromophore, in this case melanoma or its related tissue phantom. 5 ns pulsed laser light (usually 450 nm) directed into the flow chamber bombards the chromophore of interest as it passes through the beam path. The chromophore, by definition, absorbs the incident light and photon energy is transformed into thermal energy. The increase in thermal energy causes a temperature rise within the chromophore and a kinetic thermo-elastic expansion ensues.

### **3.5.2 Acoustic Wave Propagation**

The thermo-elastic expansion of the chromophore is transient due to the pulsed nature of the incident laser light (see Chapter 1.1). Since the excitation pulses are short enough in duration that no thermal heat escapes the chromophore, small elastic enlargements of the cells occur within solution in a manner such that pressure waves are propagated away from the source in the range of 1-50 MHz.

### **3.5.3 Acoustic Wave Detection**

Longitudinal pressure waves, such as those emanated from a photoacoustic source, propagate parallel to the direction of the wave. The resulting effect is that of a compression wave or moving band of high pressure. This high pressure band moves freely in solution (such as the environment within the flow chamber) at a speed of 1.5 mm/s away from the source in all directions. Therefore, a portion of those waves inevitably come into contact with the PVDF film, striking it as a mallet would strike the surface of a drum. The PVDF film is a highly ordered copolymer that can be likened to a lipid bilayer in a biological system. At steady state, or ground, conditions are entropically favorable for an ordered copolymer structure. When an acoustic wave strikes a surface of the film, that copolymer layer is disrupted, increasing the entropy of the system and consequently forming a charge on the disrupted surface of the film. The exterior of the film is grounded by a copper plate electrode therefore conferring a positive charge to the interior surface of the PVDF film.

### **3.5.4 Signal Transduction**

The positive voltage produced by the photoacoustic phenomenon is conducted throughout the interior of the detection chamber by a 1.8% saline solution which serves as the solvent for all media of interest. The electrode described in Section 3.3.3 carries the charge out of the flow cell for further analysis. A schematic of this event is shown in Figure 3.5.

## **3.6 Data Acquisition**

### **3.6.1 Amplification and Signal Display**

The transduced voltage of a photoacoustic effect is carried to a SR445A 350 MHz Amplifier (Stanford Research Systems, Sunnyvale, CA) where it is amplified by four stages each providing a gain of 5 for an amplification range of 5 to 125. Voltage signals are displayed by a TDS 2024 200 Mhz Oscilloscope (Tektronix, Beaverton,

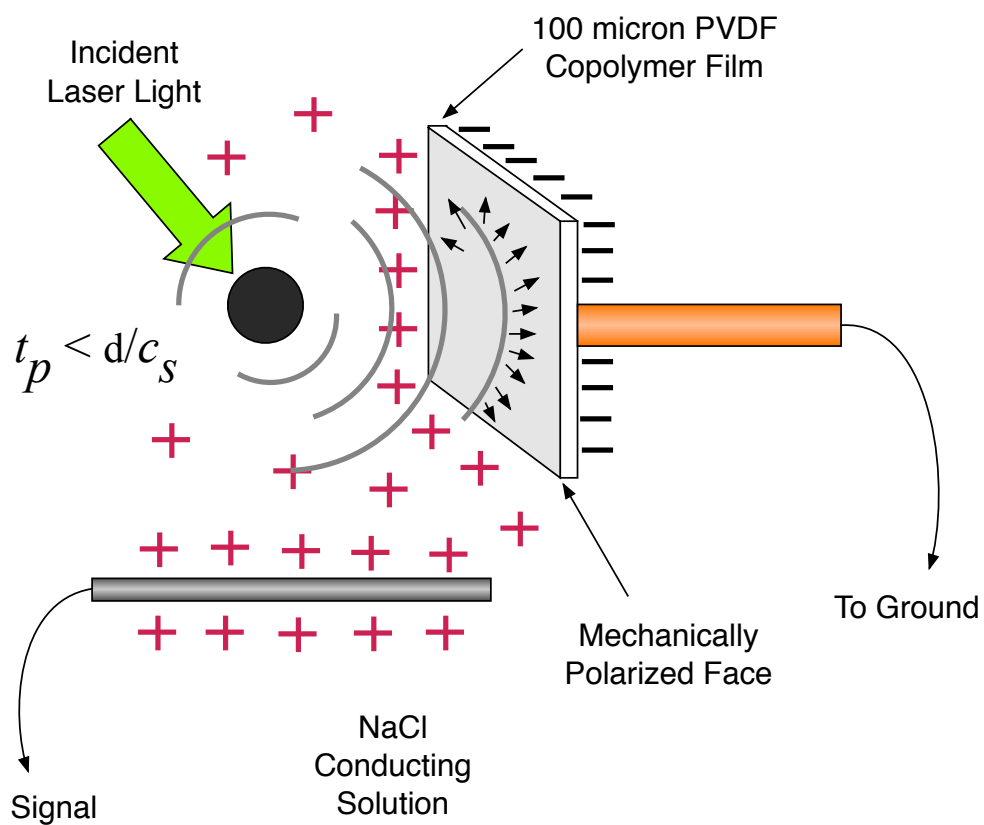


Figure 3.5: Schematic showing the photoacoustic mechanism as it applies to this system. The figure represents the interior of detection chamber. Single chromophore excitation. Equation for pulse time noted.

OR) triggered by a photodiode (Thorlabs, Newton, NJ) upon each laser firing.

## **3.7 System Modifications and Improvements**

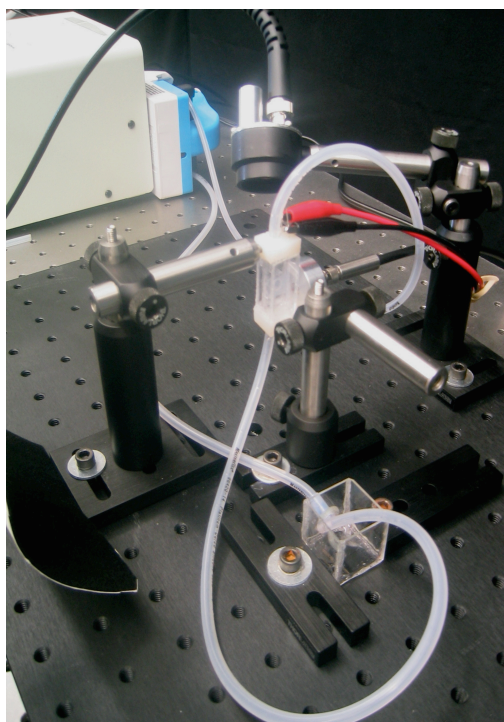
A number of modifications and improvements were made to the overall design of the detection chamber since its inception. Many variations of the current design, previously described, were tried and tested in order to improve signal strength, ease of operation, and detection threshold.

### **3.7.1 Design**

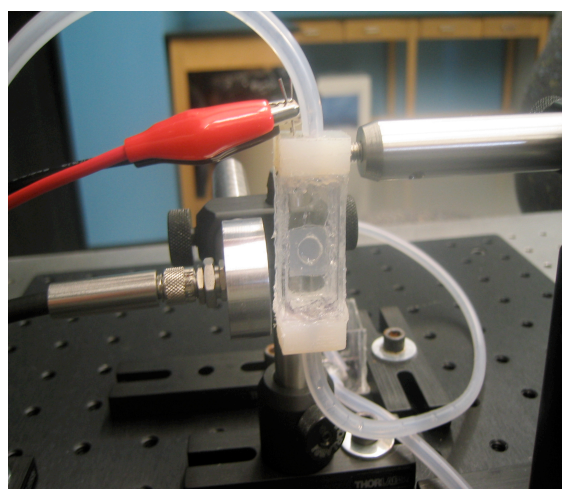
Initially, the cell was designed as a dual chamber device constructed from standard microscope slides (Fisher Scientific, Pittsburgh, PA), cyanoacrylate (Loctite, Avon, OH), 100% silicone sealant (Dow Corning, Baltimore, MD), and Nylon sheet plastic (Small Parts Inc., Miami Lakes, FL). These materials were tediously cut and constructed by hand and often resulted in unreliable results. One chamber served as the flow chamber and conducted a positive signal, similar to the current flow cell. The second chamber was a stagnant reservoir filled with saline solution that was grounded by an electrode inserted into the chamber. Separating the two chambers was a glass divider with a 5 mm diameter hole cut into it. The PVDF film was sealed onto the face of the divider on the grounded side. Consequently, this mechanism functioned in the same manner as the current setup and was used to realize the idea that a proposed photoacoustic device, such as this, could successfully detect low numbers of circulating chromophores. A description of this device is important to mention because it is with this setup that the initial results were achieved. However, this elementary form of the detection system was bulky and relatively inefficient, thereby presenting the need for redesigning the system. The initial setup is presented in Figure 3.6.

### **3.7.2 Detection**

It was soon determined that the initial method of detection, as described in Section 3.7.1, needed revising due to complications regarding leaking of the flow cell and



**A**



**B**

Figure 3.6: A. Original setup for photoacoustic detection system including photo-diode, peristaltic pump, excitation source, electrodes, and reservoir. B. Close-up of dual chamber flow cell with side excitation. Electrodes connect to the top of the flow cell.

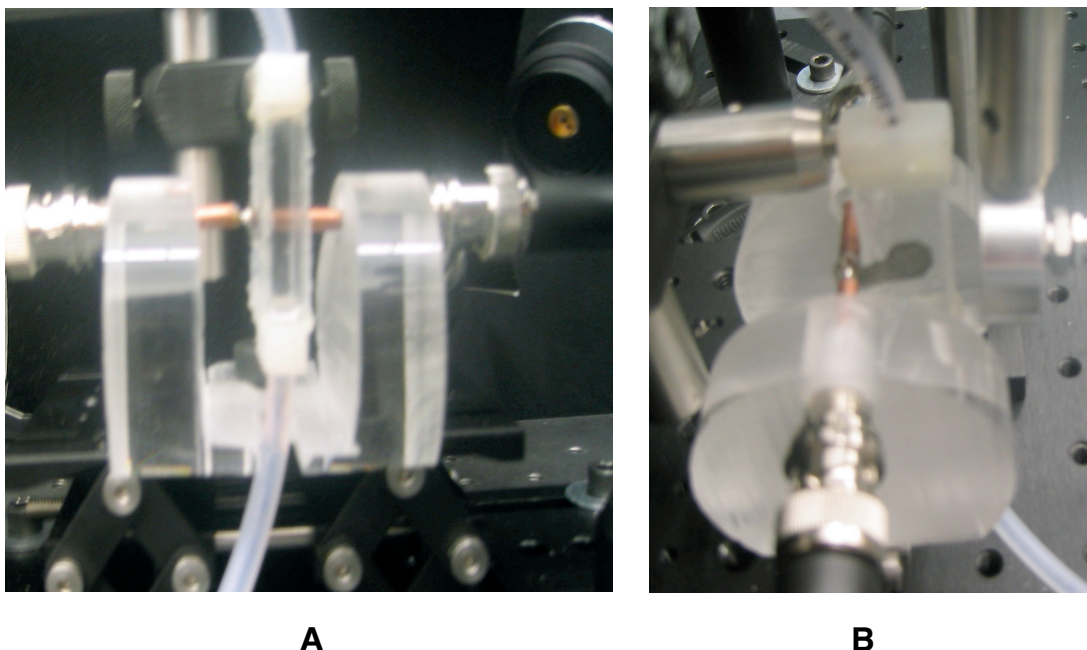


Figure 3.7: A. Side view of single chamber flow cell placed in acrylic electrode housing from direction of laser light input. B. View from top of same setup. Shows dual electrode clamping mechanism on NiCr/Al plated PVDF in free space. Laser ferrule shown on far right.

accessibility of the piezoelectric film for maintenance. Thus, the cell was redesigned to consist of only a single flow chamber with a  $25\text{ }\mu\text{m}$  NiCr/Al plated copolymer PVDF film (Ktech Corp., Albuquerque, NM) affixed to the exterior of the device. This cell was once again constructed by hand and allowed for a portion of the film to extend away from the cell into free space. This version of the device required the use of the cast acrylic housing and external electrodes as described in Section 3.3.3. However, this setup required an additional positive, copper plate electrode housed on the opposite side of ground electrode that clamped both sides of the aluminum plated PVDF film together. This procedure can be seen in Figure 3.7.

Theoretically, the aluminum plating would serve as conductors for both the positive and ground signals, avoiding the use of an invasive electrode into the flow cell which may adversely effect the flow of chromophores. Unfortunately, this method compromised the structural integrity of the PVDF film and resulted in extremely

poor signal strength despite our best efforts. The reasons for the lack of signal strength is yet unknown but assumed to be a result of signal shorting by electrode contact. As a result, the design was once again shifted to reflect the current setup including a 100  $\mu\text{m}$  external non-plated film, internal positive electrode, and direct grounding by an external plated electrode placed directly on the detection area of the PVDF film.

### 3.7.3 Signal Improvement

The experimental goal of this project has primarily been to increase signal strength while maintaining a high signal to noise ratio. Many of the slight modifications necessary to achieve this goal have occurred through undocumented trial and error over the course of working with the device.

The first large improvement in signal strength was due to an increase in detection aperture size from around 2 mm to 5 mm in diameter. Intuitively, the larger the detection aperture the greater the likely-hood that acoustic wave collection will occur from the surrounding medium. Secondly, the introduction of the customized flow cell greatly increased overall signal strength primarily due to the smaller volume of the cell, particularly in regards to the 2 mm side width. This 2 mm width constrains the chromophores passing through the flow cell and forces the entire medium to pass through the excitation beam path assuring that no chromophore passing through the cell is missed. The customized flow cell is also placed on an x-z translational stage that allows for accurate placement of the flow cell in reference to the set beam path.

Another form of signal improvement involves focusing and applying the laser to the detection chamber, the methodology for which has taken on a number of forms. Initially, we ran tests using a protocol termed *front excitation* which involved excitation of the specimen through the front, or large surface of the flow cell (i.e. the surface containing the PVDF film). This meant that the beam path crossed the plane of the copolymer film after it had passed through the cell. This proved to be inefficient due to an increase in noise caused by a pyro-electric effect of light photons

interacting with the polymers of the film. Subsequently, *side excitation* became the preferred method of stimulation.

Initially the laser light was coupled into a fiber, as described in Section 3.4.2, in order to maneuver the light source to the most efficient location for excitation. Trial runs were conducted using light emitted directly from the fiber resulting in a spot size of nearly 4 mm. It was quickly determined that the focus of the laser light was infinitely important and directly related to signal strength. Once again this is an intuitive thought. Radiant exposure is defined as Joules per  $\text{cm}^2$ , a small decrease in spot size diameter results in an increase in radiant exposure by the inverse square law. As it pertains to the design of this project, a millimeter decrease in spot size from 3 mm to 2 mm for a 12 mJ light source results in a 125% increase in radiant exposure. As a result, a 35 mm plano-convex lens (LA1027, Thorlabs, Newton, NJ) was inserted between the fiber and the detection chamber to decrease the incident spot size to approximately 2 mm in diameter. Eventually, the entire setup was repositioned for excitation without an intermediate fiber, as described in Section 3.4.3, which increased incident energy from 7.0 or 8.0 mJ to 11.0 or 12.0 mJ. The spot size was brought to within  $0.026 \text{ cm}^3$  (between 1 and 2 mm in diameter) giving a radiant exposure in the range of 460-900  $\text{mJ}/\text{cm}^2$  and increasing signal voltages to their highest level to date.

The amplification of the signal as it passes from the detection apparatus to the oscilloscope plays an important role in the identification of a signal as well as noise response. It was found through trial and error that a gain of 25 appeared to produce the best signal differentiation. A gain of 125 often dropped the signal to noise ratio dramatically and produced poor results, although it should be noted that in some instances a gain of 125 was preferable for the detection of extremely weak signals. Therefore, a gain of 25 is used as a default, however, the gain should be set on the basis of the individual experiment and may vary throughout the results of this work.



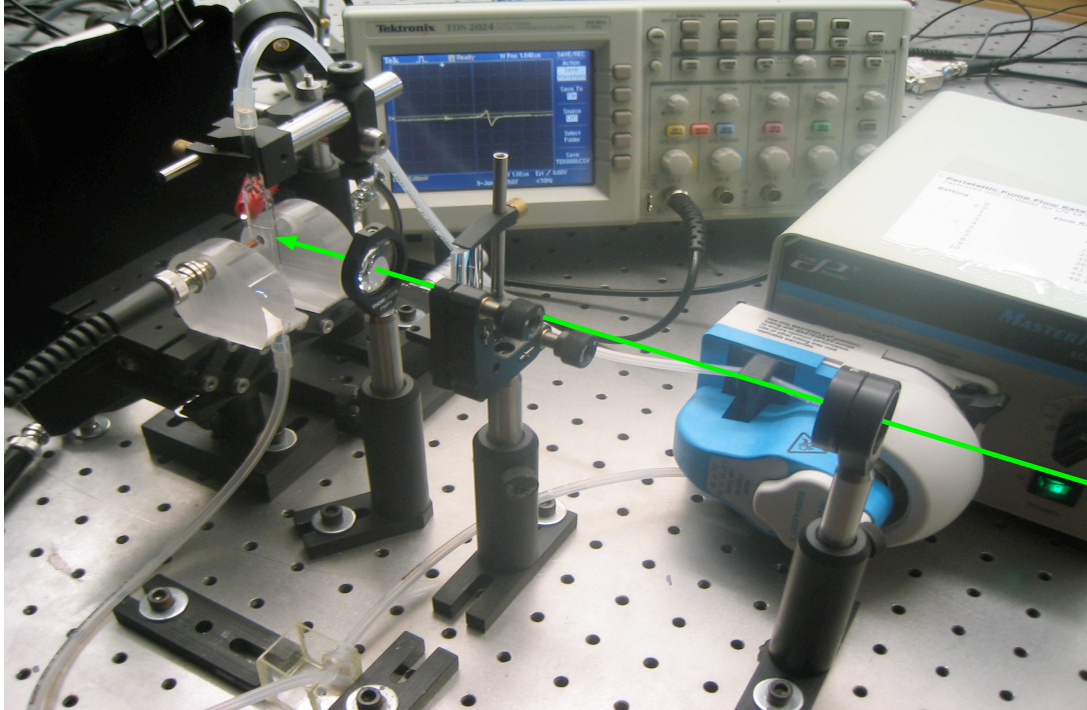


Figure 3.8: Picture of current setup with beam path from laser.

### 3.8 Final Setup Design

Based upon the factors set forth in this chapter, a working model has been developed that as of July 2006 is the most efficient design for the photoacoustic detection of circulating melanoma cells. A picture of the active setup is shown in Figure 3.8 followed by a diagram of the most current design setup in Figure 3.9.

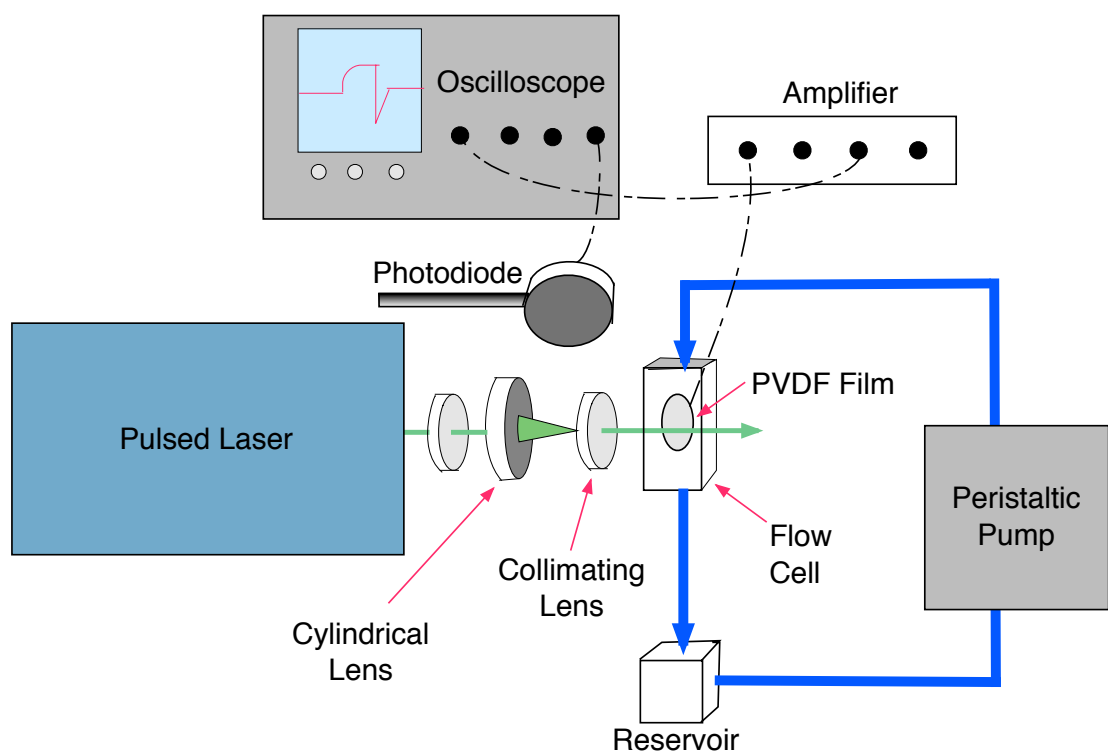


Figure 3.9: Schematic representing the entire photoacoustic system.

# Chapter 4

## Detection Trials Incorporating Latex Microspheres

### 4.1 Introduction

The first detection trials to be run following the construction of the photoacoustic device incorporated latex microspheres as a precursor to live melanoma cells. These trials were conducted as a proof of principle for the device. The test solutions were also used to determine a detection threshold for the device in order to characterize the sensitivity of the system. Proof of principle was conducted using the original dual chamber design while initial thresholding was performed after implementing a single chamber design for the flow cell. As discussed in the previous chapter, technical problems required a re-design of the detection chamber resulting in progressive improvements to the system. This chapter presents proof of principle for the device as well as describing the thresholding for both the single chamber and current setup. It describes in detail the methodology for these types of experiments and includes a discussion of results and system parameters based on experimental results.

### 4.2 Latex Microspheres

#### 4.2.1 Specifications

Black CML Latex Microspheres (2-BK-7000, Interfacial Dynamics Corp., Portland, Oregon) measuring  $6.6\ \mu\text{m}$  in diameter were used as tissue phantoms to mimic

the photoacoustic response of melanoma cells (optical properties of melanoma cells and tissue phantoms are discussed in Chapter 8.0). The latex microspheres were chosen because of their broadband absorption spectrum and relative size. A standard melanoma cell can range between 10  $\mu\text{m}$  to greater than 50  $\mu\text{m}$  depending upon the heterogeneity of the cell line and morphology of the cell [26]. Although the melanoma cell tends to be much larger than the microspheres used in these trials, the microspheres contain a darker pigment and therefore sufficiently imitate the photoacoustic effect of a melanoma cell, as discussed in later chapters. However, it is speculated that the larger size of the melanoma cells and the large number of melanin granules contained within them will allow them to produce a stronger photoacoustic signal than the microspheres per single cell. Therefore, it is hypothesized that true melanoma will provide a signal similar to that of the microspheres, if not greater.

### 4.2.2 Spectroscopy

Spectroscopic analysis of the latex microspheres was conducted using a HR-2000 High-Resolution Spectrometer and a HL-2000 Halogen Light source (Ocean Optics Inc., Dunedin, FL). An absorption spectrum of 4.3 g/100ml (4.3%) black microspheres was taken using a 150  $\mu\text{m}$  cuvette constructed of 1mm thick glass slides (Fisher Scientific, Pittsburgh, PA) and 150  $\mu\text{m}$  shim stock (Artus Corp., Englewood, NJ). The microsphere solution was placed within the constructed cuvette and inserted between the halogen light source and detector of the spectrometer. Data was analyzed using OOIBase32 (Ocean Optics Inc., Dunedin, FL). Data collection was taken under an integration time of 14 ms with no averaging. A short path length was used to reduce the effects of scattering on the absorbance data. The results are displayed in Figure 4.1.

It can be inferred from the absorption spectrum that the microspheres possess steady absorption across the entire visible spectrum showing that the spheres are indeed a black broadband absorber. This spectrum indicates a slight increase in absorbency with wavelength within the visible range.

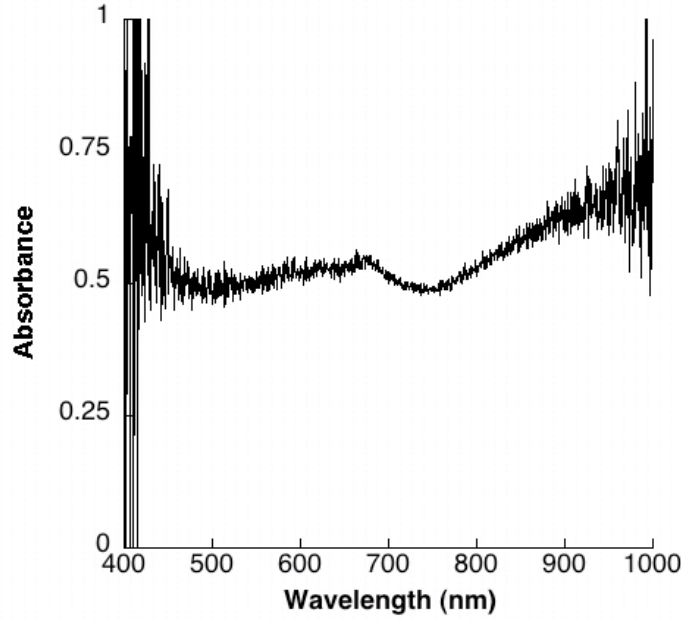


Figure 4.1: Absorbance spectrum for 6.6  $\mu\text{m}$  black CML Latex Microspheres suspended in a 0.9% solution across a 150  $\mu\text{m}$  plane.

## 4.3 Materials and Methods

### 4.3.1 Saline Solutions

The latex microspheres were introduced into a signal conducting saline solution before being entered into the detection system. Initially, the saline solution was a 0.9% sodium chloride (NaCl) solution created by adding 0.9 g of solid NaCl solute into 100 ml of de-ionized water solvent. Currently, a 1.8% solution is used, the reasoning for which is described in Section 4.7.1.

Microspheres were added to 20 ml of saline solution in varying concentrations ranging from a maximum of  $7.124 \times 10^6$  microspheres/ml to a minimum of  $7.0 \times 10^2$  microspheres/ml. The microsphere concentration of each solution was deduced by Equation 4.1

$$\text{microsphere/ml} = \left( \frac{V_s}{V_m} / V_{su} \right) (V_i) / (20\text{ml}) \quad (4.1)$$

where  $V_s$  stands for solid volume of microspheres from factory,  $V_m$  stands for volume

of a single 6.6  $\mu\text{m}$  microsphere,  $V_{su}$  represents the remaining volume of factory microsphere suspension, and  $V_i$  represents volume incorporated into saline solution.

15 ml of each selected concentration was placed into the reservoir for circulation through the detection system.

## 4.4 Initial Results

This section will include data taken as proof of principle for the detection system as well as thresholding data for the original version of the single chamber flow cell built by hand. It will also give photoacoustic results for multiple wavelength excitation.

### 4.4.1 Photoacoustic Waveform

Figure 4.2 shows a standard photoacoustic waveform derived from a high concentration tissue phantom solution. This waveform is taken from a set of data displayed in Section 4.4.2 as proof of principle for the original dual chamber detection system. This trial employed a 0.9% saline solution, 510 nm excitation, 7.5 mJ input energy, and a 2.36 mm x 2.45 mm spot size resulting in a radiant exposure of 0.129 J/cm<sup>2</sup>. The signal was averaged over 64 acquisitions. The photoacoustic peak occurs at 3.0  $\mu\text{s}$  followed by secondary reflective signals. The large signal noise ranging from 0  $\mu\text{s}$  reaching up to 2  $\mu\text{s}$  is from the firing of the laser.

### 4.4.2 Dual Chamber Flow Cell

Results from the pilot study of the dual chamber flow cell are given in Figure 4.3. These trials employed 0.9% saline solutions, 510 nm excitation, 7.5 mJ input energy, and a 2.36 mm x 2.45 mm spot size resulting in a radiant exposure of 0.129 J/cm<sup>2</sup>. The signals were averaged over 64 acquisitions with no amplification. As can be seen from the results, a strong signal was produced at 3.0  $\mu\text{s}$  ranging between 5 and 10 mV thus proving the success of the device. The control signal contained a variegated sine wave not typical of other trials, which may have affected the other resulting signals. To account for the control signal variation the results were normalized over the control signal. The results of which are shown in Figure 4.4.

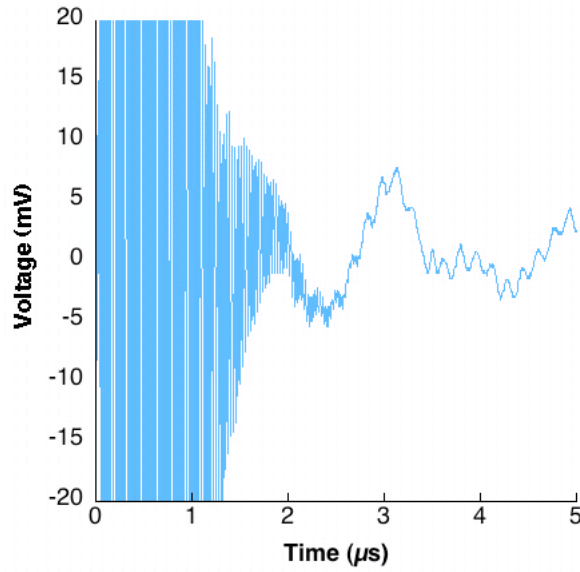


Figure 4.2: Standard photoacoustic waveform retrieved from pilot study of system.  $1.42 \times 10^6$   $\mu\text{sphere/ml}$  solution. 510 nm excitation with no amplification.

The resulting peak voltages were plotted against concentration of microspheres in solution to show signal strength in relation to chromophore concentration. Peak voltage was averaged over 12 peak data points with control included. This is represented in Figure 4.5.

#### 4.4.3 Single Chamber Flow Cell

The control signal for the pilot study and dual chamber flow cell raised a large amount of concern as to the reliability of the system and the subsequent photoacoustic signals as described in the previous section. The variegated sine wave produced by all the samples, including the control, resulted in the redesigning of the system for use with a single chamber flow cell, primarily focusing on an alternative means of grounding the piezoelectric film, as described in Section 3.7.2. A more detailed set of experiments, similar to the microsphere concentration variation of the pilot study, were conducted to determine the sensitivity of the new design. These trials were conducted with a much greater thoroughness in the hopes of obtaining an accurate

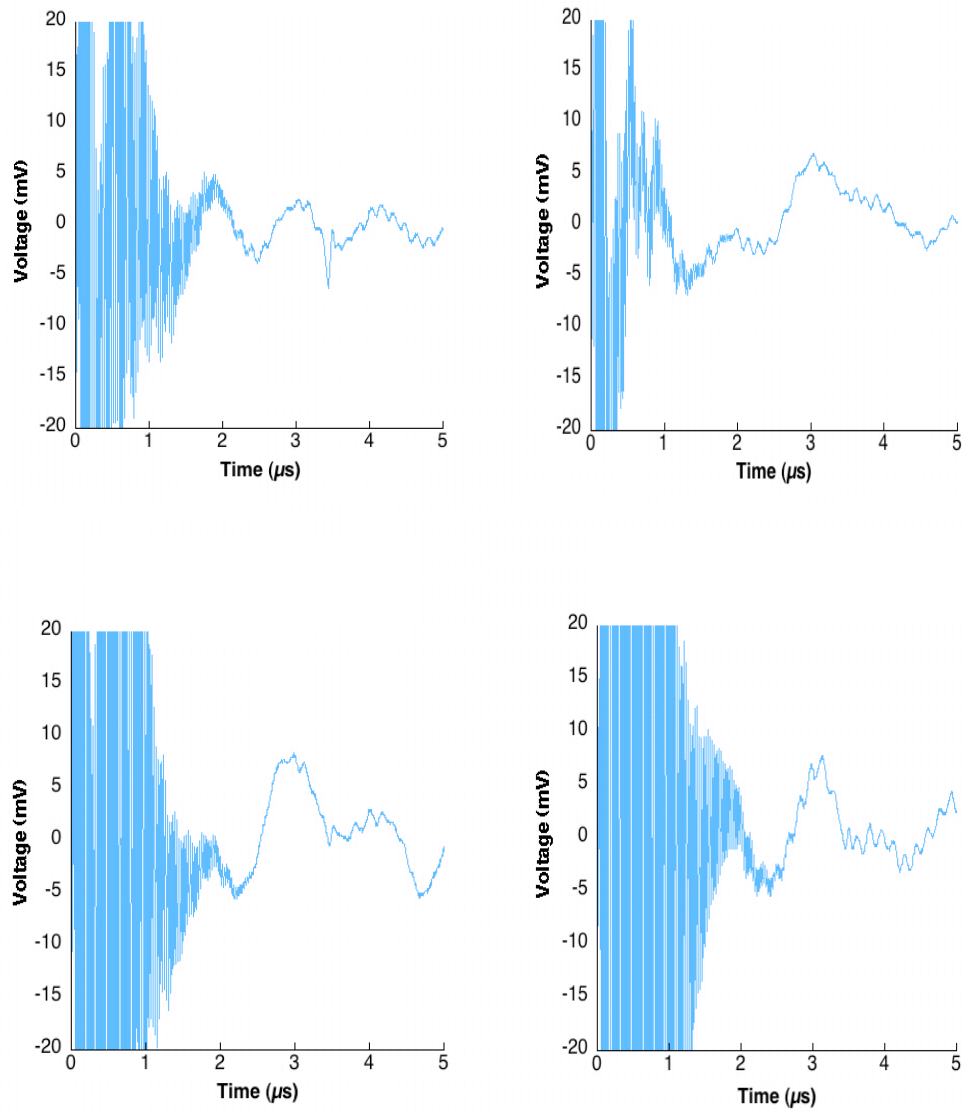


Figure 4.3: Pilot study results including control and three decreasing concentrations from top right to bottom right. 510 nm excitation with no amplification. Top left: 0.9% saline control solution. Top right:  $7.12 \times 10^6$   $\mu$ sphere/ml solution. Bottom left:  $3.56 \times 10^6$   $\mu$ sphere/ml solution. Bottom right:  $1.42 \times 10^6$   $\mu$ sphere/ml solution.



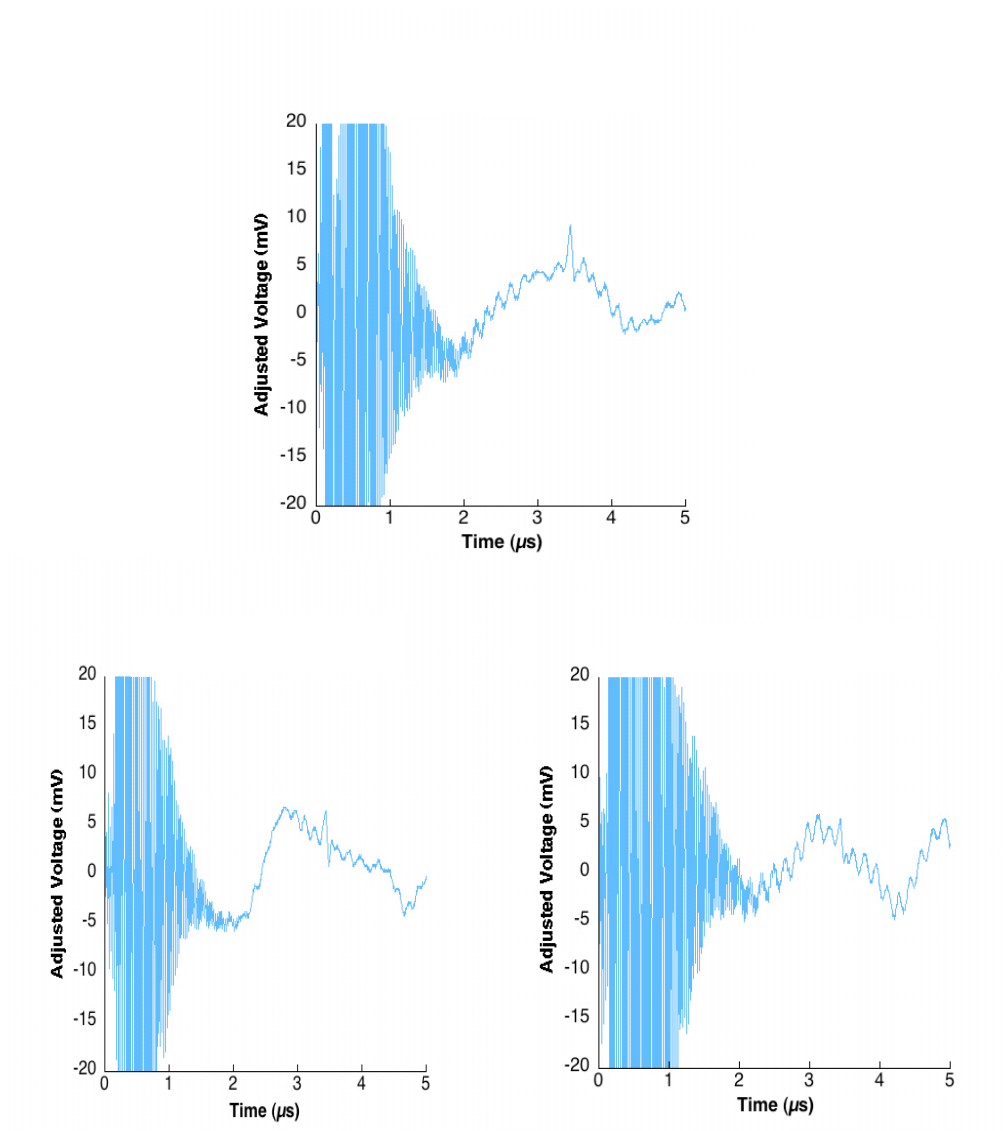


Figure 4.4: Pilot study photoacoustic signals normalized over control waveform. 510 nm excitation with no amplification. Top:  $7.12 \times 10^6$   $\mu$ sphere/ml solution. Bottom left:  $3.56 \times 10^6$   $\mu$ sphere/ml solution. Bottom right:  $1.42 \times 10^6$   $\mu$ sphere/ml solution.

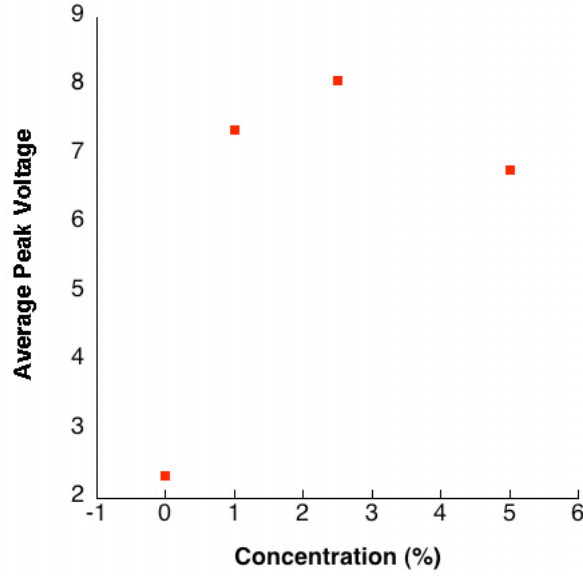


Figure 4.5: Average peak voltage given by percentage of microspheres to saline in solution for the dual chamber trials. Control included.

minimum detection threshold value for the system. Twelve sample concentrations ranging from  $7.12 \times 10^6$  to  $7.0 \times 10^2$   $\mu$ spheres/ml were used to gain an understanding of signal variation with concentration. Determining this would make it possible to quantify unknown concentrations of tissue phantoms by known signal intensities. All trials were run with the following experimental parameters: 450 nm excitation, 8.75 mJ energy input, 1 x 1 mm spot size, 13.1 mm beam length, radiant exposure of  $0.875 \text{ J/cm}^2$ , and 9 ml/min flow rate. Samples  $7.12 \times 10^6$  through  $8.9 \times 10^4$  employed a signal gain of 25 averaged over 64 acquisitions. Lower concentrations ranging from  $5.5 \times 10^3$  through  $7.0 \times 10^2$  used a signal gain of 125 averaged over 128 data acquisitions. The differing parameters were necessary to differentiate signals of lower concentrations for this setup. Figure 4.6 shows the largest peak signal obtained from these trials. Also shown is the control waveform with a similar gain of 25.

Figure 4.7 displays the smallest differentiated photoacoustic signal for these trials. The control waveform for a gain of 125 averaged over 128 is shown for com-

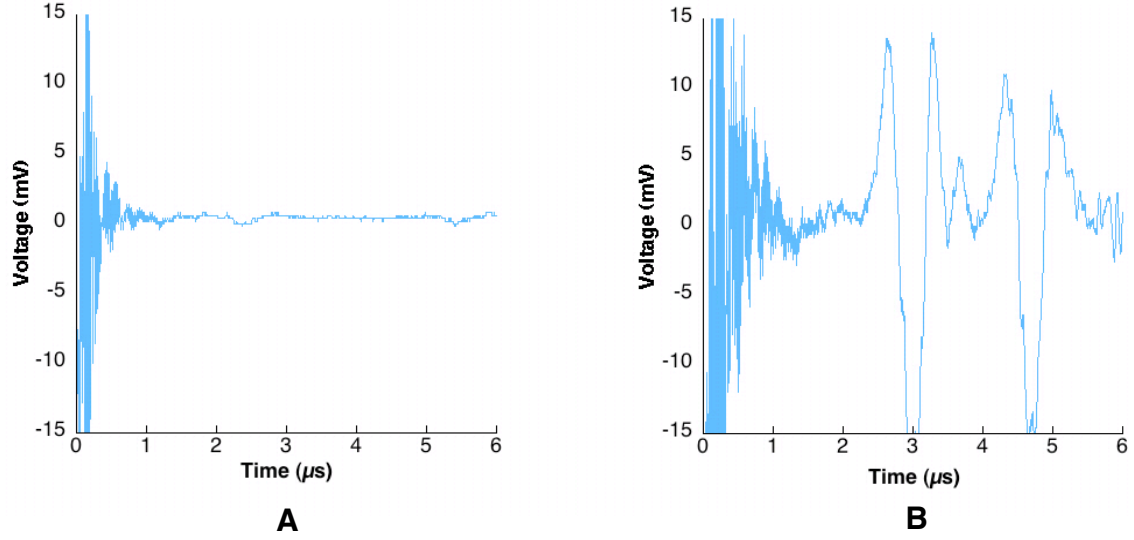


Figure 4.6: Strongest signal obtained from the single chamber detection trials (20:0.2 saline to microsphere solution ratio). 450 nm excitation with a gain of 25. A. 0.9% saline control waveform. B.  $1.42 \times 10^6$   $\mu$ sphere/ml solution.

parison. All representative waveforms collected from these trials can be found in Appendix A.

#### 4.4.4 Thresholding

Peak voltages were analyzed for each waveform. A signal to noise ratio was determined for each peak value by dividing the peak values by a standard deviation measurement taken from the control waveforms. This was done for both amplifications of 25 and 125. This eliminated any signal due to noise within the system. The standard deviation for a gain of 25 was 0.089 mV. The standard deviation for a gain of 125 was 0.462 mV. Figure 4.8 displays the calculated signal to noise ratios for each photoacoustic signal as a function of microsphere concentration. Both signal gains are represented as well as the corresponding linear equations.

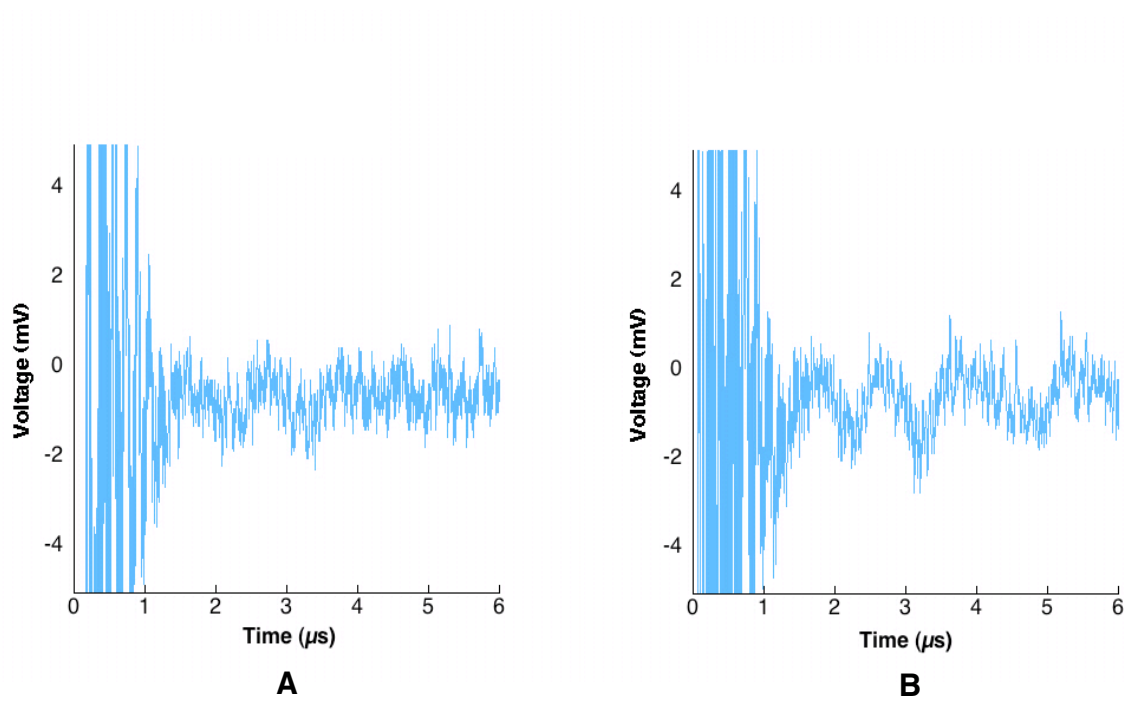


Figure 4.7: Smallest differentiated signal obtained from the single chamber detection trials (20:0.0001 saline to microsphere solution ratio). 450 nm excitation with a gain of 125. A. 0.9% saline control waveform. B.  $7.0 \times 10^2$  μsphere/ml solution.

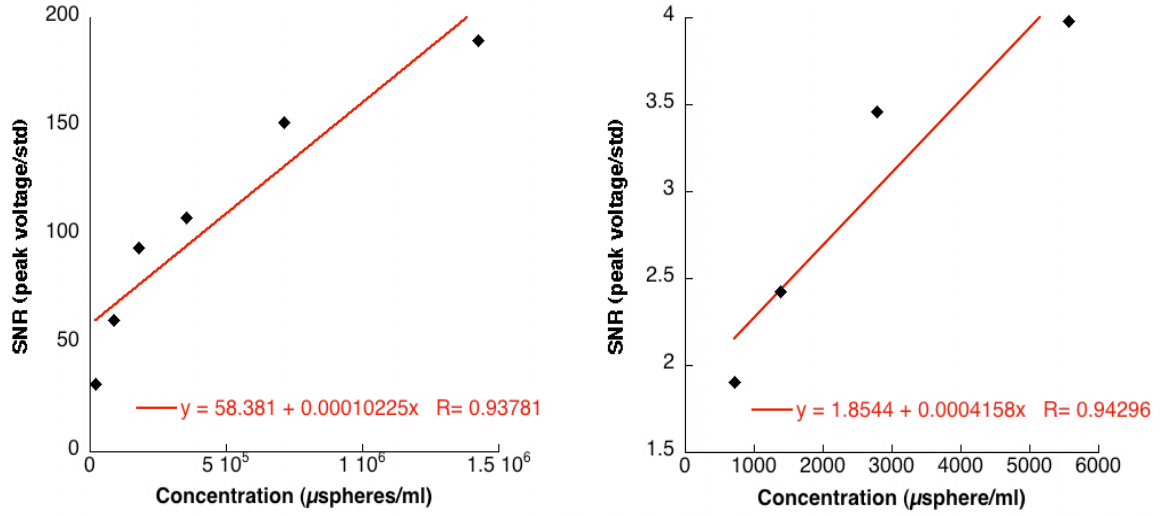


Figure 4.8: Signal to noise ratios for peak values of detection trials using single chamber flow cell as a function of concentration. Gain of 25 shown on left. Gain of 125 shown on right. Linear function of curve fit given in red.

## 4.5 Discussion of Initial Results

### 4.5.1 Pilot Study

The results of the pilot experiment showed that photoacoustic detection of circulating cells is plausible. Latex microspheres,  $6.6 \mu\text{m}$  in diameter, were successfully detected at 3 concentrations on the order of  $10^6$  per milliliter. The detection mechanism proved sufficient for the purposes of this experiment.

The noise produced by the laser can be identified as the large clustered excitation ranging from 0-2  $\mu\text{s}$  on each set of data. It can be noted from graphical analysis of the control solution that the voltage change associated with the saline solution produces an oscillating sinusoidal curve in the absence of any latex microspheres (Figure 4.3). The oscillation could be an acoustic resonance created within the solution or surrounding materials but is most likely attributed to insufficient grounding. This is assumed due to the fact that the oscillation is eliminated by a redesign of the system, particularly the ground component. Excitation of the microspheres by the

laser light is clearly shown in each one of the solutions tested. The control oscillation remains visible beneath the excitation peak, however, it does not appear to affect the desired measurements as is shown by the normalized waveforms.

A marginal decrease in signal was noted between the 2.5% solution and the 1% solution (Figure 4.5). A discrepancy occurred, however, with the 5% microsphere solution which should have had a peak voltage greater than that of the 2.5% and 1% solutions. This can be attributed to an experimental inconsistency. In this trial, the 5% solution used was created previous to the time of execution. The solution was stored in a chilled environment and may not have thoroughly acclimated to the temperature of the other solutions as well as possibly containing a slightly skewed consistency, thus accounting for the counter-intuitive results.

### **4.5.2 Time Domain Response**

Peak excitation consistently occurs at  $3.0\ \mu\text{s}$  (Figure 4.4). This is to be expected considering that in this design the detector is a distance of 4.0 mm from the acoustic origin as depicted in Figure 4.9. Acoustic waves travel through liquid at a rate of approximately  $1.5\ \text{mm}/\mu\text{s}$ . Therefore, acoustic signals can travel a distance of 4.5 mm in  $3\ \mu\text{s}$  in solution. Assuming light propagation time to be insignificant on the  $\mu\text{s}$  scale, excitation would occur simultaneously throughout the beam path beginning at time  $0\ \mu\text{s}$  (firing of the laser). Therefore, one can assume that the first signal to reach the detector will be the excited chromophore closest to the detector, in this case directly perpendicular to the detector as shown in Figure 4.9. This distance totals 4.0 mm which correlates to slightly less than  $3\ \mu\text{s}$  travel time for an acoustic signal which is reflected in the results as the appropriate time domain response for this system. This data reinforces the fact that the excitation peak is indeed that of the circulating microspheres.

### **4.5.3 Single Chamber Sensitivity**

Initial synopsis of the single chamber design yields more reliable and more efficient results. The control signal of a plain 0.9% saline solution for both a gain of 25

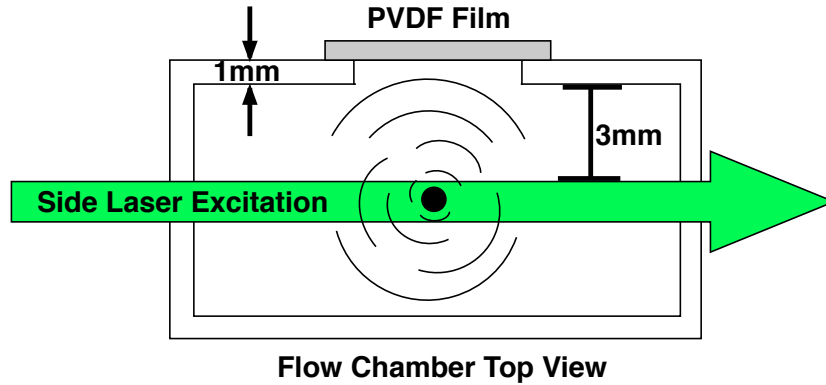


Figure 4.9: Dimensions of dual chamber flow cell that result in a photoacoustic response at  $3.0 \mu\text{s}$ . Includes single chromophore excitation. Second chamber not shown.

and a gain of 125 show a relatively steady response with no identifiable signals alluding to a photoacoustic response (Figures 4.6 and 4.7). The standard deviation of the control waveform is  $0.089 \text{ mV}$  as compared to  $1.91 \text{ mV}$  of the former dual chamber design. This result is clear evidence of a more reliable design with less signal variation including no phantom signals or oscillations. This is most likely attributed to a stronger grounding mechanism and elimination of any osmosis behavior between solutions of the previous design. The control signal with a gain of 125 shows evidence of a small sinusoidal wave with a standard deviation of  $0.462 \text{ mV}$ . This deviation is greater than that of the gain of 25 control which would be expected with a higher amplification, however, it is still much less than the previous design.

The maximum signal produced by these trials (Figure 4.6) is that of a  $1.42 \times 10^6$  microsphere/ml solution. The signal had a peak voltage of  $16.8 \text{ mV}$  with a gain of 25. One should note the strong peaks that occur at  $3.2$ ,  $4.2$ , and  $5.0 \mu\text{s}$  which can be attributed to acoustic reflectance and secondary signals made possible by the small enclosed area of the detection chamber. The smallest differentiable solution is  $7.0 \times 10^2$  (Figure 4.7) with a peak value of  $0.88 \text{ mV}$  at a 125 gain. This signal appears to be barely differentiable from the control signal, however, upon calculation the signal nearly doubles that of the control giving a signal to noise ratio of 1.903.

This proves to be a strong detection of a 700 microsphere per milliliter solution.

The time domain for the photoacoustic signal is different in the single chamber detection trials as compared to the dual chamber detection trials. The single chamber detection trials show a detection peak at a slightly shorter time of  $2.5 \mu\text{s}$ . This is due to the fact that the newly built detection chamber has an excitation width of 3.5 mm, from excitation point to PVDF film, as compared to 4 mm in the previous results (refer to Figure 4.9). This distance correlates to an acoustic travel time of  $2.33 \mu\text{s}$  which is near the actual response time of the waveforms. Amplification of 125 seems to form a small sinusoidal wave as seen in the control in Figure 4.7 which appears in all of the subsequent waveforms (see Appendix A). The photoacoustic detection peak is still thought to primarily occur at  $2.5 \mu\text{s}$ , however, similar peaks appear both before and after that characteristic peak. This is thought to be an artifact of the 'natural' sinusoidal waveform only amplified by the presence of a microsphere solution. The reason for this remains unknown. This characteristic response is what should be looked for when attempting to deduce the presence of cells in solution.

The analysis of signal to noise ratio vs. concentration given in Figure 4.8 illustrates the linearity of signal response to decreasing concentrations of absorbers. Each data point is one half the concentration of the previous, larger point resulting in a linear decrease in signal strength. The theoretical slope of signals with a gain of 25 is  $1.33 \times 10^{-4}$  which differs by only 23.3% from the experimental slope of  $1.02 \times 10^{-4}$ . This is a relatively small deviation considering the experimental conditions. The theoretical slope of signals with a gain of 125 is  $6.66 \times 10^{-4}$  which differs by only 37.6% from the experimental slope of  $4.1 \times 10^{-4}$ . The linearity of the samples differs with varying amplification as expected due to experimental conditions. The important point is that the trials are nearly linear which allows for quantification of unknown solutions by signal interpolation. For solutions monitored with a gain of 25, a voltage change of 1 mV will require the addition or removal of 9,779 microspheres/ml while the addition of a single microsphere will result in a voltage increase of merely  $1.02 \times 10^{-4}$  mV. For solutions monitored with a gain of 125, a



voltage change of 1 mV will require the addition or removal of 2,405 microspheres/ml while the addition of a single microsphere will result in a voltage increase of merely  $4.15 \times 10^{-4}$  mV. If the slightest measurable voltage change can be approximated as 0.1 mV, realistically, for a gain of 25 the sensitivity of the single chamber device is about 978 microspheres while at a gain of 125 the sensitivity would be approximately 240 microspheres.

This data can be further analyzed to obtain a more relevant meaning than previously discussed. Assuming even distribution of microspheres within the entire solution, the exact amount of single microspheres crossing the beam path at any given time can be deduced by Equation 4.2.

$$M_{\#} = (C_m)(V_b) \quad (4.2)$$

Where  $M_{\#}$  is the number of excited microspheres,  $C_m$  is concentration of microspheres per milliliter solution, and  $V_b$  is the volume of the excitation beam path through the flow cell in  $\text{cm}^3$ . This deduction makes it possible to realize the number of single cells producing each photoacoustic signal, therefore interpolating the number of single chromophores necessary to induce a differentiated signal. In the case of the single chamber detection trials, **only 9 individual microspheres are crossing the plane of the excitatory path**, producing photoacoustic signals, with the least concentrated solution. Plus, it can be inferred that fewer than 9 microspheres are crossing the beam path because of sample loss associated with the pump tubing, reservoir, and uneven distribution of sample.

## 4.6 Redesign and Confirmation of Results

The single chamber flow cell design proved to be the most efficient design to this point. However, it was apparent that the hand crafted flow cells were structurally unreliable and continued to pose problems of leaking or breaking entirely. It was also assumed that a more reliable flow cell with a smaller detection aperture (a size unachievable with the tools in the lab) would allow for more consistent results while alleviating the maintenance problems associated with the hand constructed

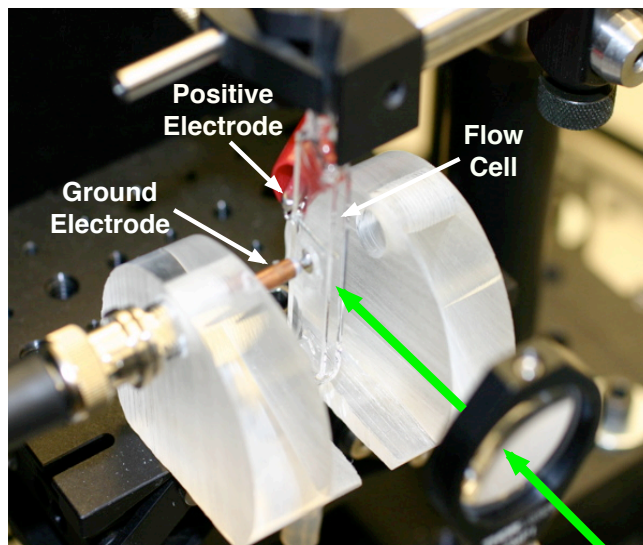


Figure 4.10: Close up of an active Spectrocell customized flow in the detection system. Top of the figure shows the x-z mount for aligning the flow cell. Ground electrode present on PVDF film. Positive electrode in solution. Incident laser light shown.

flow cells. Therefore, a customized flow cell was ordered and implemented into the system (see Section 3.3.1). Figure 4.10 shows the redesigned customized flow cell implemented into the system.

#### 4.6.1 Saline Solutions

During the trials using the customized flow cell it was proposed that a more concentrated saline solution be used to boost signal strength by increasing conductivity throughout the test solution while decreasing resistance from water. Previously, a physiological saline solution of 0.9% had been used as a solvent for all trials. A simple study was conducted that doubled the saline concentration to 1.8%, the results of which are shown in Figure 4.11. The slight increase in signal strength led to the use of 1.8% saline solutions for the duration of these trials and the melanoma trials described in chapter 6.

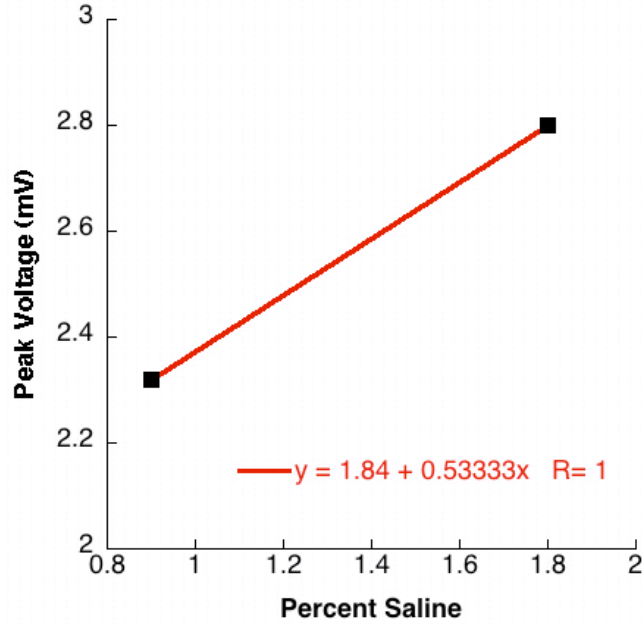


Figure 4.11: The effect of saline concentration on peak voltage.

#### 4.6.2 Photoacoustic Waveforms

Detection trials similar to those in Section 4.4.3 were conducted to determine the sensitivity and threshold of the newly redesigned system. In these trials seven microsphere solutions of different concentrations ranging from  $8.9 \times 10^4$   $\mu\text{sphere/ml}$  to  $7.0 \times 10^2$   $\mu\text{sphere/ml}$  were passed through the new system. Trials were run with the following parameters: 450 nm excitation, x25 amplification, averaged over 128 data acquisitions, flow rate of 9 ml/min, laser energy input 11.5-12.0 mJ, spot size of  $0.13 \times 0.2$  cm ( $0.026 \text{ cm}^2$ ), and a radiant exposure of  $0.461 \text{ mJ/cm}^2$ .

The largest signal from these trials was that of the  $8.9 \times 10^4$  (1600:1 saline to microsphere ratio)  $\mu\text{sphere/ml}$  solution shown in Figure 4.12. The lowest discriminated signal was that of the  $7.0 \times 10^2$  (200000:1 saline to microsphere ratio)  $\mu\text{sphere/ml}$  solution shown in Figure 4.13. After all trials were run, a post-experimental control was taken which is also displayed in Figure 4.13. As you can see from the graph, a small but clearly differentiated signal exists at  $3 \mu\text{s}$  from this concentration. A

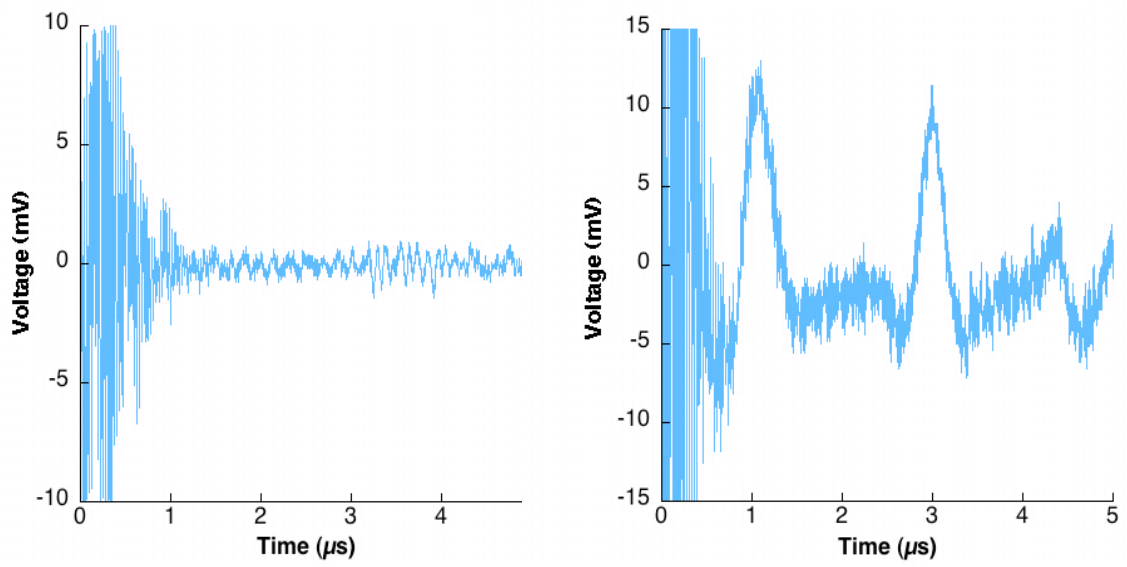


Figure 4.12: Strongest signal obtained from the custom flow cell detection trials (1600:1 saline to microsphere solution ratio) shown on right. Corresponding 1.8% saline control waveform given on left. 450 nm excitation with a gain of 25. 11.5 mJ incident energy.

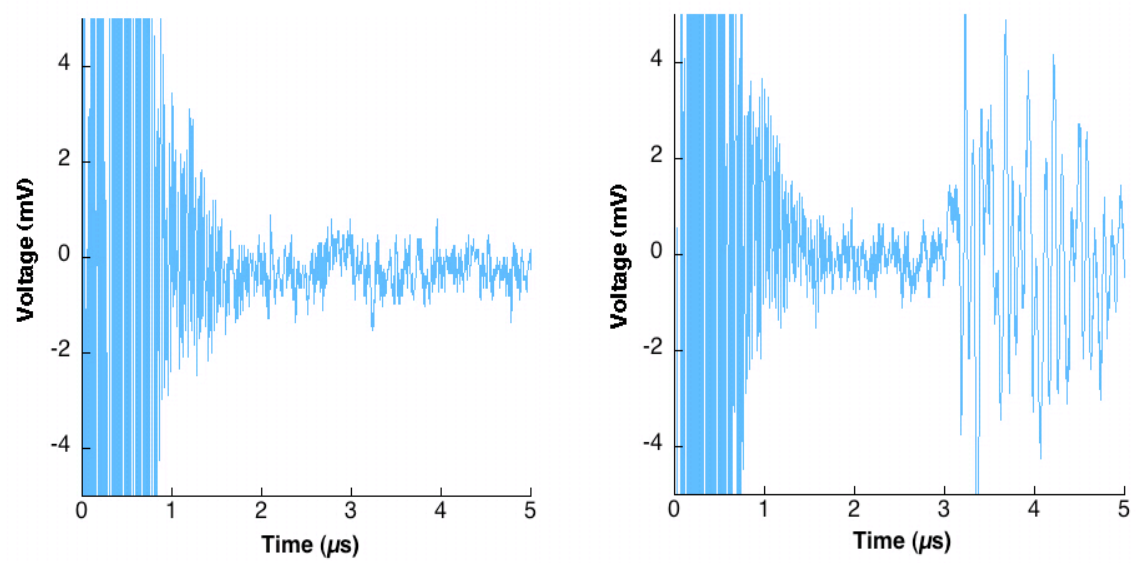


Figure 4.13: Weakest differentiated signal obtained from the custom flow cell detection trials (200000:1 saline to microsphere solution ratio) shown on right. Post-experimental 1.8% saline control waveform given on left. 450 nm excitation with a gain of 25. 11.5 mJ incident energy.

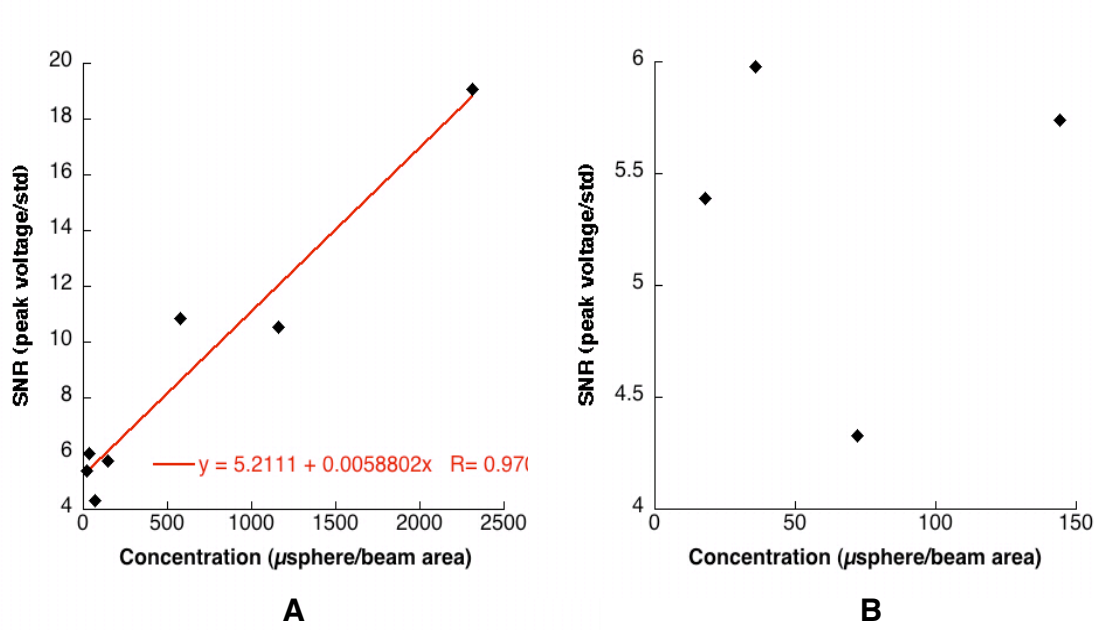


Figure 4.14: A. Signal to noise ratio for all data points taken in customized flow cell trials at  $1.0 \mu\text{s}$ . Linear equation given in red. B. Close up of four smallest concentrations in A.

similar signal also appears in the post-experimental control waveform but weaker. All waveforms for the customized flow cell detection trials can be found in Appendix B.

### 4.6.3 Thresholding

Signal to noise ratios for all waveforms were calculated by normalizing peak voltages over the standard deviation of the pre-experimental control waveform measured from  $0.8$  to  $2.0 \mu\text{s}$ . The standard deviation was  $0.682 \text{ mV}$ . The SNRs were plotted against the concentration of microspheres per illuminated beam path or, in other words, the number of excited microspheres at any given time in solution. All points are plotted with a linear curve fit in Figure 4.14A. Upon analysis of the data, it was found that the SNRs were linear up to the four lowest concentrations. On closer inspection, a data plot (Figure 4.14B) revealed a stochastic behavior for these particular data points. This prompted a secondary data analysis of the photoacoustic reflection

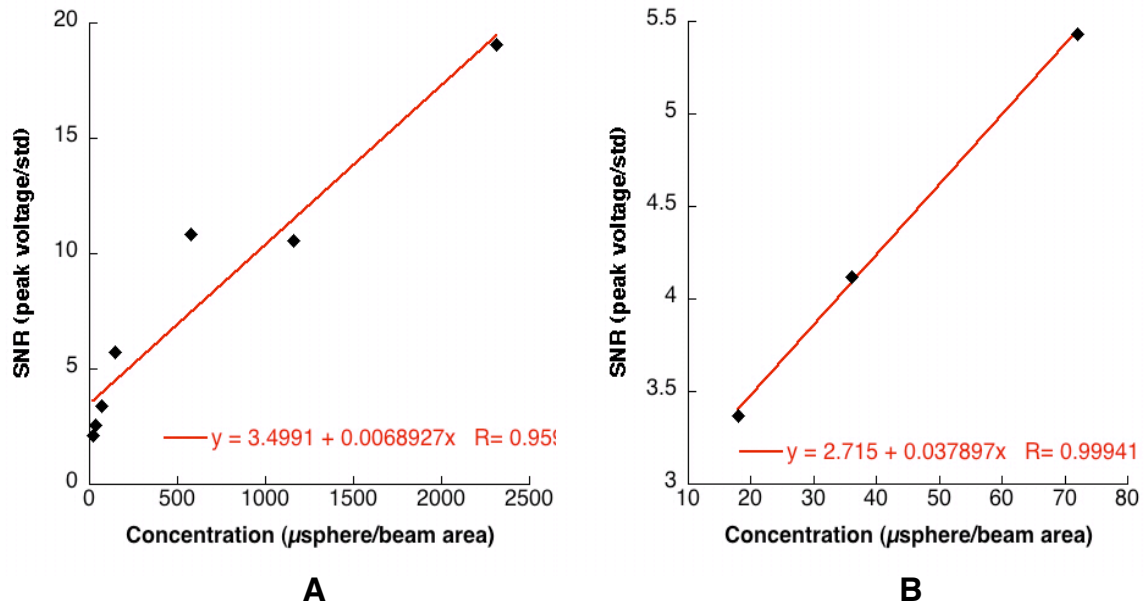


Figure 4.15: A. Signal to noise ratio for all waveforms measured at  $3.0 \mu\text{s}$  with linear curve fit. B. Linear curve fit of lowest concentrations from A measured at  $3.0 \mu\text{s}$ . Linear equation given in red.

signal which occurs at  $3.0 \mu\text{s}$ . This signal is very strong and easily differentiated in these waveforms. The resulting signal to noise ratio for all points measured at  $3.0 \mu\text{s}$  is shown in Figure 4.15A. A magnified view of the three lowest concentrations is given in Figure 4.15B.

## 4.7 Discussion of Custom Design

### 4.7.1 Saline Concentration

Increasing the saline concentration from 0.9% to 1.8% increased the peak signal of a solution by a factor of 1.2, or 0.48 mV. This half a millivolt increase was sufficient to increase all saline concentrations to 1.8% from the time the trial was run, including all custom flow cell trials and melanoma cell trials. This was a very quick and rudimentary study only mentioned as a side note here. Two unknowns must be considered in this matter. First, to what limit of concentrated saline can

a live melanoma cell survive without lysis? Secondly, how much signal can be gained from continually increasing the saline concentration of a solution? Obviously further studies are needed to discover the answer to these questions. Potentially, saline concentration could be increased significantly in order to obtain much more powerful results without compromising the integrity of the melanoma cells.

### 4.7.2 Time Domain Response

The time domain of the signal response is clearly different with the customized flow cell compared to detection trials of previous setups. The results are as expected for a 2 mm wide flow cell. A photoacoustic peak is present at  $1.0\ \mu\text{s}$  and a second peak present at  $3.0\ \mu\text{s}$  (Figure 4.12). The  $1.0\ \mu\text{s}$  peak corresponds to 1.5 mm the acoustic wave must propagate from the excitation source for this particular setup (see Section 4.5.2). The  $3.0\ \mu\text{s}$  peak corresponds to the reflection wave most likely propagating of the wall opposite the PVDF film and thus requiring the wave to travel at least 4.5 mm in solution before being detected.

### 4.7.3 Peak Signal Intensity

The peak signal intensity was generated from the  $8.9 \times 10^4\ \mu\text{sphere/ml}$  solution (the most concentrated solution tested for this trial) and measured at 13 mV (Figure 4.12). The maximum peak intensity for the previous sensitivity characterization using the older design (Section 4.4.3) yielded 5.4 mV for the identical solution and amplification. This results in a 7.6 mV increase in signal strength from the old single chamber setup to the customized flow cell.

Once the concentration of solutions decreased to  $5.5 \times 10^3\ \mu\text{sphere/ml}$  the signal at  $1.0\ \mu\text{s}$  began to become integrated into the noise produced from the firing of the laser (see Appendix B). Although the signal remained clearly differentiated, its amplitude began to take on a stochastic behavior most likely due to interactions with the noise from the laser firing. In a way, this is beneficial as it serves as natural amplification of the signal which can be used to detect low concentrations of cells. However, the nonlinearity of that signal (see next section) provides unreliable



results. Therefore, beginning at  $5.5 \times 10^3$   $\mu\text{sphere/ml}$ , signals were measured from the  $3.0\ \mu\text{s}$  reflection peak which remained differentiated throughout these trials. The smallest measured signal intensity was derived from the  $3.0\ \mu\text{s}$  point of the  $7.0 \times 10^2$   $\mu\text{sphere/ml}$  solution at 1.44 mV. This is 0.56 mV stronger than the trial conducted at the same concentration with the previous flow cell which measured 0.88 mV with a gain of 125.

The post-experimental control waveform shown in Figure 4.13 displays a residual signal phenomena common to these experiments. This residual signal at  $3.0\ \mu\text{s}$  measures 0.8 mV and is the result of excess microspheres that adhere to either the glass surface of the flow cell or the crevices present surrounding the PVDF film attachment site. These residual chromophores, left during the course of the experiments, are excited whenever a new solution is tested and a residual signal results (note no residual signal in pre-experimental control, Figure 4.12). This issue can often be resolved by cleaning the flow cell between trials with KOH solution. However, due to the time constraints, that was not possible. Subtracting the 0.8 mV from the control waveform from the 1.44 from the lowest intensity waveform results in a voltage peak of 0.64 mV.

It should be noted that at lower concentrations a large amount of noise was introduced into the system from a time greater than  $3.0\ \mu\text{s}$ . The reasons for which are yet unknown. The results were not affected by the introduction of this signal.

#### 4.7.4 Threshold

The threshold, as measured by this series of experiments, is **18.3 microspheres per illuminated beam path**. This number is derived from Equation 4.2 and displayed in Figure 4.15. This threshold could certainly be lower had the experiment been ran further considering that detection peaks at both  $1.0\ \mu\text{s}$  and  $3.0\ \mu\text{s}$  are differentiated at 3.68 mV and 1.44 mV respectively. **This would easily translate into single cell detection upon further study.**

The signal to noise ratios of the peak voltages resulted in a linear relation with concentration (Figure 4.14 and 4.15). However, at low concentrations the signals

became nonlinear as described in Section 4.7.3 and shown in Figure 4.14. Because of this, more stable data was taken from the reflection peak at  $3.0\ \mu\text{s}$  and resulted in a completely linear plot shown in Figure 4.15. The last three concentrations of  $2.7 \times 10^3\ \mu\text{sphere/ml}$  to  $7.0 \times 10^2\ \mu\text{sphere/ml}$  at  $3.0\ \mu\text{s}$  displayed a perfectly linear response (Figure 4.15B) allowing for accurate characterization of unknown solutions as described in Section 4.5.3.

The data including all points (Figure 4.15A) resulted in a slope of  $6.89 \times 10^{-3}$  which differs from the theoretical slope of  $8.63 \times 10^{-3}$  by only 20.1%. It is believed that the results would have shown an even more linear response had there not been an experimental error introduced at the third data point of  $2.2 \times 10^4\ \mu\text{spheres/ml}$ . The PVDF film was replaced at this point due to a leak. One can see the direct result of doing so in mid-trial as the signal jumped significantly at that point. It would take 145 microspheres/beam area to increase the voltage by 1 mV at high concentrations and would require 14 microspheres/beam area to increase the signal by 0.1 mV, a detectable increase. The lowest three concentrations had a slope of 0.0378 indicating a strong increase in signal response at low concentrations. This slope varied 50.3% from the theoretical slope of 0.0763. It would take 26 microspheres/beam area to increase the voltage by 1 mV at high concentrations and would require only 2.6 microspheres/beam area to increase the signal by 0.1 mV. This shows that not only is the system more sensitive to low concentration solutions but that the current sensitivity of the system is as low as 2.0 microspheres/beam area.

#### 4.7.5 Effects of Modification

The effects of modifying the system from its original design were quite significant. Total signal strength was increased 272% from the initial dual chamber design to the single chamber design. Subsequently, signal strength was again increased by 240% from the hand crafted single chamber design to the implementation of the Spectrocell custom flow cell design. In addition, the system has evolved to become an efficient, leak free design that is relatively easy to use and provides unprecedented results for circulating detection of photoacoustic absorbers.

## 4.8 Conclusions

Photoacoustic detection of tissue phantoms in the form of  $6.6\text{ }\mu\text{m}$  black latex microspheres was shown to be extremely successful. The development and modification of the detection mechanism has gone through a number of transformations and improvements upon design, all of which have helped to make the device as successful as it is in its current form. The mechanism functions best when 1.8% saline solutions are used to circulate cells of interest. However, further experiments should be conducted to determine the maximum saline threshold and any signal enhancement it might provide. A detection threshold of 18 microspheres has been successfully completed with a signal strong enough to infer an even lower threshold upon further experimentation. An amazingly accurate sensitivity of 2.0 microspheres per irradiated beam path has been described in these results. It could be easily inferred that this system is capable of detecting the presence of single cells in a circulating solution.

## Chapter 5

# Detection of Tissue Phantoms Isolated in the Peripheral Blood Mononuclear Cell Layer

### 5.1 Introduction

The goal of this work is to develop the ability to detect cancerous melanoma cells circulating within the hematogenic system of a potential cancer patient. However, the detection system can only process materials through *in vitro* analysis which requires a method for extracting the cells of interest from a human patient. A simple blood draw is the most common method for obtaining cells present in the circulatory system and may be used as a relatively pain-free, routine method for obtaining particular samples of interest. Once a blood sample is collected, it is proposed that metastatic melanoma cells can be accurately isolated from whole blood *in vitro* by implementing a Ficoll-Hypaque centrifugation technique. This technique requires the extracted whole blood to undergo centrifuge gradient separation in order to isolate the particular cell layer of interest before introducing it to the photoacoustic detection system.

The next step in expanding upon the proof of principle for the device was to show that chromophores could be isolated and detected from a whole blood medium. To test this theory, tissue phantoms representing biological melanoma were introduced into healthy samples of blood *in vitro* and detected using the photoacoustic method.

This section describes the methodology for isolating circulating tumor cells from whole blood and presents experimental data for the detection of latex microspheres embedded in human blood samples.

## **5.2 White Blood Cells and the Peripheral Blood Mononuclear Cells**

Leukocytes, or white blood cells, defend the body against infecting organisms and foreign agents, both in tissue and in the bloodstream itself. Human blood contains about 5,000 to 10,000 leukocytes per cubic millimeter; the number increases in the presence of infection. Leukocytes are formed from stem cells in the bone marrow. They have nuclei and are classified into two groups: granulocytes and agranulocytes. [27]

Granulocytes form in the bone marrow and account for about 70% of all white blood cells. Granulocytes include three types of cells: neutrophils, eosinophils, and basophils. Neutrophils constitute the vast majority of granulocytes. The main purpose of these cells is to surround and destroy bacteria and other foreign particles as well as act in inflammatory response mechanisms during infection or allergic reaction. [27] Granulocytes serve as the first line of defense against infection by foreign cells.

Agranulocytes include monocytes and lymphocytes. Monocytes are derived from the phagocytic cells that line many vascular and lymph channels, called the reticuloendothelial system. Monocytes ordinarily number 4% to 8% of the white cells. They move to areas of infection, where they are transformed into macrophages, large phagocytic cells that trap and destroy organisms left behind by the granulocytes and lymphocytes. Lymphocytes, under normal conditions, make up about 20% to 35% of all white cells, but proliferate rapidly in the face of infection. There are two basic types of lymphocytes: the B lymphocytes and the T lymphocytes. B lymphocytes tend to migrate into the connective tissue, where they develop into plasma cells that produce highly specific antibodies against foreign antigens. Other B lymphocytes act as memory cells, ready for subsequent infection by the same organism. Some T

lymphocytes kill invading cells directly; others interact with other immune system cells, regulating the immune response. [27]

Peripheral Blood Mononuclear Cells (PBMCs) is a term used to describe monocytes and lymphocytes that can be separated from a whole blood solution using a Ficoll-Hypaque centrifugation technique described in Section 5.3.2. Although conflicting information exists on metastatic disease and its interactions with the human immune system, it is hypothesized by this research group, with the confidence of Dr. David Lee of the Microbiology and Immunopathology department of the University of Missouri-Columbia, that antigens present on the surface of melanoma cells within the blood stream of an individual with metastatic disease will be recognized and bound by these mononuclear cells. This assumption is based upon the idea that metastatic disease is a *chronic* disease which persists in the blood stream and would be primarily attacked by monocytes and lymphocytes that are thought to defend against chronic illness more so than granulocytes. Therefore, isolation of the peripheral blood mononuclear cell layer should result in the isolation of any melanoma cells present in the blood stream.

## 5.3 Materials and Methods

### 5.3.1 Blood Draw

Samples of healthy, cancer free blood were drawn from consenting individuals from within the lab group, namely the author of this manuscript. Samples were taken by venipuncture from the antecubital area of the arm in the amount of 10-50 cubic centimeters using a standard blood draw procedure. Ethylenediaminetetraacetic acid (EDTA) liquid coated tubes were used for blood collection to inhibit clotting. Blood samples were stored in a refrigerated environment for no more than five hours before being processed.

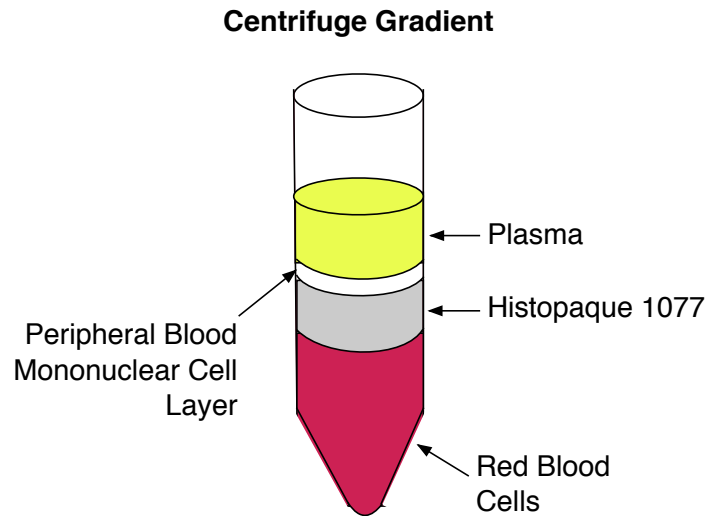


Figure 5.1: Representation of Ficoll-Hypaque blood separation indicating location of peripheral blood mononuclear cell layer.

### 5.3.2 Isolation of Mononuclear Cell Layer

A Ficoll-Hypaque separation technique was used to isolate the peripheral blood mononuclear cell layer from the whole blood samples. The Ficoll-Hypaque process employs a sugar compound of a specific density that separates specific blood components by a density gradient when centrifugal force is applied. Approximately 1 ml of Histopaque 1077 (Sigma-Aldrich Inc., St. Louis, MO) separation gradient was placed in Pyrex No. 9800 glass tubes (Corning Inc., Acton, MA). Approximately 7 ml of blood from the refrigerated samples were gently poured on top of the Histopaque 1077 and stopped with a rubber stopper. The sample tube was then placed in a 60 Hz 3400 rpm Vanguard 6500 centrifuge (Hamilton Bell Co., Montvale, NJ) and spun for 10 minutes. The resulting gradient and relative location of the PBMC layer is shown in Figure 5.1. The peripheral blood mononuclear cell layer consisting of monocytes and lymphocytes separates out directly above the Histopaque layer and below the plasma. The Granulocytes are larger and separate below the Histopaque layer, directly above the blood layer (not shown).

Following separation, the differentiated PBMC layer was carefully removed using

standard transfer pipets (Samco Scientific Corp., San Fernando, CA) and placed into 1.5 ml Flat Top Microcentrifuge Tubes (Fisher Scientific, Pittsburgh, PA). The PBMCs in the microcentrifuge tubes were washed in a saline solution and re-spun for 5 minutes. Excess saline solution and plasma was pipetted off of the top of PBMC layer. This was repeated until peripheral blood mononuclear cells were cleanly isolated.

### 5.3.3 Introduction of Microspheres

Two suspensions of isolated mononuclear cells (0.111 g) were added to 20 ml of a 0.9% saline solution. One suspension served as the control. The second suspension contained 0.5 ml ( $1.49 \times 10^8$ ) of black latex microspheres (Section 4.2). Both were introduced to the photoacoustic detection system.

A third test sample was created in which 1 ml ( $2.98 \times 10^8$ ) of 6.6  $\mu\text{m}$  black latex microspheres was added to 7 ml of human blood sample prior to Ficoll-Hypaque centrifugation. The Peripheral blood mononuclear cell layer was isolated as previously described, added to 20 ml of 0.9% saline, and introduced into detection system.

All trials were run with the following parameters: 450 nm excitation, amplification  $\times 25$ , averaged over 128 data acquisitions, 9 ml/min flow rate, 9.5-10.5 mJ input energy, and a spot size of 0.16 x 0.16 cm ( $0.0256 \text{ cm}^2$ ) resulting in a radiant exposure of  $0.39 \text{ J/cm}^2$ .

It is not yet known how live melanoma cells will separate out in blood. It is postulated that melanoma cells in the blood stream of a metastatic patient may remain in the plasma when subjected to the Ficoll-Hypaque gradient. For this reason, a separate trial was conducted using isolated blood plasma to determine the dynamic ability of the detection system to function using different mediums. Two samples were prepared, a control sample consisting of 3 ml of human plasma and 10 ml of 0.9% saline and a test sample of the same solution with 0.5 ml ( $1.49 \times 10^8$ ) black microspheres added, to mimic the presence of melanoma in plasma. Similar experimental parameters were used as before, only a 595 nm excitation wavelength was used to eliminate absorption by the naturally yellow pigmented plasma.



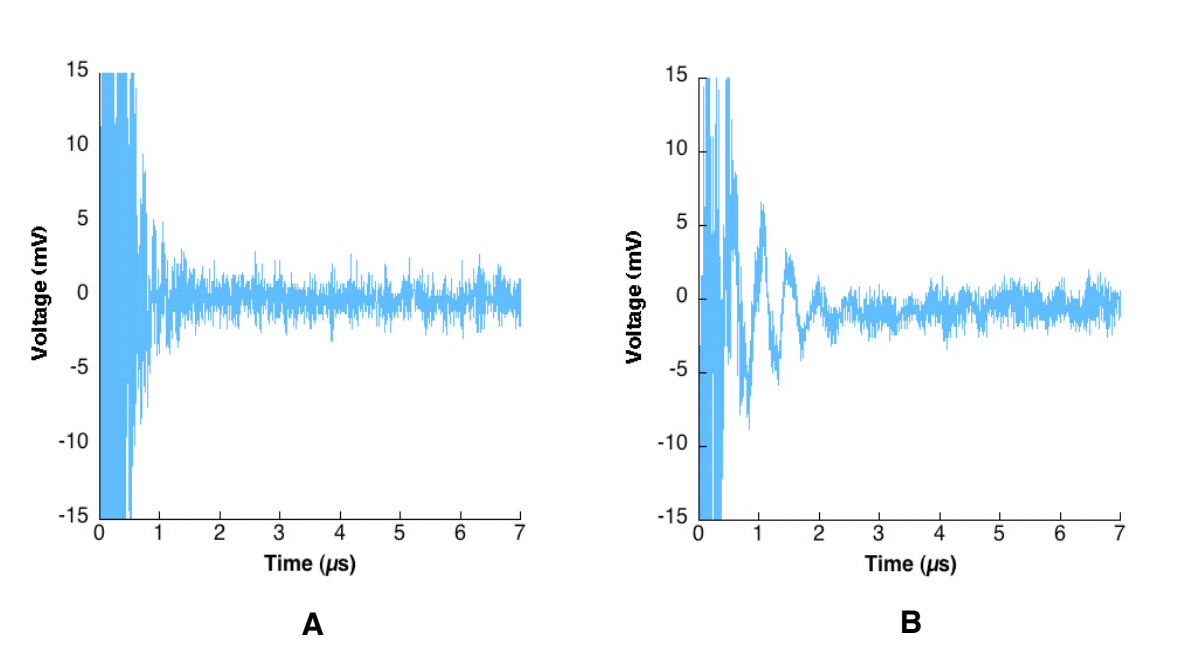


Figure 5.2: A. Control waveform of a 0.9% saline solution. Amplification x 25. 450 nm excitation. B. Photoacoustic results for a control agranulocyte cell suspension with no addition of microspheres. Amplification x 25. 450 nm excitation.

## 5.4 Results

### 5.4.1 Mononuclear Cell Layer Control

Figure 5.2 shows the waveform of a mononuclear cell suspension as a control solution. The waveform for a 0.9% saline solution is included in the figure for comparison.

### 5.4.2 Post-Mononuclear-Cell-Isolation Addition of Microspheres

After isolation of the peripheral blood mononuclear cell layer, a saline/ mononuclear cell suspension was made to which  $1.49 \times 10^8$  microspheres ( $7.12 \times 10^6$  per ml) were added. The resulting waveform is shown in Figure 5.3.

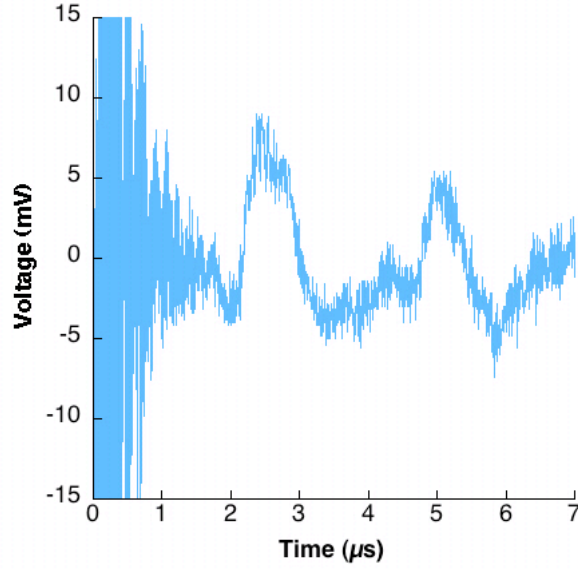


Figure 5.3: Photoacoustic waveform of a post-PBMC-isolation addition of microspheres.  $3.56 \times 10^6$   $\mu$ spheres/ml mononuclear cell solution. Amplification  $\times 25$ . 450 nm excitation.

### 5.4.3 Pre-Mononuclear-Cell-Isolation Addition of Microspheres

Previous to the isolation of the PBMC layer,  $2.98 \times 10^8$  microspheres ( $3.56 \times 10^6$  per ml) were added to a whole blood sample. The blood/microsphere mixture then underwent Ficoll-Hypaque centrifugation in order to isolate the PBMC layer. The photoacoustic results are shown in Figure 5.4.

### 5.4.4 Plasma

Figure 5.5A shows the control waveform for the plasma/saline solution excited at 595nm. Clear photoacoustic excitation of  $1.49 \times 10^8$  microspheres ( $6.0 \times 10^6$  per ml) added to the plasma/saline solution is shown in Figure 5.5B.

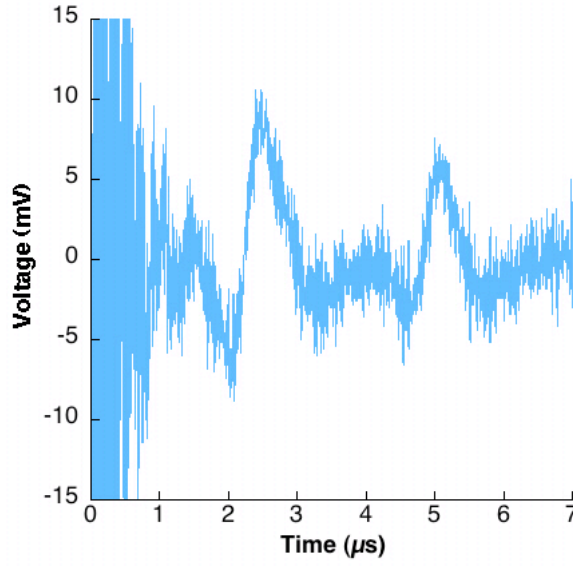


Figure 5.4: Photoacoustic waveform of a pre-PBMC-isolation addition of microspheres.  $7.124 \times 10^6$   $\mu$ spheres/ml mononuclear cell solution. Amplification x 25. 450 nm excitation.

## 5.5 Discussion

### 5.5.1 Controls

The control waveform for the mononuclear cell suspension (Figure 5.2) is important in that it shows that there is no photoacoustic excitation that occurs from exciting the PBMCs. This is expected since mononuclear cells are white in color and should contain no active chromophores that may produce a photoacoustic signal. An interesting oscillating waveform appears between 0 and 2.0  $\mu$ s in addition to a number of small stochastic peaks that continue on past 2.0  $\mu$ s. This waveform is most likely attributed to a pyro-electric effect caused by laser light interactions with the PVDF film. This effect is made possible by the increased light scattering properties of the mononuclear cells. This phenomena is reflected in the waveforms of the solutions containing microspheres described in the next section.

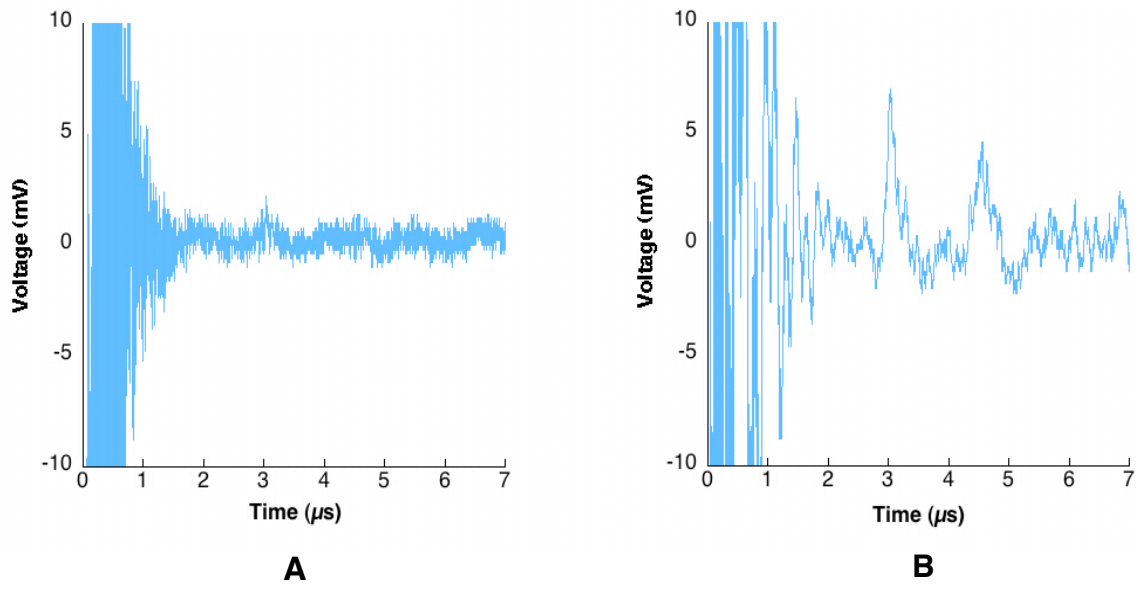


Figure 5.5: A. Control waveform of a 3 ml plasma/ 10 ml saline solution. Amplification  $\times 25$ . 595 nm excitation. B. Photoacoustic waveform of the same plasma solution with the addition of  $1.49 \times 10^8$  ( $6.0 \times 10^6$  per ml) black latex microspheres. Amplified  $\times 25$ . 595 nm excitation.

### 5.5.2 Peak Values

The photoacoustic waveform resulting from the addition of microspheres to an isolated mononuclear cell suspension (Figure 5.3) clearly shows the ability of the detection system to identify chromophores amongst a circulating PBMC solution. Photoacoustic peaks appeared at 2.7 and 5.2  $\mu\text{s}$  with peak values of 9 mV and 5.4 mV respectively. These signals are derived from a very strong concentration of microspheres, nevertheless, it proves that detection is possible. The signals occurred on a time scale typical of that of the older single chamber flow cell which was used for these trials. In these trials, however, signal peaks only occur at 2.7 and 5.2  $\mu\text{s}$  as opposed to 2.6, 3.2, 4.2, and 5.2  $\mu\text{s}$  as in saline trials (see Figure 4.6). The exact reason for this characteristic mononuclear cell/microsphere signal response remains undetermined although it is speculated that acoustic signals may be absorbed by the presence of the many cell bodies present within the detection chamber. It should also be noted that the negative component of the bi-polar waveform does not appear following a positive signal in these trials. This insinuates that the inhomogeneity of the mononuclear cell structure results in a variegated acoustic diffraction which ends up being averaged out of the resulting waveform (see Paltauf *et. al.* [3]). Thus, only a positive photoacoustic signal peak is displayed from a mononuclear cell solution as well as a melanoma cell solution as seen in Chapter 6.

The waveform resulting from the addition of microspheres to whole blood previous to centrifugation is representative of melanoma cells present in the blood stream itself (Figure 5.4). The microspheres were added in large concentration so that if all the spheres were isolated properly,  $7.12 \times 10^6$   $\mu\text{spheres/ml}$  would result in solution. This was most likely not the case as it can be assumed that many microspheres were lost during the process of separation. The resulting waveform shows that Ficoll-Hypaque centrifugation is extremely successful in isolating tissue phantoms representing melanoma cells, proving this research group's hypothesis correct. Peaks were similar to that of the post-isolation microsphere addition at 2.7 and 5.2  $\mu\text{s}$  which reconfirms the detection of microspheres within solution. The peak signals presented maximum values of 10.6 mV and 7.6 mV measuring an average of 2 mV

higher than that of the post-isolation addition waveform. This can be attributed to the increase in amount of microspheres added to the whole blood sample as compared to the post-isolation mononuclear cell solution. The photoacoustic peaks of the pre-isolation waveform are noticeably sharper than that of the post-isolation waveform. This hints at a decrease of microspheres in free space due to the binding capabilities of mononuclear cells acting out an immune response in whole blood.

### **5.5.3 Plasma**

The extraction of blood plasma shows a second possible method for detecting chromophores amongst a non-saline solution. Microspheres were accurately detected at high concentrations at 595 nm (Figure 5.5). This shows the versatility of wavelength modification for detection. 595 nm does not excite the yellow pigmented plasma (as seen in the control) primarily because plasma absorbs in the blue and red spectrum. Still, 595 nm provides photoacoustic excitation for tissue phantoms present in solution due to the broadband absorption of the microspheres. This provides a mode for detection of cells isolated to the blood plasma, which may prove helpful in the future.

## **5.6 Conclusion**

Photoacoustic response from tissue phantoms inoculated into healthy blood can be accurately isolated and detected using the photoacoustic detection system. These results are monumental in showing that a methodology exists to extract cells evenly distributed amidst hundreds of millions of blood constituent cells not of interest to this project. It also shows the ability of the detection setup to express the presence of chromophores amongst a mononuclear cell suspension which eliminates the need for a further cell isolation method not yet in existence. It is proposed that live malignant melanoma cells will reside in the same Ficoll-Hypaque gradient as the tissue phantom cells. However, it is possible that the melanoma cells, being larger than the microspheres and of different makeup, may separate differently, possibly to the granulocyte layer. Further experimentation is necessary to elucidate the answer.

## Chapter 6

# Detection Trials Incorporating Live Melanoma Cells

### 6.1 Introduction

Detection trials to this point have shown that the device can successfully detect chromophores in solution on the order of twenty single cells with the possibility of increasing that threshold with simple system modifications and further experimentation. The sensitivity of the current detection setup is as low as two microspheres. It has also been shown that melanoma phantoms can be added to healthy blood, isolated, and detected using methods described in Chapter 5.

The next step in determining the system's ability to detect disseminated cancer cells is to test its ability to detect melanoma cells *in vitro*. In order to do so, a live melanoma cell line was cultured so that an abundance of isolated melanin could be introduced into the system for detection. This chapter describes the cell line used and cell culturing methods employed. It also describes in detail the methods used for detecting live melanoma and how it was determined that the resulting signals were indeed produced by melanoma cells as opposed to other absorbers or experimental effects.

## 6.2 Melanoma

Melanoma is a malignant tumor composed of unregulated melanocytes [28]. A melanoma cell is essentially a melanocyte containing one or more mutations that inhibit normal cell growth and regulation. A melanocyte produces coloring in mammals by secreting three unique pigments: the dark insoluble, nitrogenous eumelanins formed from the oxidative polymerization of dihydroxyindolequinones, the sulphur-containing alkali-soluble pheomelanins derived from cysteinyl-DOPA which provide the lighter colors (primarily brown and red-brown), and the amphoteric pheochromes (red and red-orange colors) [29, 30]. These colors are enzymatically synthesized by 10nm granular sites studding the internal walls of the melanocytes [31]. These pigments are termed melanin and are produced in various shapes, sizes, and amounts depending upon the cell. The amount and type of melanin produced determines skin, hair, and eye color in mammals. The melanin produced is encapsulated by the melanocyte providing a pigment to any cell producing melanin. It is the melanin granules encapsulated within the melanocyte, or melanoma cell, that serves as the broadband absorber to produce photoacoustic signals when exposed to incident laser light [2]. Basic melanin structures and experimentally based absorption spectra for different melanosomes are given in Figure 6.1 [31].

Melanins are a broad class of functional macromolecules that together exhibit a band structure model characteristic of an amorphous solid with a broad band absorption spectrum in the visible and UV (as seen in Figure 6.1). Eumelanin, the prevalent pigment, has been shown to efficiently absorb UV and visible photon energy and deactivate with a quantum efficiency of less than 0.05%, which fits its role as a photoprotectant in skin. The mechanism by which this occurs is complicated and not entirely understood. Studies show that melanins consist of small heterogeneous oligomeric units that possess different redox states resulting in a broad range of HOMO-LUMO gaps (energy difference between the highest occupied molecular orbital and the lowest unoccupied molecular orbital). This chemical disorder model allows for broadband monotonic absorption as a consequence of the superposition of a large number of nonhomogeneously broadened Gaussian transitions associated



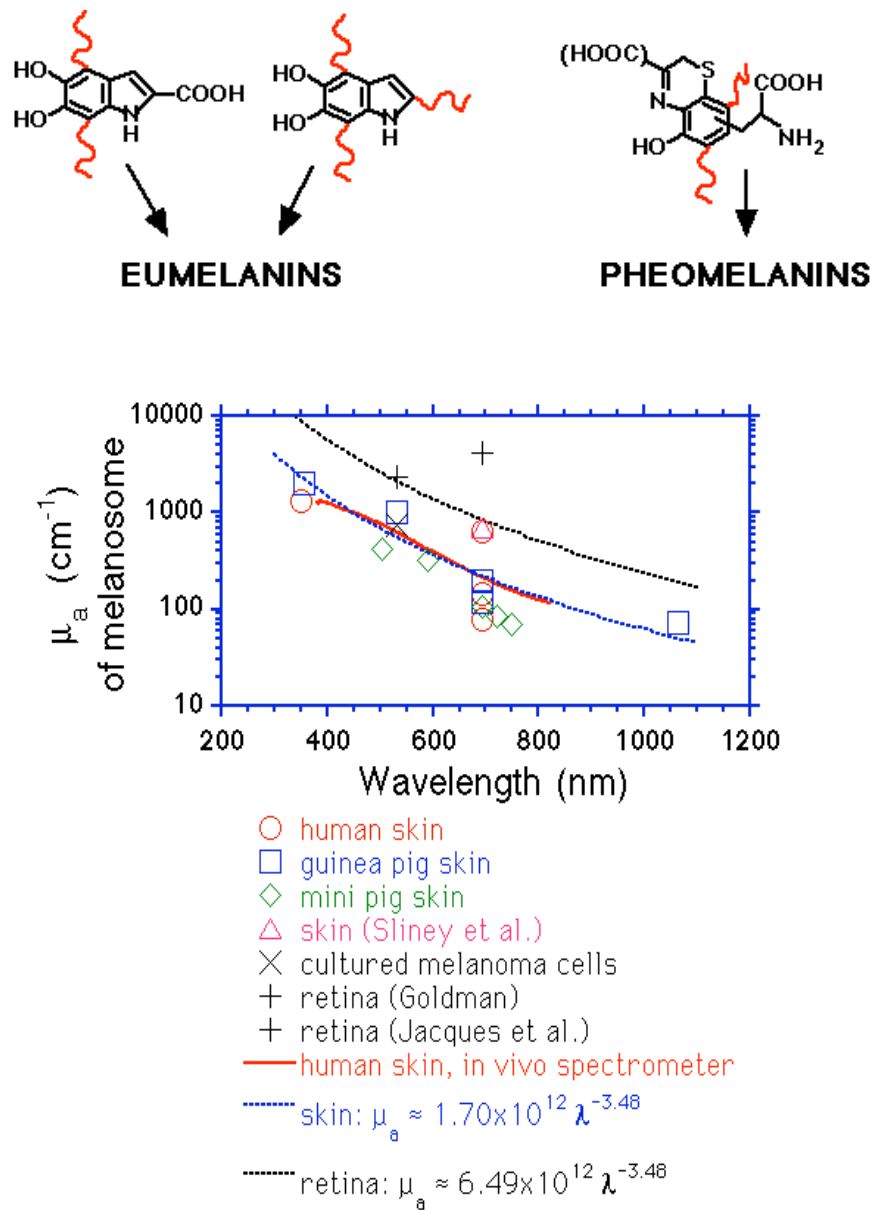


Figure 6.1: Chemical structure of two most abundant types of melanin (top). Absorption spectrum given as a function of absorption coefficient for melanosomes (bottom).

with the components of the melanin ensemble [30]. Despite all the work done to characterize melanin absorption it has been hypothesized that the absorption spectrum of human melanin is dominated by scattering, as it shows no characteristic absorption resonances in the visible or ultraviolet [32].

Melanocytes are present in the epidermal layer of the skin and can give rise to cancerous tumors. Melanoma, therefore, is an epithelial based cancer but does not necessarily include carcinomas and their resulting metastatic cells. Unfortunately, approximately 10% of melanomas consist of amelanotic melanoma cells that do not produce pigment therefore rendering the photoacoustic detection method ineffective for those particular cancers. It has been proposed, however, that molecular tagging mechanisms, including nanoparticle technology, could be used to identify and bind to amelanotic cells, *in vitro*, which would allow for photoacoustic excitation of the bound markers. This could eventually allow for the photoacoustic detection of any melanoma based cancer.

### **6.2.1 Cell Line**

The Melanoma cell line utilized was SK-MEL-1. These cells were originally obtained in 1968 from the thoracic duct lymph of a 29 year old caucasian with rapidly progressing malignant melanoma. The cells are known to be tumorigenic in nude mice or cortisone treated hamsters, producing pigmented malignant melanomas. Additional cellular characteristics included a spherical growth property, with cells loosely clustered, exhibiting a granular cytoplasm. Figure 6.2 shows melanoma cells under microscope after Hematoxylin and Eosin staining and cytopspin analysis. Irregular cell structure can be seen.

### **6.2.2 Medium**

The cells were grown in suspension in 25 cm<sup>2</sup> Canted Neck Flasks with a Phenolic Style Cap (Corning Glass Works, Corning, NY) at 37 degrees Celsius in a humidified 5% CO<sub>2</sub> environment. Approximately 10 ml of the cell suspension was kept in each flask. A media composed of 444.4 ml RPMI (Invitrogen Corp., Grand Island, NY),

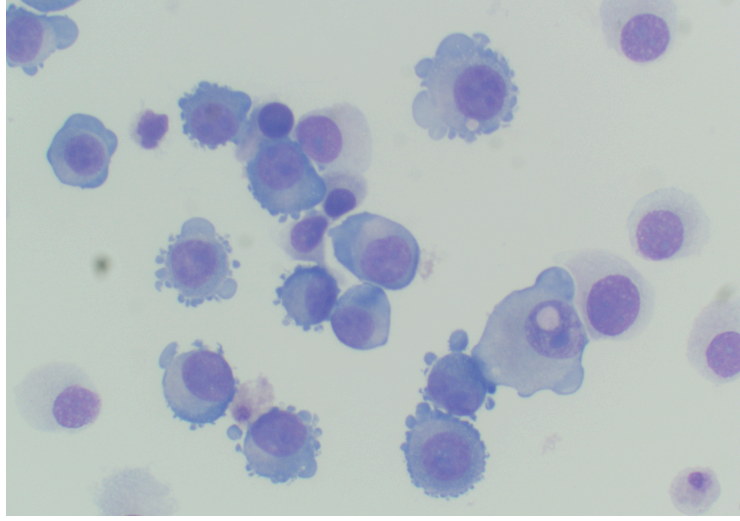


Figure 6.2: Microscopic view of cultured melanoma cells after Hematoxylin and Eosin staining and cytopspin analysis.

5 ml Glutamine (Invitrogen Corp., Grand Island, NY), 50 ml Fetal Bovin Serum (U.S. Bio-Technologies Inc., Pottstown, PA), and 0.6 ml Gentamycin (American Pharmaceutical Partners, Schaumburg, IL) was used and renewed three times per week. When changing the media, 7 ml of the cell suspension was removed and discarded, leaving 3 ml in the original flask. Then, 7 ml of fresh media was then added back to the flask.

### 6.3 Cell Counting

The cells were counted before each media renewal. A small sample of cells would be obtained for the count. The cells were gently mixed with a blue ink at a dilution of 1:2. Using a hemacytometer, the cells in three squares were counted. Equation 6.1 was used to determine the numerical amount of cells present within a culturing flask.

$$\text{Total \# of Cells} = [(C_c)(D)/C_s](1 \times 10^4)(S) \quad (6.1)$$

$C_c$  represents the number of live cells counted,  $D$  is the dilution factor,  $C_s$  is the number of squares counted, and  $S$  is the sample size in ml.

## 6.4 Microscopy and Fontana-Masson Staining

A cytopspin was performed on a selected batch of cells (Figure 6.2). This process involved centrifuging the cells at 1500 RPM for 10 minutes using a Fisher Scientific accuSpin 1 centrifuge. The supernatant was removed and 0.5 ml of a thrombin and plasma solution was added to the remaining cell pellet. This final product was then retrieved and placed in wax paper followed by submersion in zinc formalin for fixation. The tissue was then processed into a paraffin block so further studies could be performed.

The general procedure for regressive Hematoxylin and Eosin staining was performed using Harriss solution. First, the slides were hydrated then stained using Harriss formula for 10 minutes. Next, the slides were rinsed in water to remove the excess Hematoxylin and put in a 1% hydrochloric acid mixture with 70% ethanol for 10 seconds. The slide was then rinsed again and placed in a weak ammonia solution for 60 seconds, washed for 5 minutes in DI water, and counterstained with Eosin for 1 minute. The slides were then twice dehydrated in 95% ethanol for 1 minute. Finally, the samples were dehydrated in absolute alcohol for 1 minute and placed in xylene twice, then cover slipped. The stained cells revealed that individual cells varied in size, with many containing dark, intracellular inclusions. The nuclei were centrally located, round, and contained one or more prominent nucleoli.

Fontana-Masson is a melanin stain that allows for visible determination of melanin content within the melanoma cells. The technique used was the Fontana- Masson Argentaffin Reaction Method. The tissue embedded within the paraffin was cut at 5  $\mu\text{m}$  and affixed to a glass slide. The slide was then hydrated, immersed in silver nitrate solution for 2 hours at 56 degrees C, for 1 hour. The slide was then rinsed in distilled water followed by toning in gold chloride for 2-3 minutes. Rinsing was then repeated and the slide was placed in 5% sodium thiosulfate for 1 minute and rinsed again. Next, a counterstain with nuclear fast red was used for 5 minutes. The slide

was finally rinsed in distilled water twice and then dehydrated and mounted using a synthetic mounting media. Figure 6.3 shows multiple examples of Fontana-Masson staining. Amount of melanin produced varies by cell with approximately 5% of the cells containing dense brown cytoplasmic granules dispersed evenly throughout the cytoplasm. Therefore only 1 in 20 live melanoma cells are actively producing melanin. Mutated aneuploid state of the transformed melanoma is apparent through cells containing multiple nuclei as shown in Figure 6.3.

## 6.5 Materials and Methods

A number of control trials were ran in order to definitively prove the detection of melanoma cells as opposed to other absorbers or pyro-electric effects. These control experiments were ran in addition to detecting melanoma suspensions.

### 6.5.1 White Microsphere Control

In addition to a plain 1.8% saline control solution (as prepared and tested in previous sections), a  $7.124 \times 10^6$   $\mu$ sphere/ml solution was prepared using 6.6  $\mu$ m White CML Latex Microspheres (Interfacial Dynamics Corp., Eugene, OR). Whereas black microspheres represents the absorbing effects of melanoma, white microspheres can be used to represent the scattering effects of melanoma cells. Therefore, the white microsphere suspension was introduced to determine the effects of a purely scattering medium on the system. As described in Section 6.2, live melanoma cells act as both absorbers and scatterers due to their variable melanin content and large amount of *white* surface area. It is possible that a scattering medium (such as melanoma) may produce phantom signals or oscillations due to a pyro-electric effect, or signals produced by scattered photons interacting with the piezoelectric film or electrodes. These control trials give examples of typical pyro-electric waveforms so as to eliminate the possibility of mistaking a pyro-electric signal for that of a melanoma signal.

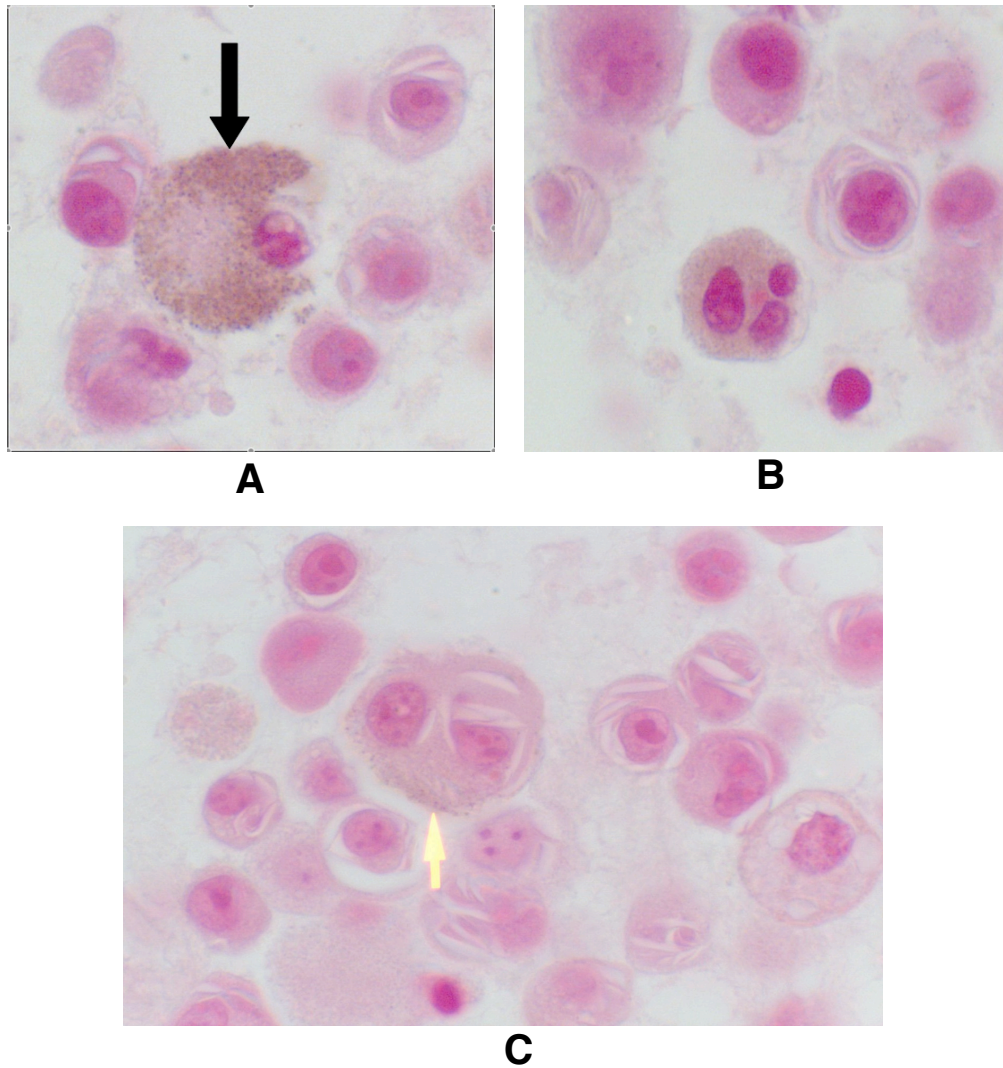


Figure 6.3: Examples of Fontana Masson Melanin Staining. A. Arrow points to large, darkly pigmented melanoma cell. B. Mutated aneuploid cell producing melanin with three nuclei. C. Group of malignant melanoma cells with light pigmentation. Arrow points to melanin granule.

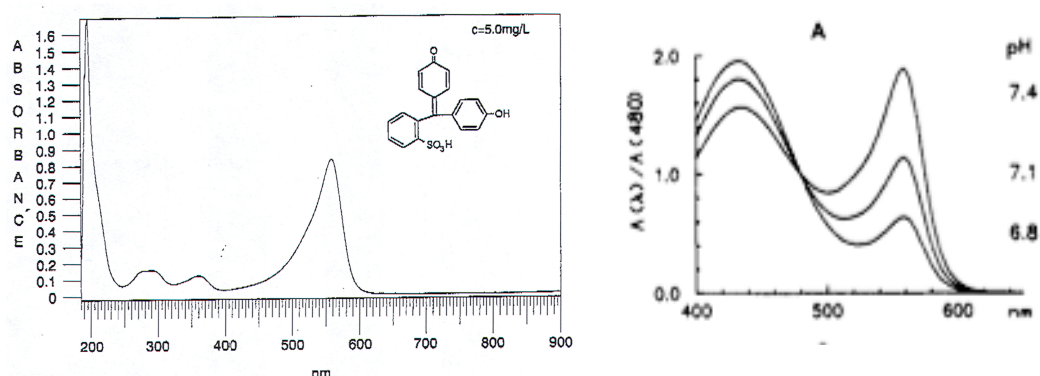


Figure 6.4: Chemical structure and absorbance spectrum of phenol red at various pH. Absorbance spectrum on left is from The Sigma-Aldrich Handbook of Stains, Dyes, and indicators. Spectrum on right is from *in vitro* spectroscopy studies of 0.8 mM solutions of phenol red performed by Baylor *et. al.* Phenol red is a key chemical component of RPMI cell culture medium used to culture melanoma.

### 6.5.2 Medium Control

A second control experiment was conducted using a 1:1 suspension of RPMI Culture Medium (Section 6.2.2) and 1.8% saline. The medium, used to culture the melanoma cells, contains phenol red that serves as an acid/base indicator to identify when the cells have expired the nutrients of the growth medium. Phenol red (Phenolsulfonephthalein) has a pK value of 7.9 and an absorption spectrum shown in Figure 6.4 [33, 34]. Different absorption spectra exist from different sources and detection techniques as can be seen by comparing the two spectra. It is evident that phenol red has a variable absorbance at 450 nm that could produce a photoacoustic signal but no absorbance at 620 nm. Therefore, detection trials were ran at 450 nm and 620 nm for both the culture medium suspension and the melanoma suspension for comparison. This would ensure that any signal produced at 620 nm would be that of the melanoma cells not that of the culture medium either present on the cells or absorbed by the cells. Thus eliminating the notion that the culture medium may be producing a photoacoustic signal mistaken for melanoma.

### 6.5.3 Cell Preparation

Before suspending the melanoma for introduction into the detection system, the cells were counted (see Section 6.3) then spun at 1200 RPM at 4 degrees Celsius for ten minutes using a Fisher Scientific accuSpin 3R centrifuge. The supernatant of media was then removed from the cell pellet formed. Next, the cells were washed using Dulbeccos Phosphate Buffered Saline (Invitrogen Corp., Grand Island, NY). Saline was added to the pellet, the cells were gently mixed, becoming again suspended, and the procedure was repeated using the same methods as described above. Finally, the supernatant of saline was removed, and a small amount of fresh saline was added to the cell pellet.

A 15ml solution was made consisting of  $2.3 \times 10^6$  live melanoma cells and 1.8% saline resulting in a  $1.53 \times 10^5$  cell/ml suspension. This suspension was entered into the most recent setup design and detected with the following parameters: 450 nm and 620 nm excitation, 9.5-11.6 mJ input energy, gain of 25, averaging over 128 data acquisitions, and a flow rate of 0 ml/min.

## 6.6 Results

### 6.6.1 Controls

Figure 6.5 shows the results of the white microsphere control trial as well as a 1.8% saline control waveform for comparison.

Figure 6.6 gives the results of the RPMI culture medium trials at both 450nm and 620nm excitation.

### 6.6.2 Photoacoustic Waveforms

Figure 6.7 shows the photoacoustic waveforms for melanoma cell detection. Two separate waveforms are displayed at 450 nm, one at 9.5 mJ and one at 11.6 mJ input energy for comparison. Also included are the 620 nm excitation waveform and a post-experimental control waveform consisting of 1.8% saline. This was conducted following all trials to ensure that the signals were not that of a residual photoa-



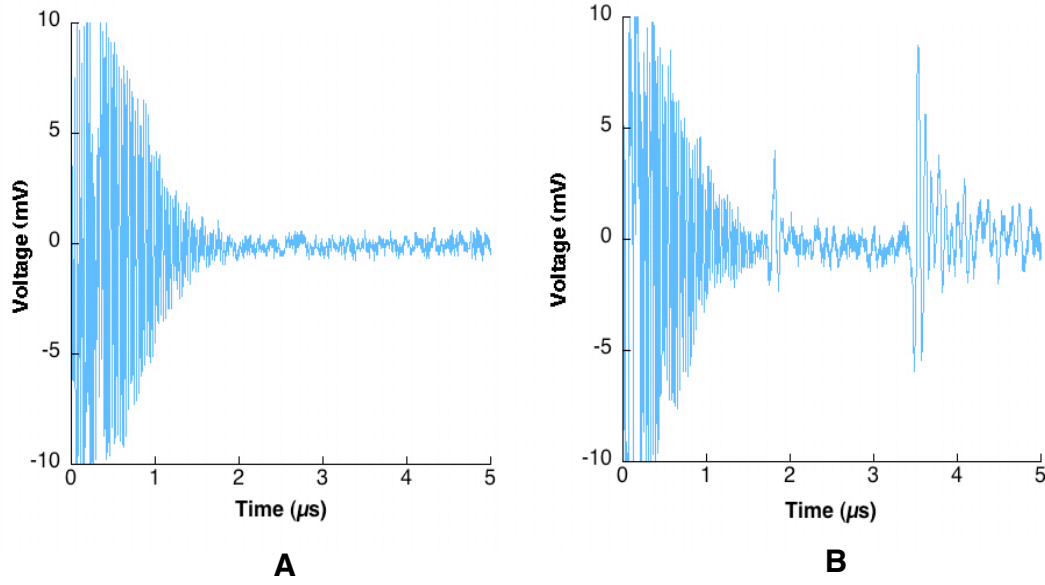


Figure 6.5: A. 1.8% saline control waveform. B.  $7.124 \times 10^6 \mu\text{sphere/ml}$  white microsphere waveform displaying the pyro-electric effect. Excited at 450 nm with 9.5 mJ incident energy. Gain of 25.

coustic source emanating from cells or particles lodged within the flow cell from the experimental trials ran throughout the course of the day.

## 6.7 Discussion

### 6.7.1 Cell Line

The cell line chosen for these trials was a non-clustering metastatic melanoma cell line. The original sample was taken from the metastatic tumor of a class IV cancer patient which insinuates that the cells possess an inherent ability to disseminate and intravasate into the blood stream. Therefore, the cells cultured and tested should be comparable to cells that would be present in the blood stream of a metastatic cancer patient. Approximately 5%, or 1 in 20, of the cultured cells produced visible melanin. The irradiated spot size for these trials was 0.13 cm x 0.2 cm (0.026 cm<sup>2</sup>) with a beam length of 1 cm. If it is assumed that 1 in 20 cells produced viable

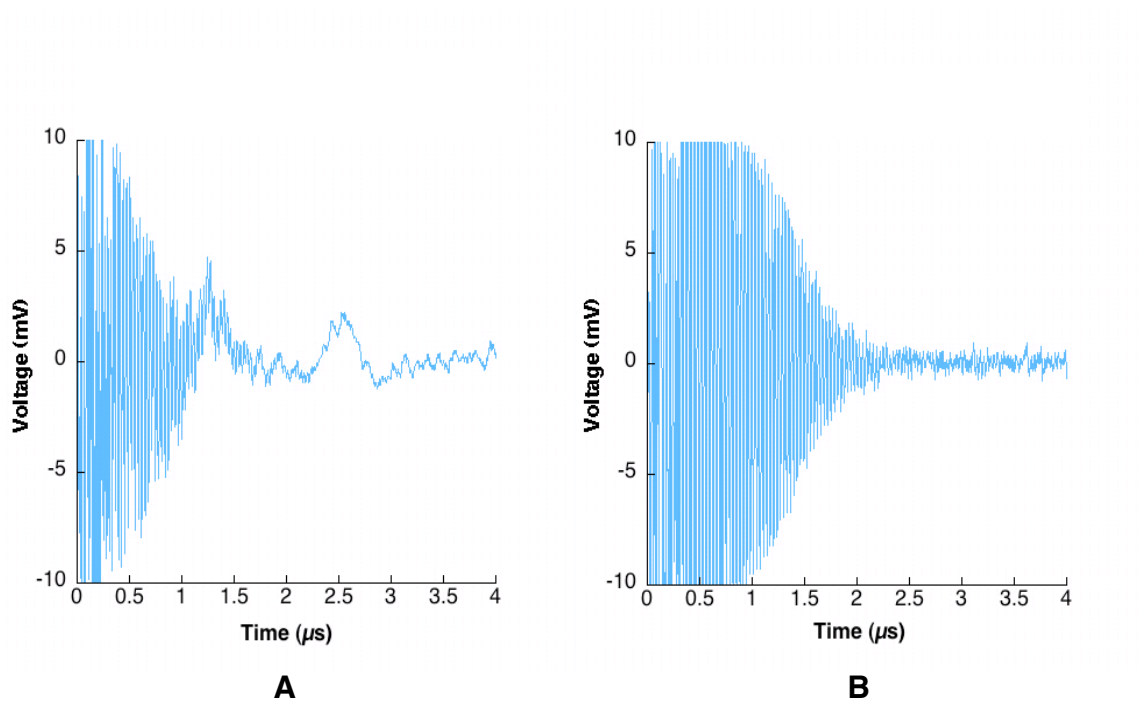


Figure 6.6: A. 10 ml RPMI Culture Medium/10 ml 1.8% Saline solution excited at 450 nm. 9.5 mJ incident energy. B. 10 ml RPMI Culture Medium/10 ml 1.8% Saline solution excited at 620 nm. 7.5 mJ incident energy.

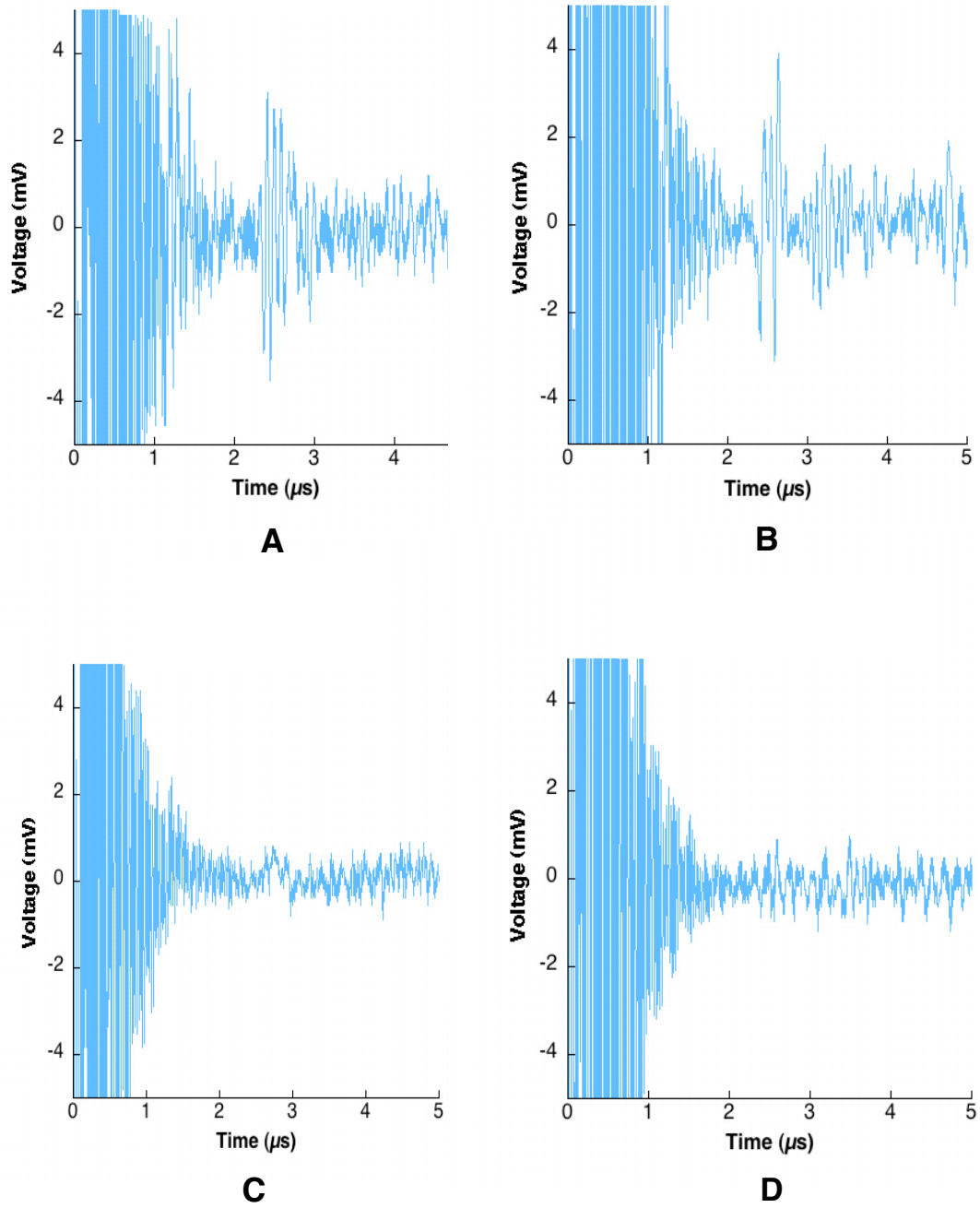


Figure 6.7: A-B. Photoacoustic waveforms for metastatic melanoma.  $1.43 \times 10^5$  cells/ml 1.8% saline. 450 nm excitation. 11.6 mJ incident energy in A, 9.5 mJ in B. C. Photoacoustic waveform for melanoma with 620 nm excitation.  $1.53 \times 10^5$  cells/ml. 6.7 mJ incident energy. D. Post-experiemntal control waveform. 1.8% saline solution. 450 nm excitation with 9.5 mJ incident energy.

melanin then it can be deduced that any resulting signal was produced by 200 melanotic melanoma cells per irradiated beam path.

The melanoma samples were excited by 450 nm excitation due to the optical absorption properties set forth in Figure 6.1. The decrease in absorption with increasing wavelength is evident in Figure 6.7 with a very strong photoacoustic signal at 450 nm and only a mild signal at 620 nm. This can also be attributed to less input energy at longer wavelengths (6.7 mJ versus 9.5 mJ).

### 6.7.2 Peak Values

The live melanoma signals were clearly differentiated and occurred consistently at 2.5  $\mu$ s (Figure 6.7). The signals are clearly unique from those of the RPMI culture medium and the microsphere tissue phantom trials in that they appear in multiple smaller peaks grouped together as opposed to a single peak over the span of 0.5-1.0  $\mu$ s. This is most likely attributed to a pyro-electric effect produced by the melanoma cells. This can be corroborated by a correlation that exists between the pyro-electric signal shown in Figure 6.5 and the peak signal given by the melanoma excitation. Also, a large amount of scattering occurs from the excitation of the melanoma which can be seen by the naked eye during experimentation. Peak values for the two 450 nm excitation peaks shown in Figure 6.7A and B are 3.12 mV and 3.92 mV, respectively. These results are with a gain of 25 allowing for the possibility of increasing the signals by increasing the gain. Nevertheless, these characteristic waveforms clearly show the ability of the detection system to detect malignant melanoma cells *in vitro*.

The peak signals occur around 2.5  $\mu$ s which is not expected of the customized flow cell. Peak signals should occur around 1.0  $\mu$ s with secondary reflection signals occurring at around 2.5-3.0  $\mu$ s as described in Section 4.6.2. However, it is plausible that primary detection peaks do occur around 1.0  $\mu$ s but are not apparent because they merge with the laser noise (this can be seen in Figure 6.7A at 1.0  $\mu$ s). As with the thresholding signals of the customized flow cell given in Section 4.6.2, it is the secondary signals that become prominent and differentiated at low detection levels. This is most likely the case for the melanoma waveforms.

### 6.7.3 Determination of Melanoma Detection

To draw the conclusion that melanoma cells are being detected and not that of secondary absorbers or light scattering effects, one must consider all other forms of potential signal initiation. Figure 6.7C shows the photoacoustic detection of melanoma at an excitation wavelength of 620 nm. This waveform gives a peak value of 0.8 mV and allows for the determination of melanoma cell detection by comparison to the culture medium results in Figure 6.6. At 450 nm excitation, the phenol red present within the RPMI culture medium produces a strong photoacoustic signal in which both the primary and secondary excitation peaks are clearly visible. These peaks occur in the same time domain as that of the melanoma cells and could prove detrimental to the validity of the results. However, the RPMI signal is drastically different from that of the melanoma signals in that it resembles a signal characteristic to that of a waveform produced by a microsphere solution. Secondly, it is shown that the culture medium has no photoacoustic signal at 620 nm whereas the melanoma cells do. This rules out the possibility of photoacoustic signals due to contamination of cells with RPMI culture medium.

Another potential form of false signaling is that of the pyro-electric effect resulting from stray photons exciting the piezoelectric film or electrodes within the detection chamber. Figure 6.5 shows the pyro-electric effect produced by a white microsphere solution. Although there are semblance's in the melanoma waveforms to that of the white microsphere, no pyro-electric peak occurs at  $2.5 \mu\text{s}$  that could be mistaken for melanoma detection. The similarities between the two waveforms is to be expected since melanoma cells are both highly scattering and absorbing.

Finally, it is shown in Figure 6.7D that post-experimentally, after all trials had been conducted, no photoacoustic signal existed from any residual material that may have become trapped within the detection cell during the course of the experiments. The combination of these experimental results shows the successful detection of live malignant melanoma from culture.

#### **6.7.4 Sources of Error**

It should be noted that all detection trials conducted in this section were ran with no flow velocity during the time of detection. The samples were circulated when the detection process was not occurring and the laser was not being fired. The reason for this is because of the presence of a yet unidentified signal that arose from the circulation of samples and firing of the laser. This strange signal had not appeared until this set of trials and did not affect results when samples were not circulating. As a result, samples were sufficiently circulated and then stopped for detection to be conducted. This should not have affected results except for possibly decreasing the strength of the signals by only allowing a small portion of the samples to be excited at once in contrast to averaging a circulating solution.

### **6.8 Conclusion**

Cultured live malignant melanoma was successfully detected using the custom flow cell design of the photoacoustic system. The signals were clearly differentiated and retained a distinct pattern relating to melanoma detection. Results showed that approximately 200 melanotic melanoma cells were required to produce a 4 mV signal. When compared to the threshold trials for the customized flow cell setup in Chapter 4, which gave a peak value of 1.4 mV, the melanoma signal is a 2.8 fold increase in voltage. Assuming a linear correlation of voltage and melanoma concentration, it could be assumed that only 50 melanotic melanoma cells per irradiated beam path would prove sufficient to create an easily differentiated signal of 1.0 mV. Further experimentation and signal enhancement could result in the detection of melanotic melanoma on the order of tens of cells.

# Chapter 7

## Integrating Sphere Theory and Optical Property Determination

### 7.1 Introduction

The determination of optical properties for the black latex microspheres (Chapters 4 and 5) and live melanoma cells(Chapter 6) is vital to the understanding of how the microsphere tissue phantoms compare to the live cells they are trying to represent. Understanding how light interacts with the two absorbing media tested in this thesis will allow for conclusions to be drawn regarding their abilities to produce photoacoustic signals. Once the signal production potential is realized through the determination of optical properties, the photoacoustic response of both the melanoma cell suspensions and the black latex microsphere suspensions can be further explained. From this, data correlations can be made between the sensitivity trials conducted with latex tissue phantoms and the results from actual live melanoma detection.

Integrating spheres offer a method of simultaneously determining the optical properties of materials by employing the Inverse Adding-Doubling Algorithm to measured light flux gathered from the spheres. This chapter details the optical properties of interest, provides a brief explanation of the theory of integrating sphere measurements, describes the methodology used, and discusses the optical properties of the latex microspheres and malignant melanoma.

## 7.2 Optical Properties

There are a number of properties that are used to describe light interactions with turbid media. The three properties we will consider in detail are absorption, scattering, and anisotropy. The most important optical property for the purpose of these experiments is absorption. As described in Chapters 1 and 3, the amount of absorption of a material at a particular wavelength is directly related to the strength of the photoacoustic signal that it produces.

### 7.2.1 Absorption

Absorption occurs when an incident light photon interacts with a molecule that can absorb that photon in the form of molecular energy transition. In the visible spectrum these transitions consist of electron orbital shifts in compounds composed of conjugated dienes. Compounds containing conjugated dienes make up the majority of absorbing materials, or chromophores. The absorption of a compound is described by its absorption coefficient,  $\mu_a$ , defined as the probability of light absorption in an infinitesimal distance  $ds$ , given as  $\text{cm}^{-1}$ . The absorption coefficient is wavelength dependent and is determined by the type of chromophore and its concentration. Assuming a purely absorbing medium, the absorption coefficient can be calculated using Beer's Law given in equation 7.1.

$$I_t = I_o e^{-\mu_a d} \quad (7.1)$$

The equation is described schematically in Figure 7.1. The absorption coefficient is exponentially related to the percentage of transmitted light and dependent upon the thickness of the sample. This describes the simplest method of determining absorption. Realistically, a purely absorbing medium does not exist thus explaining the need for more complicated methods of optical property determination such as the inverse adding-doubling algorithm.



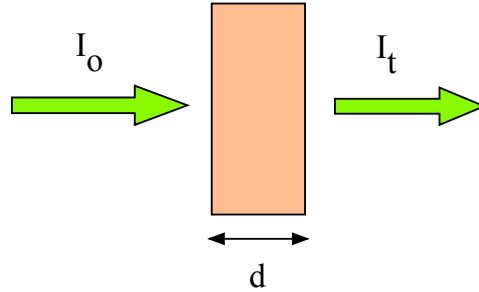


Figure 7.1: Depiction of experimental setup to determine absorption coefficient using Beer's Law.

### 7.2.2 Scattering

Scattering describes the interaction of photons that are not absorbed by a particular medium and is caused by changes in the index of refraction across a material. Optical scattering is described by the scattering coefficient,  $\mu_s$ , and defined as the probability of photon scattering in an infinitesimal distance  $ds$ , given by  $\text{cm}^{-1}$ . The scattering coefficient of a material is based on the volume density of scatterers and is dependent upon the size of the particle. Beer's Law can be used in the same manner as absorption for calculating the scattering coefficient for a purely scattering medium.

### 7.2.3 Anisotropy

Anisotropy describes the amount of light that is forward scattered by a material. The phase function, or angle of light refraction, is characterized by anisotropy,  $g$ , which is the average cosine of the phase function. Anisotropy varies between isotropic scattering ( $g=0$ ) and complete forward scattering ( $g=1$ ). Figure 7.2 gives a schematic representation of isotropic and forward scattering.

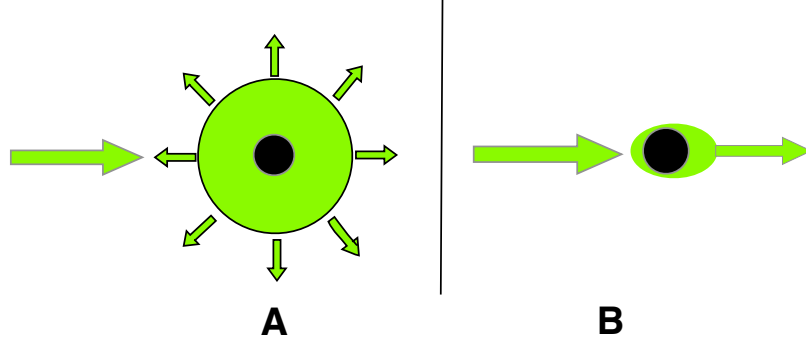


Figure 7.2: A. Representation of isotropic scattering ( $g=0$ ). B. Representation of complete forward scattering ( $g=1$ ).

#### 7.2.4 Other Optical Properties

There are other optical properties that should be briefly mentioned such as the scattering albedo given by equation 7.2. The albedo represents the relative portion of scattering during a light interaction event.

$$a = \mu_s / (\mu_a + \mu_s) \quad (7.2)$$

The total light attenuation coefficient is given in equation 7.3.

$$\mu_t = \mu_a + \mu_s \quad (7.3)$$

The effective attenuation rate for highly scattered media is given by equation 7.4.

$$\mu_{eff} = \sqrt{3\mu_a(\mu_a + \mu_s(1 - g))} \quad (7.4)$$

The mean free path for a photon passing through an absorbing and scattering medium is given by equation 7.5.

$$mfp = 1/\mu_t \quad (7.5)$$

The optical depth for an absorbing and scattering medium is given by equation 7.6.

$$\tau = d(\mu_a + \mu_s) \quad (7.6)$$

Finally, the reduced scattering coefficient describes a highly scattering medium by relating anisotropy to the scattering coefficient as seen in Equation 7.7

$$\mu'_s = \mu_s(1 - g) \quad (7.7)$$

All of these optical properties can be used to decipher the composition of a material and will be presented later in this chapter.

## 7.3 Integrating Sphere Theory

### 7.3.1 Overview

A few select optical properties for melanoma have been reported by *in vivo* measurements [31, 35]. However, these optical properties are limited in scope and specific to models unrelated to metastatic melanoma. For this reason it is necessary to determine the *in vitro* optical properties of the melanoma cell line used in these experiments. This can be accomplished using double and single integrating sphere methods.

When a collimated light beam is placed upon a sample it interacts with the tissue in four ways. The light can either be directly reflected off of the surface of the sample or it is subjected to diffuse reflectance, diffuse transmittance, or collimated transmittance. Figure 7.3 shows a schematic example of possible light interactions. Integrating spheres are hollow spheres coated with a highly reflecting medium. The spheres contain three ports that allow light to enter or escape the sphere. Placing photodiodes or spectrometers in two of the ports and a sample across the other allows for the accurate measurement of the four types of light interactions in the form of voltage or intensity counts. Figure 7.4 depicts a double-integrating sphere setup.

The single and double-integrating sphere systems allow for the simultaneous determination of all optical properties by using the inverse adding-doubling algorithm described in the next section. The single-integrating sphere setup uses a spectrometer to collect light. To measure the reflected and transmitted light from a sample it is situated, respectively, at the exit or entrance port of the sphere. The theory requires

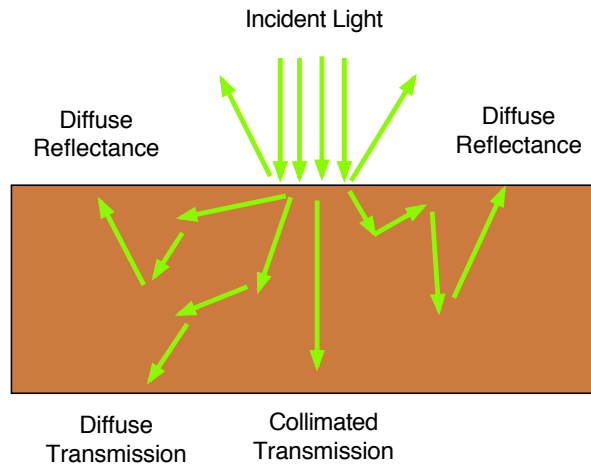


Figure 7.3: A schematic representation of possible light interactions with a sample.

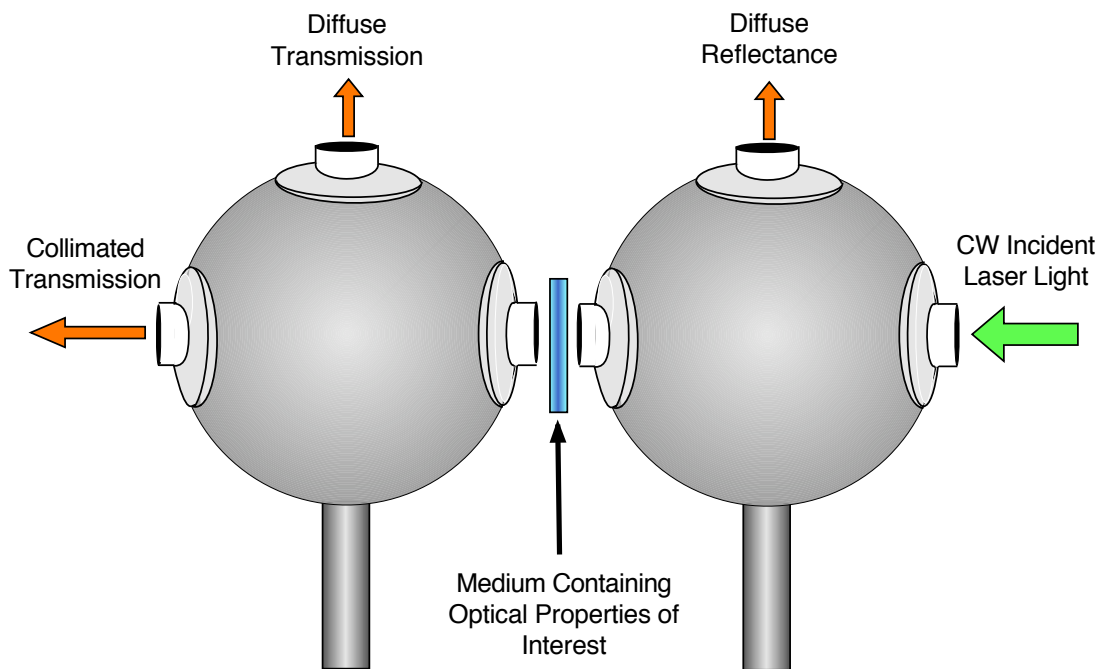


Figure 7.4: A schematic representation of a double integrating sphere setup.

that no directly reflected light from the sample irradiates the detector, thus a baffle is placed between the sample and the detector within the sphere. The integrating-sphere theory accounts for the losses caused by absorption from the sphere wall and light escaping the sphere. The power detected depends on the total light remaining within the sphere and on the relative size of the detector [36].

The double-integrating sphere method (see Figure 7.4) uses photodiodes as light detectors therefore light is measured in the form of voltage. The double-sphere system consists of two spheres with the sample placed between them. If light irradiates the sample in the first sphere (reflectance sphere), a portion of this light will be transmitted through the sample to the second sphere (transmittance sphere). Some of the light within the transmittance sphere will irradiate the *back* of the sample and be transmitted back into the reflectance sphere, thus increasing the signal in the reflectance sphere. This process of transmission of an ever decreasing portion of light through the sample continues until all light has been absorbed or lost from the spheres. The net effect is to increase the signal in both spheres over the single-sphere case [36].

More detailed information on integrating sphere theory including calibration equations and sample and port size determinations can be referenced in Pickering *et. al.* and Prahl [36–38].

### 7.3.2 Inverse Adding-Doubling

To determine the optical properties from the measured light flux in the two spheres an iterative method of the adding-doubling solution of the radiative transfer equation is used [36]. The inverse adding-doubling algorithm (IAD) is appropriate because it allows for the use of collimated and diffuse incident light, is applicable with slab geometry, can account for boundary conditions, and is relatively fast. Optical properties are derived by calculating the expected light fluxes in each sphere with the IAD and comparing these with measured fluxes until a match is achieved [36]. The measurements of the reflection, the total transmission, and the sample thickness allow the determination of  $\mu_a$  and  $\mu'_s$ . The additional measurement of collimated

transmission allows for the separation of reduced scattering coefficient into the scattering coefficient and anisotropy [36].

The adding-doubling method is a general, numerical solution of the radiative transport equation that takes into account boundary conditions needed for turbid materials with mismatched boundaries [39]. The IAD method consists of the following steps: guess a set of optical properties, calculate the reflection and transmission by using the adding-doubling method, compare the calculated values with the measured reflection and transmissions, and repeat until a match is made [39]. The inverse implies a reversal of the usual process of calculating reflection and transmission from optical properties. The doubling method assumes that the reflection and transmission, including corresponding angles, is known for a single layer slab. The reflection and transmission of a slab that is twice as thick is found by juxtaposing two identical slabs and adding the contributions from both slabs, thus doubling the values. The adding component extends the doubling method to dissimilar slabs thus simulating a layered media or internal reflection caused by index-of-refraction differences [39]. Further details regarding the IAD method are described by Prahl *et. al.* [39]

### 7.3.3 Non-Linear Behavior of Detectors

The double-integrating sphere method utilizes photodiodes as light flux detectors. These photodiodes have an experimentally derived non-linear behavior described by Figure 7.5. Therefore, voltage measurements from the detectors must be characterized by the corresponding laser power and normalized over the incident power from the laser before being entered into the inverse adding-doubling method. This was carried out following a curved fit 6,7, and 8 order polynomial for each of the three detectors; collimated transmission, diffuse transmission, and diffuse reflectance, respectively.

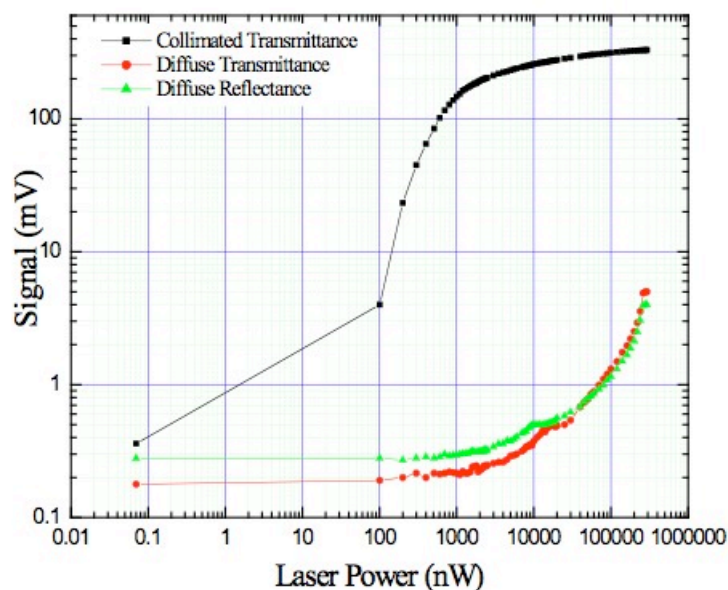


Figure 7.5: Polynomial curve fit of photodiode detectors for double-integrating sphere setup.

## 7.4 Double-Integrating Sphere Materials and Methods

### 7.4.1 Experimental Design

Two integrating spheres (LabSphere, North Sutton, NH) were arranged in alignment, as shown in Figure 7.4, so that samples could be placed between the two spheres for analysis. One of the two integrating spheres was placed on a micrometer so that samples could be easily added and removed. The samples were *sandwiched* between the two spheres and held in place by pressure. Sample cuvettes of 1 mm and 5 mm were constructed from standard 1 mm glass slides (Fisher Scientific, Hampton, NH) and 100% silicone sealant (Dow Corning, Baltimore, MD) to house the sample solutions. Originally, optical properties were derived using the 1 mm cuvettes, however, it was determined that 5 mm cuvettes provided more accurate results due to greater sample volume. Samples were tested using three different

HeNe lasers; a 543 nm laser, a 594 nm laser, and a 633 nm laser (Melles Griot, Carlsbad, CA). The three wavelengths were chosen arbitrarily in order to measure the effects of wavelength on the optical properties of the samples. Previous to the laser entering the integrating spheres, the light was passed through two polarizers and a cubed beam splitter (Thorlabs, Newton, NJ). One beam continued on to the integrating spheres while another entered a S/N 2705 Universal Fiber Optic Detector leading to a 2835-C Multi-Function Optical Meter (Newton, Stratford, CT). The optical meter allowed for the determination of input laser power which was held constant at  $245 \mu\text{W}$  for one trial and  $10 \mu\text{W}$  for a second trial. Optical photodiodes were affixed to the diffuse transmission and diffuse reflectance ports to measure the transmitted and reflected light from the sample as shown in Figure 7.4. The collimated photodiode was placed 60 cm from the exit port to avoid detection of diffuse transmission exiting the transmission sphere [36]. The photodiodes were connected to a TDS 2024 200 Mhz Oscilloscope (Tektronix, Beaverton, OR) which displayed photon density in the form of a voltage signal. All trials were conducted in a dark room to eliminate undesired effects from stray light.

### 7.4.2 Sample Preparation

Four samples were tested using the double-integrating sphere trials with 1 mm and 5 mm cuvettes. An initial trial was run using approximately 1 ml of a  $7.124 \times 10^6$  microsphere/ml 1.8% saline solution to test the functional ability of the integrating sphere setup. This trial implemented  $245 \mu\text{W}$  incident laser power. It was later determined that this power was saturating the collimated detector and  $10 \mu\text{W}$  incident power was used for the remainder of the double-integrating sphere experiments. The second trial using  $10 \mu\text{W}$  incident power incorporated a 5 ml 1.8% saline solution,  $9.0 \times 10^6$  microspheres suspended in a 5 ml 1.8% saline solution, and  $9.0 \times 10^6$  live melanoma cells suspended in a 5 ml 1.8% saline solution.



### 7.4.3 Curve Fitting

Each photodiode measurement in mV was converted to power in the form of nW according to the experimentally derived curve fit polynomials described in Section 7.3.3 and shown in Figure 7.5 using MATLAB 7 (MathWorks, Natick, MA). This was necessary to account for the non-linear behavior of the photodiode detectors and to analyze the data as a power measurement as opposed to voltage.

### 7.4.4 Data Analysis

Both ambient light measurements (signal with no incident laser light in dark room) and maximum light measurements were recorded at each laser wavelength prior to the experiments. The maximum value for the collimated detector was determined by placing the two spheres together with no intervening sample and measuring a directly incident beam. The maximum values for the diffuse transmission and reflection photodiodes were obtained by placing a 99% reflection standard (LabSphere, North Sutton, NH) over the collimated transmission port of the transmission sphere and the collimated transmission port of the reflection sphere, respectively. After converting all voltage measurements to power, the ambient light measurements for all three detectors were subtracted from both the maximum value measurements and the measurements derived from the intervening samples to eliminate ambient light input when measurements were taken.

A normalized ratio for each detector was obtained for every trial and every sample by dividing the sample measurement (minus ambient input) by the maximum measurement for the respective detector (minus ambient input). This calculation is displayed in Equation 7.8

$$\% \text{Light} = (S - A)/(M - A) \quad (7.8)$$

where % Light is the percentage of light collected by each detector, S is the sample measurement for the respective detector, A is the ambient light measurement for the respective detector, and M is the maximum value measured for the respective detector. These ratios are then entered into the Inverse Adding-Doubling Algorithm

	543 nm	594 nm	633 nm
$\mu_a$	0.00882mm <sup>-1</sup>	0.0237mm <sup>-1</sup>	0.0104mm <sup>-1</sup>
$\mu_s$	0.0888mm <sup>-1</sup>	0.067mm <sup>-1</sup>	0.0606mm <sup>-1</sup>
$\mu_s'$	0.0168mm <sup>-1</sup>	0.0101mm <sup>-1</sup>	0.00648mm <sup>-1</sup>
$g$	0.81	0.849	0.893
$\tau$	0.488	0.454	0.355
$a$	0.91	0.739	0.854

Table 7.1: Optical properties of black latex microspheres using a double-integrating sphere method and a 1 mm cuvette.

to determine optical properties for each sample.

## 7.5 Double-Integrating Sphere Results

### 7.5.1 Optical Properties

The optical properties of 6.6  $\mu\text{m}$  Black CML Latex Microspheres where derived at three wavelengths using a 1 mm cuvette. These results are displayed in Table 7.1.

### 7.5.2 Variation of Optical Properties with Wavelength

The optical properties displayed in Table 7.1 were plotted as a function of wavelength as shown in Figure 7.6.

## 7.6 Single-Integrating Sphere Materials and Methods

The single-integrating sphere method was introduced to eliminate the complexity of the double-integrating sphere measurements including the non-linear behavior of the detectors with the hope of improving reliability and deriving more accurate optical properties.

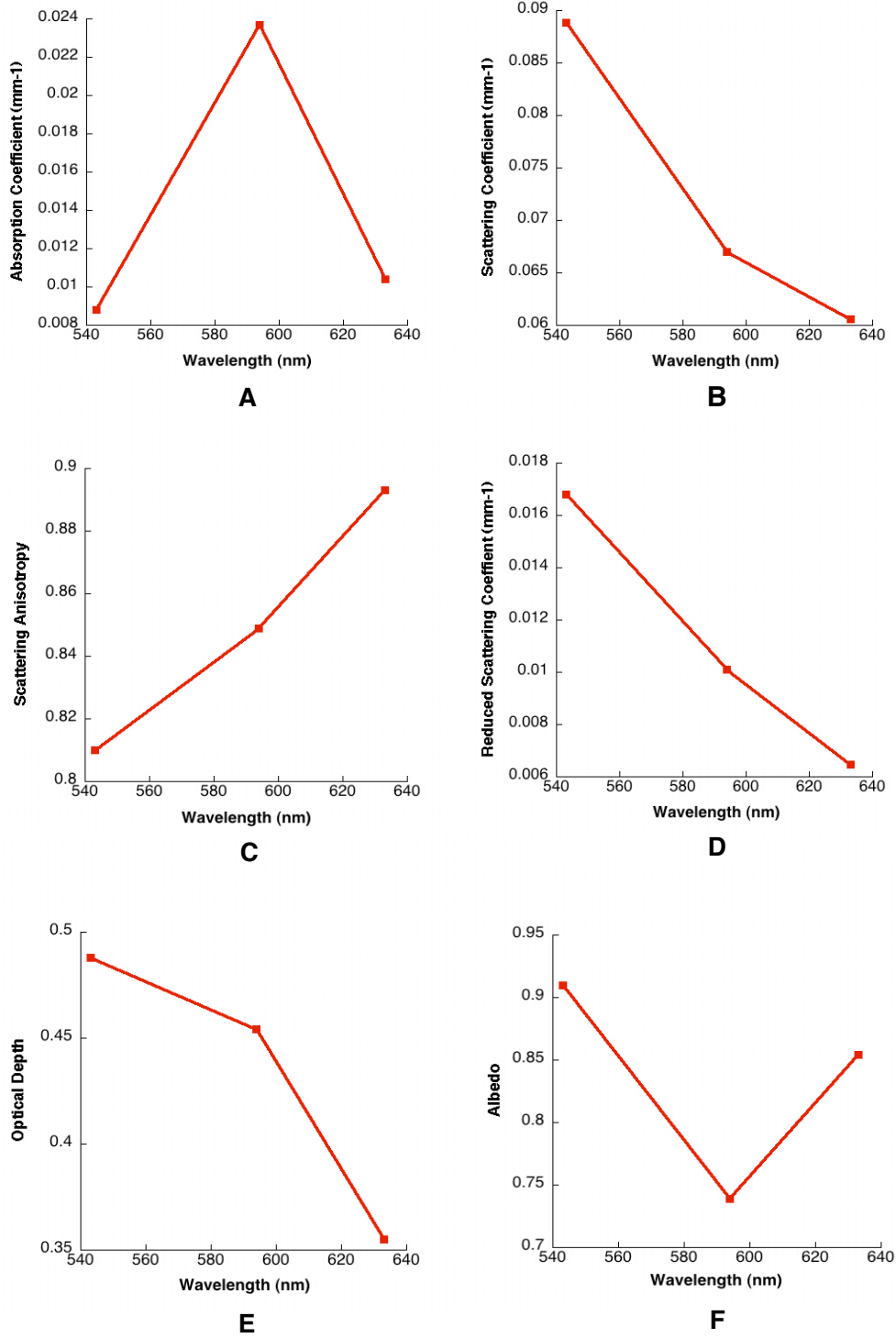


Figure 7.6: Optical properties as a function of wavelength using double-integrating spheres and 1 mm samples. A. Absorption coefficient. B. Scattering coefficient. C. Anisotropy. D. Reduced scattering coefficient. E. Optical depth. F. Scattering albedo.

### 7.6.1 Experimental Design

The single-integrating sphere design uses only one integrating sphere with 5 ml cuvette samples placed at the entrance and exit ports of the integrating sphere for the respective transmission and reflectance measurements. Instead of incident laser light and photodiode detectors, a HL-2000 Halogen Light source and HR-2000 High-Resolution Spectrometer (Ocean Optics Inc., Dunedin, FL) were implemented as the light source and detector. The light source was coupled into a 1000  $\mu\text{m}$  tefzel fiber (Thorlabs, Newton, NJ) and situated approximately 4 mm away from the samples resulting in an 8 mm spot size. The samples tested included  $5.4 \times 10^6$  microspheres suspended in 5 ml of 1.8% saline and  $5.4 \times 10^6$  live melanoma cells suspended in 5 ml of 1.8% saline. Data acquisition was averaged 5 times with a 500 msec integration time for transmission and a 440 msec integration time for the reflection measurement. Data was analyzed using OOIBase32 (Ocean Optics Inc., Dunedin, FL). Light reference for the transmission spectrum was taken using a 1.8% saline sample while light reference for the reflection spectrum was taken using a 99% reflectance standard and no sample. The reflection measurements were taken by inserting the fiber into the integrating sphere and situating it 4 mm from the reflection sample at the exit port of the sphere.

## 7.7 Single-Integrating Sphere Results

The single-integrating sphere trials were run repeatedly during the time that this thesis was being written. Although, the results should have given a much more accurate and reliable representation of the optical properties of both the black latex microspheres and the melanoma cells, no such results were obtained in a manner timely enough to be included in this thesis. Despite multiple efforts, the amount of light measured by the spectrometer for transmission and reflectance was too great resulting in a combined value greater than one which could not be processed by the Inverse Adding-Doubling Algorithm. This is most likely attributed to the unsheathed source fiber emitting excess light captured by the sphere. Further mod-

ification of the system may allow for more useful data. These experiments are included in the thesis to provide information on current developments regarding optical property determination. This method should provide important results that need to be considered to gain a complete understanding of the materials used to test the photoacoustic device.

## 7.8 Discussion

### 7.8.1 Double-Integrating Sphere

The results for the original double-integrating sphere trials using a 1 mm sample path length were partially successful in determining optical properties of black latex microspheres. At this time, these are the only results that have been analyzed due to problems associated with the IAD. The scattering coefficient ( $\mu_s$ ), the reduced scattering coefficient ( $\mu_s'$ ), the anisotropy ( $g$ ), and the optical depth ( $\tau$ ) all produced results that would be expected by optical theory. The absorption coefficient ( $\mu_a$ ) and the scattering albedo ( $a$ ), however, did not produce results as expected.

The scattering coefficient decreases linearly with increasing wavelength. This is expected because of Mie Scattering which occurs when light photons interact with particles that are larger than the wavelength with which they are interacting. In this case, studies of randomized cellular structures have shown that lower wavelengths display higher scattering coefficients. This relationship is shown in Figure 7.6B. The scattering anisotropy increases linearly with wavelength as shown in Figure 7.6C. Anisotropy varies with particle size and wavelength in a way that is largely undefined except through experimental trials with the medium of interest. The reduced scattering coefficient can be thought of as the average scattering probability through a deep sample. It should behave similar to that of the scattering coefficient as shown in Figure 7.6D. Referring to Equation 7.7, the reduced scattering coefficient should decrease with decreasing scattering coefficient and increasing anisotropy. All of these parameters are reflected in Figure 7.6. The optical depth decreases with wavelength as shown in Figure 7.6E. This is expected as optical depth is determined

by the addition of  $\mu_a$  and  $\mu_s$  as shown in Equation 7.6.

The absorption coefficient did not follow expected results. The albedo followed suit as it is dependent upon the absorption coefficient. The absorption coefficient should have increased slightly or remained constant with wavelength according to spectrometer data of latex microspheres displayed in Figure 4.1. Clearly the results of this study did not reflect that pattern. The absorption and scattering coefficients are the two most important optical properties for this project since they govern light absorption and path length, respectively, which ultimately determines the strength of a photoacoustic signal. For this reason it was decided that an alternative method for optical property determination would be required for acquiring a more accurate absorption coefficient. Therefore, 5 mm sample cuvettes were used as opposed to 1 mm. Single-integrating sphere theory was also implemented as an alternative to the double-integrating sphere method.

## 7.9 Conclusion

The optical properties can provide important information as to the makeup of a material. More importantly they govern a material's ability to produce a photoacoustic signal by determining how light interacts with a substance. The scattering coefficient and the absorption coefficient are the two most important properties in regard to this work. The scattering coefficient determines how much a single photon can interact with a substance by giving information regarding the path length of the light. The more light interactions, the higher the probability of absorption. The absorption coefficient of course determines the amount of light that a substance can absorb. This is directly related to the strength of the photoacoustic signal as the light must be absorbed before it can be transformed into thermo-elastic energy. Determining the optical properties of the black microspheres and the melanoma cells would allow one to draw direct correlations between the two absorbers. This would allow for better comparison of the peak photoacoustic signals by, for example, describing which substance is a better absorber. Unfortunately, due to the time constraints of this project and a problem with the IAD algorithm, this was not possible

for inclusion in this manuscript. Further experimentation should be conducted to accurately determine this information based upon the ground work laid out in this chapter.

# Chapter 8

## General Discussion and Conclusions

### 8.1 Photoacoustic Detection System

The photoacoustic system for the detection of metastatic melanoma has been subject to a number of revisions in order to determine the most efficient method of detecting low numbers of cancerous cells *in vitro*. Beginning with a tediously handcrafted dual chamber flow cell and ending with a customized flow cell adapted from a cuvette used for spectroscopy, the detection system has proven to be a constantly evolving entity. Even today, we are still working to improve upon the detection chamber. Entirely new designs are being drafted that further decrease the exposure area of the flow cell, increasing the likelihood of detecting a single cell within the system by decreasing the chances of allowing any material to pass outside the excitation beam path.

There is strong evidence that this system has the ability to detect the presence of melanin in solution. We believe that the device in its current state provides the most efficient method for doing so to date. The system is easy to use and allows for relatively simple sample preparation in that once a cell block is isolated, only saline is required to be added in order to conduct the voltage signal. Samples can be quickly introduced to the system via the external reservoir and circulated using a peristaltic pump to induce negative pressure. The test solutions can also be easily removed and the entire system can be cleaned in minutes providing efficient results



and the capacity for high volume processing.

Although many modifications to the detection chamber may still be made to improve upon the sensitivity of the device, the current method of a circulating flow system appears to be best suited for presenting entire samples to the detection area of the device.

## 8.2 Detection of Tissue Phantoms and Sensitivity Characterization

The majority of the developmental work for this device has been done using phantoms in the form of 6.6  $\mu\text{m}$  Black CML Latex Microspheres, which act as a broadband absorber similar to that of melanin. Microsphere solutions were used to prove the functionality of the detection system as well as characterize the sensitivity and detection threshold of the device.

**Photoacoustic signals derived from black latex microspheres have been discriminated in the amount of 9 microspheres per irradiated beam path.** The current setup has confirmed these results and has shown a detection threshold of 18 microspheres with a peak reflection signal of 1.44 mV and a signal to noise ratio of 3.37. This is a very strong and clearly differentiated signal which could be decreased to 0.5 mV and remain discernible. It would be possible through further experimentation to decrease the threshold of the current setup, as it stands today, to single microsphere detection by decreasing the concentration of the test solution and increasing the gain. The sensitivity of the current setup is estimated to be 2.0 microspheres per irradiated beam path. This is a profoundly sensitive device considering the size of the microspheres and the short life of this project.

We have also provided a method for the isolation and melanoma cells from whole blood. It has been tested and proven that the peripheral blood mononuclear cell layer can be isolated and placed in the detection system without creating any false positives. However, the simple addition of tissue phantoms in the form of latex microspheres to whole blood has produced strong results indicating that the protocol for sample preparation can accurately isolate foreign bodies, such as melanoma, in

the blood stream. Initial results have proven successful in detecting broadband absorbers in the midst of millions of mononuclear cells.

### 8.3 Melanoma Detection

**The photoacoustic device has successfully detected live melanoma cells in a standard saline suspension.** Approximately 200 melanotic melanoma cells per irradiated beam path were necessary to create a 4 mV signal. Assuming that the melanoma cell line cultured for this project is indicative of the cellular nature of other melanin producing cells, it can be proposed that an isolation of 60,000 melanoma cells from whole blood would be necessary to produce a similar signal. This is assuming that only 5% of malignant melanoma cells actively produce melanin and a 15 ml saline suspension is made. However, if a threshold peak of 1 mV is assumed only 50 melanotic melanoma cells per irradiated beam path would be necessary requiring only 15,000 melanoma cells to be isolated from whole blood. Considering that it has been reported that up to 100 million disseminated cells may be present in the circulatory system of a class IV metastatic cancer patient, the 15,000 currently needed for this detection system seems easily attainable. In addition, decreasing the solution size, the area of the detection chamber, and flow tubing would increase the concentration of melanoma cells in solution by requiring less saline. This would be an easy system modification to decrease the amount of melanoma cells needed by up to three fold, assuming 5 ml suspensions.

The photoacoustic waveform for malignant melanoma is markedly different from that of other absorbers including the tissue phantom microspheres. Acoustic diffraction by the melanoma cells results in a uniquely identifiable photoacoustic waveform that can be used to differentiate a melanoma signal from potential false positives such as blood. Further experimentation must be conducted to determine the experimental melanoma detection threshold for the device.

## 8.4 Optical Properties and Integrating Sphere Theory

The methodology for determining the optical properties of both black latex microspheres and melanoma has been well established in this thesis as well as by others. The methods need to be modified to accurately portray the optical properties so that adequate comparisons may be made between the two absorbers. In this way, the photoacoustic excitation peaks can be related. Further experimentation should be conducted to accurately determine this information based upon the ground work laid out in this manuscript.

## 8.5 Future Directions

A fair amount of work must be done before the proposed photoacoustic device can be implemented into a clinical setting. One major question remains regarding the success of the photoacoustic system: will the device and the established protocols have the ability to detect cancer in the blood stream of a human patient?

The first step to answering this question is to run trials where the cultured melanoma cells are placed into samples of healthy blood, spun down, isolated, and introduced to the photoacoustic system for detection. This procedure has been attempted already but failed due to an error in blood separation. Following the success of that experiment, randomized trials should be run testing the blood of class IV metastatic melanoma patients. The success of these two trials could lead to the device being implemented as a clinical screening method for metastatic disease. Clinical trials should also be run using the blood of early stage cancer patients to determine the device's ability to screen for the presence of early disseminated cells.

Further experiments should be run to properly characterize the sensitivity of the device to melanoma in saline suspension as shown in this thesis with the latex microspheres. Further improvements must be made to the detection chamber to decrease irradiation area and further improve signal strength. A few methods for doing so include the development of a micro flow cell that transports only a few

melanoma cells and guarantees excitation of all material passing through the flow cell. In doing so the PVDF detector will be decreased in size which may increase signal strength by decreasing the surface area of the detector and eliminate some signal dampening. Chemicals such as Indium Tin Oxide may be applied to the positive surface of the PVDF to increase conductance at the surface of the film. Also, conducting substances other than saline, or an increase in saline concentration, should be investigated to increase signal strength.

Nanotechnology could be used to detect metastatic cells that do not produce melanin. Quantum dots or gold nanoparticles should be investigated for the ability to attach to disseminated cells *in vitro* by recognizing and binding molecular receptors present on the surface of the cells. Should this be possible, the gold nanoparticles would serve as the photoacoustic source as opposed to the cells. Preliminary work has shown that the nanoparticles produce a characteristic photoacoustic signal that could be used to identify the presence of many different types of cancers assuming that their molecular markers could be elucidated. This technology could potentially expand the bounds of this system to detect all types of cancers, including those that do not produce melanin.

## 8.6 Conclusion

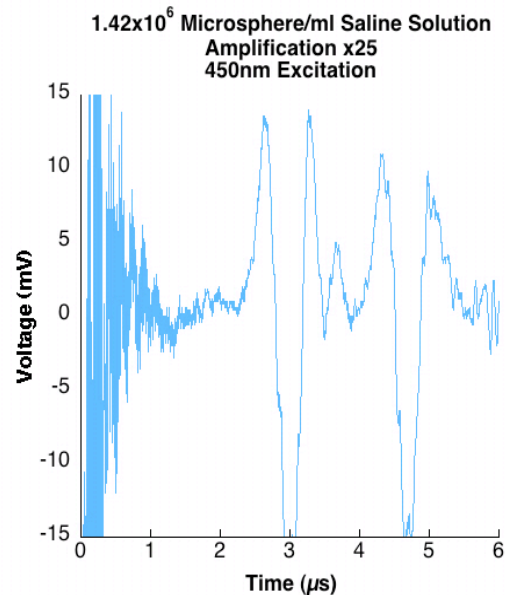
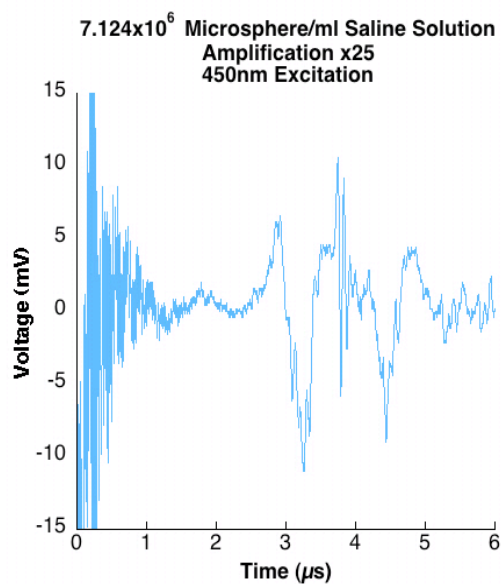
The photoacoustic detection system for metastatic melanoma has proven to be successful. If the detection of melanoma cells isolated from the blood of a metastatic patient proves to be as efficient as the detection of the tissue phantom solutions described in this thesis, the detection system will function as the most efficient form of metastatic cancer detection currently known. With the ability to analyze blood samples within 30 minutes without the aid of a trained histologist, the photoacoustic detection system may prove to be the most reliable method of detecting cancer. This unprecedented method could revolutionize the field of oncology by providing a technique for the early detection of metastatic disease as well as functioning as a method for determining the effectiveness of chemotherapeutics. In addition, if the parallel theory of metastasis holds true, this device would serve as an early detector

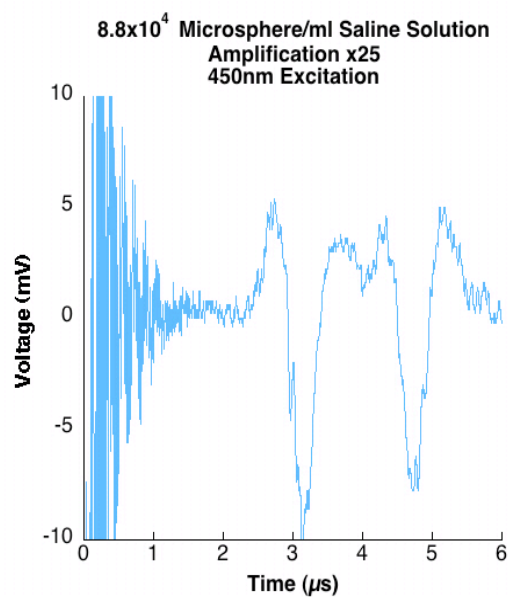
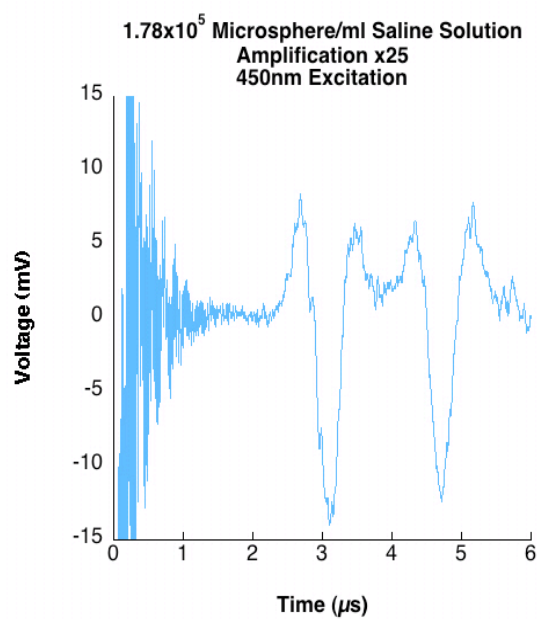
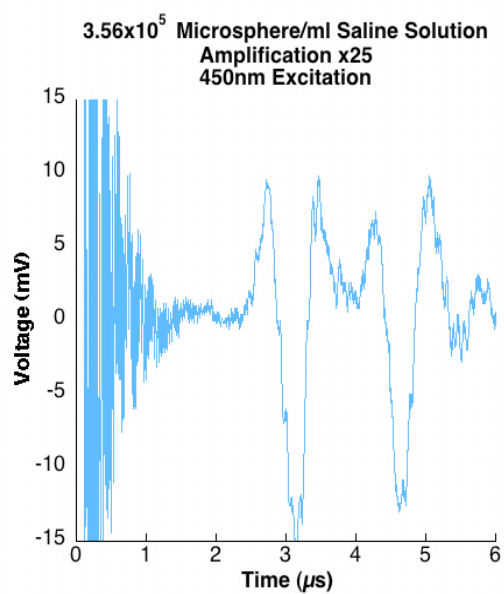
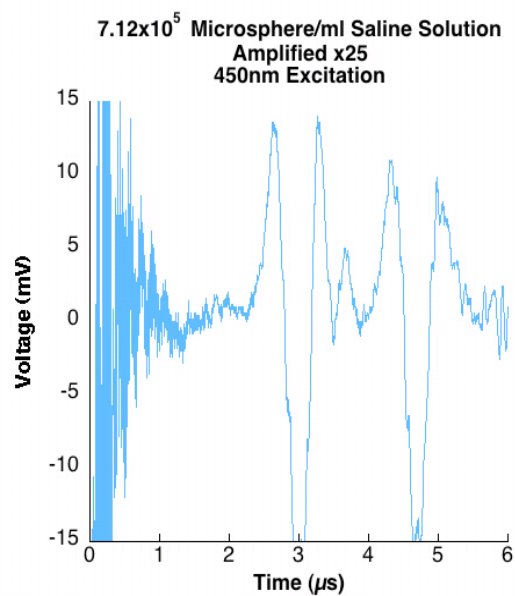
of not only metastatic disease but any melanotic form of cancer near its inception.

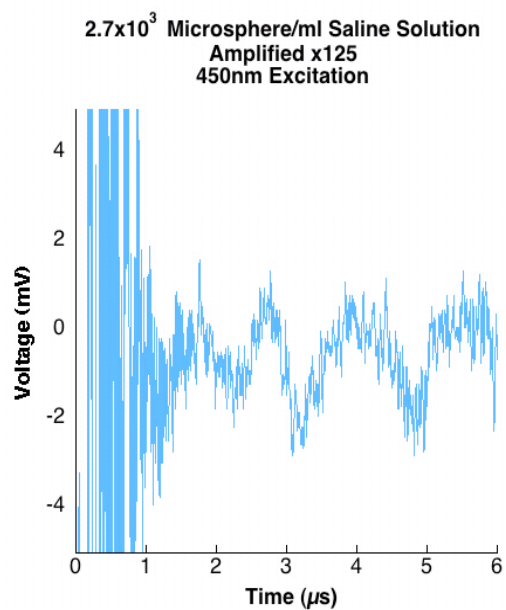
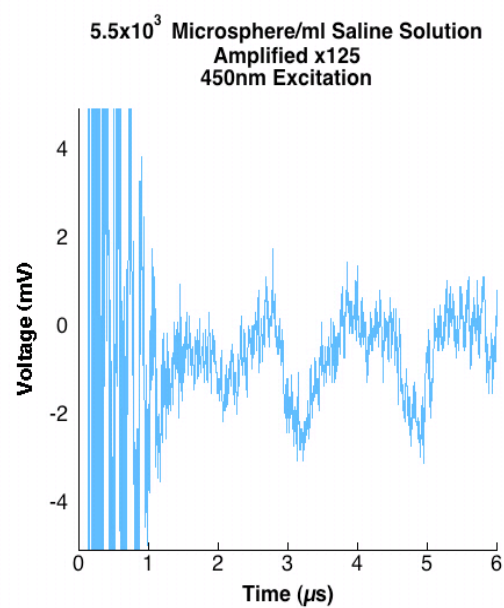
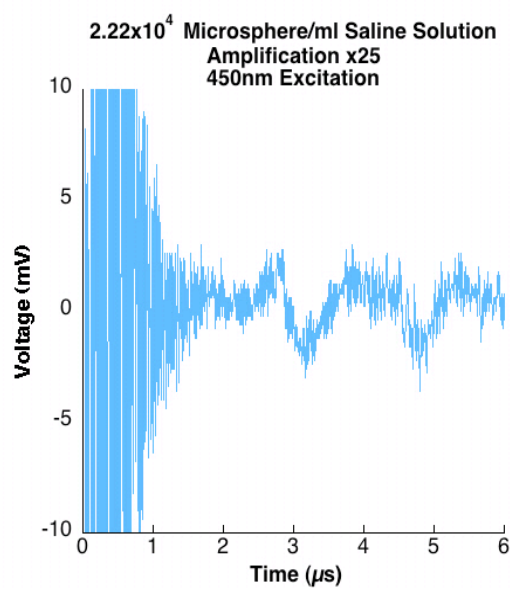
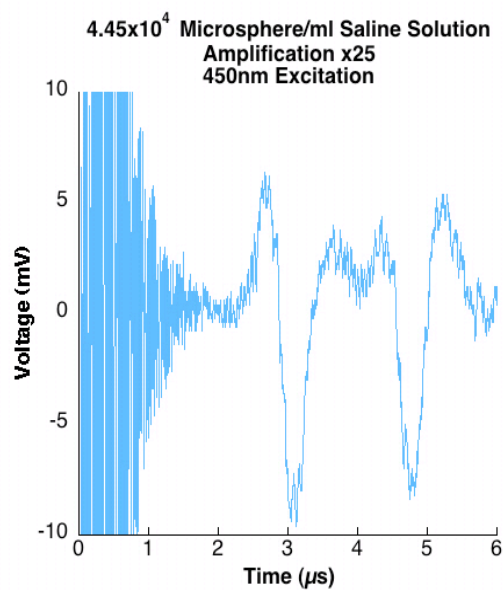
The benefits of this device are clearly evident. It is my hope that some day this technology will be able to be used for the benefit of millions of people affected by cancer throughout the world. Although the early detection of cancer is only half the battle, success in this area brings us that much closer to winning the war.

## Appendix A

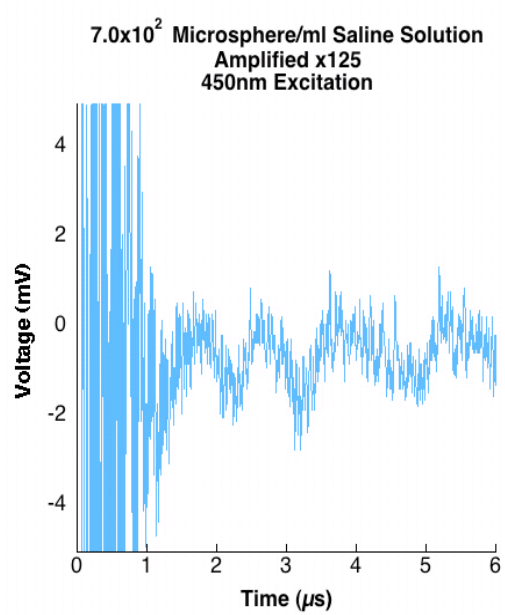
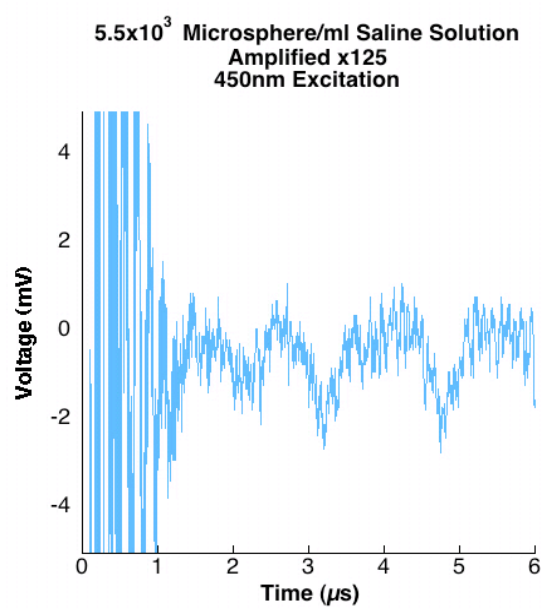
# Photoacoustic Waveforms For Decreasing Concentrations Of Microspheres Using Single Flow Chamber Design





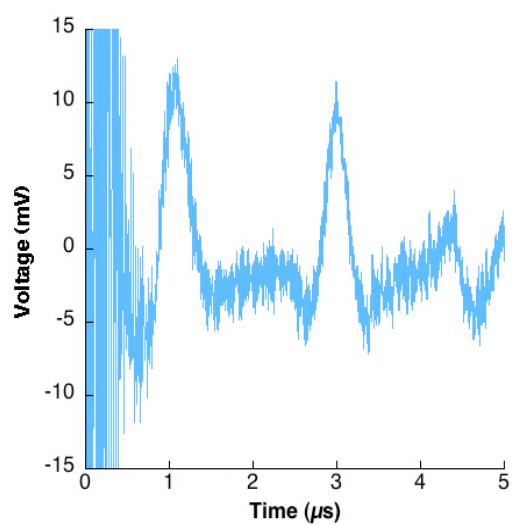
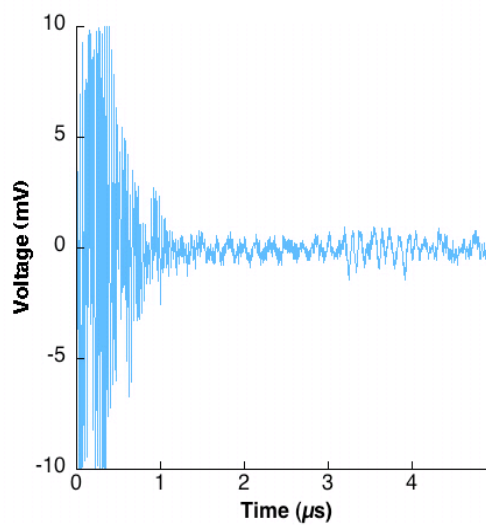




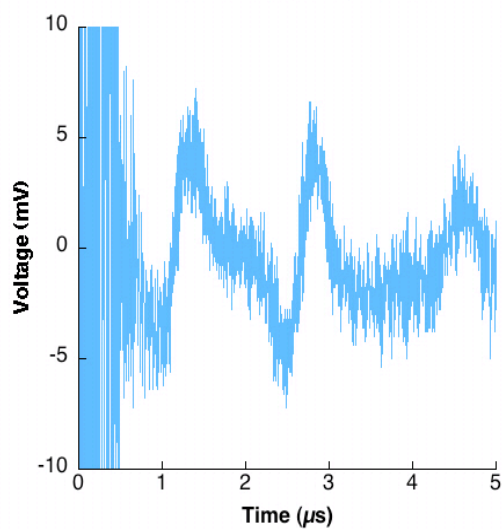


## Appendix B

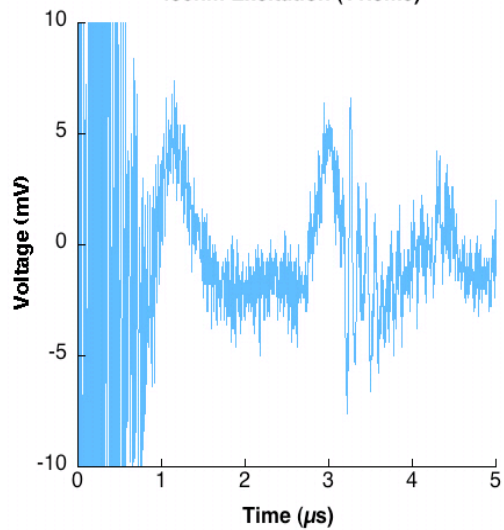
### Photoacoustic Waveforms For Decreasing Concentrations of Microspheres Using Customized Flow Cell Design

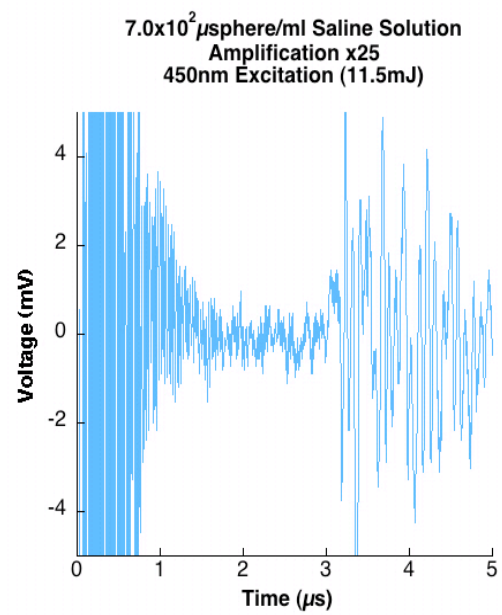
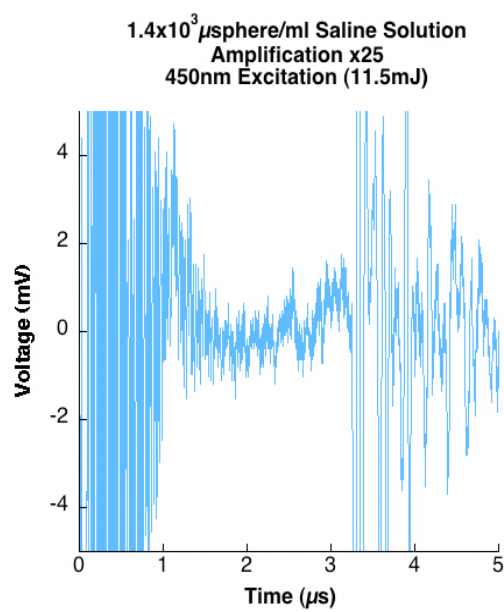
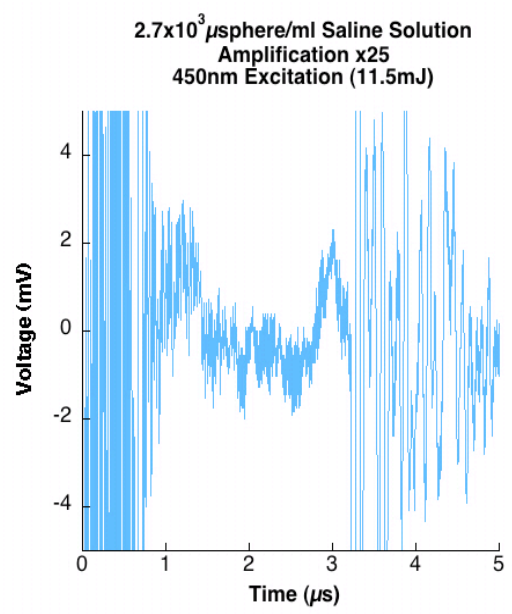
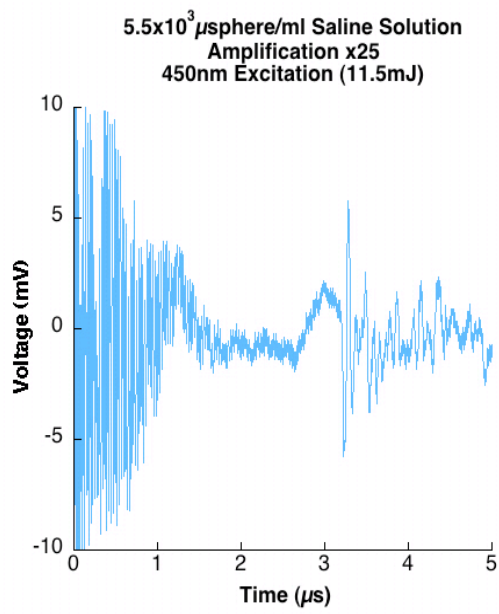


**$4.45 \times 10^4 \mu\text{sphere/ml}$  Saline Solution  
Amplification x25  
450nm Excitation (11.5mJ)**



**$2.22 \times 10^4 \mu\text{sphere/ml}$  Saline Solution  
Amplification x25  
450nm Excitation (11.5mJ)**





# Bibliography

- [1] Author U. Production of sound by radiant energy. Manufacturer and Builder 1881; 156–158.
- [2] Viator J, Komadina J, Svaasand L, Aguilar G, Choi B, Nelson J. A comparative study of photoacoustic and reflectance methods for determination of epidermal melanin content. J Invest Derm June 2004; 1432–1439.
- [3] Paltauf G, Schmidt-Kloiber H, Guss H. Light distribution measurements in absorbing materials by optical detection of laser-induced stress waves. Appl Phys Lett 1996; 69:1526–1528.
- [4] Viator J, Au G, Paltauf G, Jacques S, Prahl S, Ren H, Chen Z, Nelson J. Clinical testing of a photoacoustic probe for port wine stain depth determination. Laser Surg Med 2002; 141–148.
- [5] Siphanto R, Kolkman R, Huisjes A, Pilatou M, de Mul F, Steenbergen W, van Adrichem L. Imaging of small vessels using photoacoustics: An in vivo study. Laser Surg Med August 2004; 354–362.
- [6] Oraevsky A, Wang L. Photons Plus Ultrasound: Imaging and Sensing 2006. The Seventh Conference on Biomedical Thermoacoustics, Optoacoustics, and Acousto-Optics. Washington, SPIE–The International Society for Optical Engineering 2006.
- [7] Morton D, Wong J, Kirkwood J, Parker R. Cancer Medicine, Third Edition, Volume 2. New York, Lea & Febiger, 1993.

- [8] Surh Y. Cancer chemoprevention with dietary phytochemicals. *Nature Reviews Cancer* 2003; 768–779.
- [9] Sporn M, Liby K. Cancer chemoprevention: Scientific promise, clinical uncertainty. *Nature Clinical Practice Oncology* 2005; 518–524.
- [10] Castells A, Rustgi A. Principles of Oncogenesis. [www.intl.elsevierhealth.com/e-books/pdf/478.pdf](http://www.intl.elsevierhealth.com/e-books/pdf/478.pdf).
- [11] Gray J. Evidence emerges from early metastasis and parallel evolution of primary and metastatic tumors. *Cancer Cell* 2003; 4–6.
- [12] Schmidt-Kittler O, Ragg T, Daskalakis A, Granzow M, Ahr A, Blankenstein T, Kaufmann M, Diebold J, Arnholdt H, Muller P, Bischoff J, Harich D, Schlimok G, Riethmuller G, Eils R, Klein C. From latent disseminated cells to overt metastasis: Genetic analysis of systemic breast cancer progression. *PNAS* 2003; 7737–7742.
- [13] Steeg P. Emissaries set up new sites. *Nature* 2005; 750–751.
- [14] Kaplan R, Riba R, Zacharoulis S, Bramley A, Vincent L, Costa C, MacDonald D, Jin D, Shido K, Kerns S, Zhu Z, Hicklin D, Wu Y, Port J, Altorki N, Port E, Ruggero D, Shmelkov S, Jensen K, Rafii S, Lyden D. Vegfr1-positive haematopoietic bone marrow progenitors initiate the pre-metastatic niche. *Nature* 2005; 820–828.
- [15] Gilbey A, Burnett D, Coleman R, Holen I. The detection of circulating breast cancer cells in blood. *J Clin Pathol* 2004; 903–911.
- [16] Chambers A. The metastatic process: Basic research and clinical implications. *Oncology Research* April 1999; 161–168.
- [17] Molnar B, Sipos F, Galamb O, Tulassay Z. Molecular detection of circulating cancer cells. *Digest Dis* 2003; 320–325.

- [18] Krivacic R, etal. A rare-cell detector for cancer. *P Natl Acad Sci* 2004; 10501–10504.
- [19] Gusterson B, Ott R. Occult axillary lymph node micrometastases in breast cancer. *Lancet* 1990; 434–435.
- [20] Cote R, Peterson H, Chaiwun B, etal. Role of immunohistochemical detection of lymph-node metastases in management of breast cancer. international breast cancer study group. *Lancet* 1999; 896–900.
- [21] Fisher B, Redmond C, Fisher E, etal. Ten year results of a randomized clinical trial comparing radical mastectomy and total mastectomy with and without radiation. *N Engl J Med* 1985; 674–681.
- [22] Ring A, Zabaglo L, Ormerod M, Smith I, Dowsett M. Detection of circulating epithelial cells in the blood of patients with breast cancer: comparison of three techniques. *Brit J Cancer* 2005; 906–912.
- [23] Zabaglo L, Ormerod M, Parton M, Ring A, Smith I, Dowsett M. Cell filtration-laser scanning cytometry for the characterization of circulating breast cancer cells. *Cytom Part A* 2003; 102–108.
- [24] Braun S, Naume B. Circulating and disseminated tumor cells. *J Clin Oncol* 2005; 1623–1626.
- [25] Harris S. Tunable optical parametric oscillators. *Proc IEEE* 1969; 2096.
- [26] Grichnik J, Burch J, Schulteis R, Shan S, Liu J, Darrow T, Vervaert C, Seigler H. Melanoma, a tumor based on a mutant stem cell? *J Inv Derm* 2006; 142–153.
- [27] Houghton Mifflin’s The American Heritage Stedman’s Medical Dictionary SE. Blood. <http://columbia.thefreedictionary.com/blood>, 2005.
- [28] Wikipedia. Melanoma. <http://en.wikipedia.org/wiki/Melanoma>, 2006.

- [29] Nicolaus A. Studies of Melanin and Melanotic Compounds: The Chemical Structure of Melanin. <http://www.tightrope.it/nicolaus/link%2024.htm>, 2006.
- [30] Tran M, Powell B, Meredith P. Chemical and structural disorder in eumelanins: A possible explanation for broadband absorbance. *Biophys J* 2006; 743–752.
- [31] Jacques S. Oregon Medical Laser Center: Optical Absorption of Melanin. <http://omlc.ogi.edu/spectra/melanin/index.html>, 2006.
- [32] Kollias N, Baqer A. Absorption mechanisms of human melanin in the visible, 400–720. *J Invest Derm* 1987; 384–388.
- [33] Green F. The Sigma-Aldrich Handbook of Stains, Dyes and Indicators. Wisconsin, Aldrich Chemical Company, Inc. 1974.
- [34] Baylor S, Hollingworth S. Absorbance signals from resting frog skeletal fibers injected with the ph indicator dye, phenol red. *J Gen Physiol* 1990; 449–471.
- [35] Cheong WF, Prahl SA, Welch AJ. A review of the optical properties of biological tissues. *IEEE J Quantum Electron* 1990; 26:2166–2185.
- [36] Pickering J, S.A. Prahl NvW, Beek J, Sterenborg H, van Gemert M. Double-integrating-sphere system for measuring the optical properties of tissue. *Applied Optics* February 1993; 399–410.
- [37] Pickering JW, Moes CJM, Sterenborg HJCM, Prahl SA, van Gemert MJC. Two integrating sphere with an intervening scattering sample. *J Opt Soc Am A* 1992; 9:621–631.
- [38] Prahl SA. Optical property measurements using the inverse adding-doubling program. Unpublished 1999; 1–53.
- [39] Prahl SA, van Gemert MJC, Welch AJ. Determining the optical properties of turbid media by using the adding-doubling method. *Appl Opt* 1993; 32:559–568.



## **VITA**

Ryan Michael Weight was born on January 9, 1983, in Vinita, Oklahoma. He was raised in St. Joseph, Missouri and graduated in July of 2005 with a Bachelor of Science in Biological Engineering from the University of Missouri-Columbia. He entered into the graduate program for Biological Engineering at the University of Missouri-Columbia in August of 2005 and received his Masters of Science in August of 2006.